Design and Analysis of Membrane Structures in FEM-Based Software

Master-Thesis

A thesis submitted in partial fulfillment
of the requirements for the degree of

Master Membrane Structures

submitted to

Anhalt University of Applied Sciences

Faculty of Architecture,
Facility Management and Geo Information

by

Ing. Rostislav Lang
8.11.1987, Brno, Czech Republic

Matrikel Number
4061571

Submission Date: September 2017

First Tutor: Prof. Dr.-Ing. Robert Off

Second Tutor: Prof. Dr.-Ing. Kai-Uwe Bletzinger

Statement

I hereby declare that the work presented in this Master thesis, entitled

Design and Analysis of Membrane Structures in FEM-Based Software,

is entirely my own and that I did not use any sources or auxiliary means other than those referenced.

Dessau, September 2017 ....
Rostislav Lang

CONTENT

1 INTRODUCTION

Membrane structures are one of the current trends in civil engineering and architecture. They are fascinating in both aspects, their appearance and physical behaviour. When considering the first aspect, we can describe them as lightweight structures of beautifully curved shapes. As broadly known, those shapes cannot be chosen freely since they must be physically suitable because the material used for tensile structures can withstand no bending or compression, and thus shapes under tension have to be used. This is the first task to solve when designing membrane structures, involving both the architectural requirements and physical principles. In that way, membrane structures take shapes that have to be in accordance with nature. This task to find a beautiful and physically suitable shape is known as *form-finding*.

After the form-finding is performed, it is necessary to check the load-bearing capacity and other code-specific or investor's requirements in *structural analysis*. The structural response of such structures is strongly nonlinear in terms of both the impact of geometry changes and material behaviour.

If all the requirements are fulfilled, the structure can be fabricated. To make this step possible, it is necessary to generate *cutting patterns* as membrane structures exhibit double curvature and therefore, they have to be approximated by a certain amount of planar patterns.

The presented work will focus on all those steps. A theoretical introduction will be presented in the first part of each chapter, then practical examples will be shown to demonstrate the mentioned statements. The presented examples were created using the RFEM software, including the new add-on modules RF-FORM-FINDING and RF-CUTTING-PATTERN for the design and analysis of membrane structures, that were developed recently by the cooperating companies *Dlubal Software s.r.o.* [I] and *FEM Consulting s.r.o.* [II].

2 FORM-FINDING

The form-finding process is an essential part of tensile structures designing. This indispensable shape analysis has been the subject of many research works and as a result, many methods have been proposed. The physical principle of the form-finding process will be described in the first part of this chapter *Form-Finding*. The second part will be focused on the practical examples, which complete and illustrate the described topics.

2.1 Theory

The methods that have been proposed and implemented into software as tools for the form-finding process can be divided into many categories, such as *Force Density Method* (*FDM*), *Dynamic Relaxation* (*DR*), *Updated Reference Strategy* (*URS*), *Natural Force Density Method* (*NFDM*), etc. [1-18]. When calculating the shape of a membrane structure, there is a great difference between the classic FDM and the other methods listed above, since the *FDM* replaces the membrane by a cable mesh, while the other methods use surface finite elements for the membrane. In addition to this great difference, there are some smaller differences between the methods using *2D FE*. The difference is that the form-finding process can be assumed as a static or dynamic task or even as a specially formulated form-finding task, for example. Regardless the particular method, the goal is always to find the equilibrium shape for the surface prestress field that is an input. The particular method is more or less the way how to reach this target. The further important difference can be seen in the generality of the methods or the way of implementation since the interaction of the membranes and cables subjected to the shape finding with the substructure is highly desirable and can influence the whole design. This general concept will be described later.

2.1.1 Physical Essence of Form-Finding

The general form-finding task is to find the equilibrium shape for the given prestress field in the membrane/cable while considering the boundary conditions and external loads, if they are required. No dependence on material exists here. In contrary to structural analysis, the stresses are not the result, but the input and deformations are driven by that way. This causes singularities as described later, which has to be overcome.

The shape resulting from the form-finding process is the prestressed reference configuration for further nonlinear analysis. However, the patterns are practically the absolute reference (initial) configuration because they are the unstrained (reference/initial) shapes forming the real construction (*Fig. 1*).
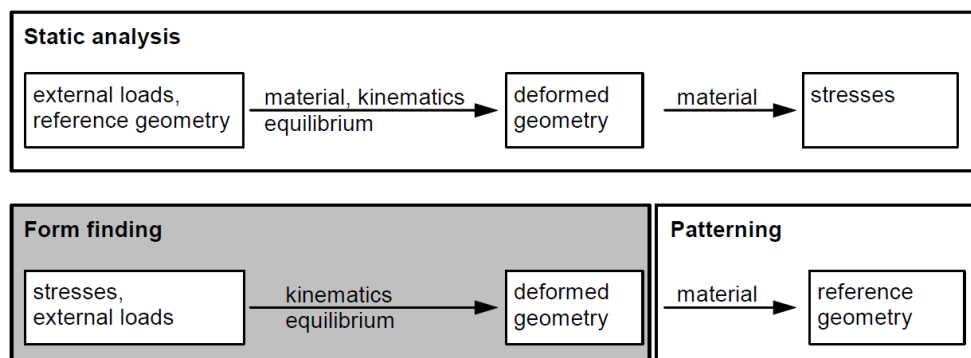

Fig. 1 – Comparison of static analysis and form-finding [19]

2.1.2 General Finite Element Approach

Regardless the differences described above, the equilibrium state of the structure subjected to the form-finding process can be written in the same manner as the equilibrium state of the body in FE analysis. Searching for the shape can be formulated as searching for the minimum of the potential energy $\boldsymbol{\Pi} = \boldsymbol{\Pi}^{int} + \boldsymbol{\Pi}^{ext}$ of internal and external forces in the body $\boldsymbol{\Omega}$. The shape is in equilibrium if the derivative of the potential energy corresponding with the deformation is zero $\partial \Pi / \partial d = 0$. The principle of the FE analysis will be described later (*3.1.1 Principles of FEM Analysis*).

$$\frac{\partial \Pi}{\partial d} = \frac{\partial \Pi^{int}}{\partial d} + \frac{\partial \Pi^{ext}}{\partial d} = \int_{\Omega_0} S : \delta E \, d\Omega_0 - \int_{\Omega_0} q \cdot \delta d \, d\Omega_0 = \int_{\Omega} \sigma : \delta e \, d\Omega - \int_{\Omega} q \cdot \delta d \, d\Omega = 0 \quad (1)$$

Where d are deformations, $\boldsymbol{S}$ and $\boldsymbol{\sigma}$ are *2nd Piola-Kirchhoff stress tensor* and *Cauchy stress tensor*, $\boldsymbol{E}$ and $\boldsymbol{\varepsilon}$ are *Green-Lagrange strain tensor* and *Euler-Almansi strain tensors*, Ω_0 is the *reference configuration*, and Ω is the *actual configuration*. As stated in the following chapter (*3.1.1 Principles of FEM Analysis*), the equilibrium of the body can be described in both the reference and the actual configurations.

However, it is not possible to directly solve the new shape due to its unknown position. Even though the normal direction of the membrane/cable is clear, the tangential redistribution of nodes is unclear as the infinite number of different positions can satisfy the same 3D shape (*Fig. 2*).
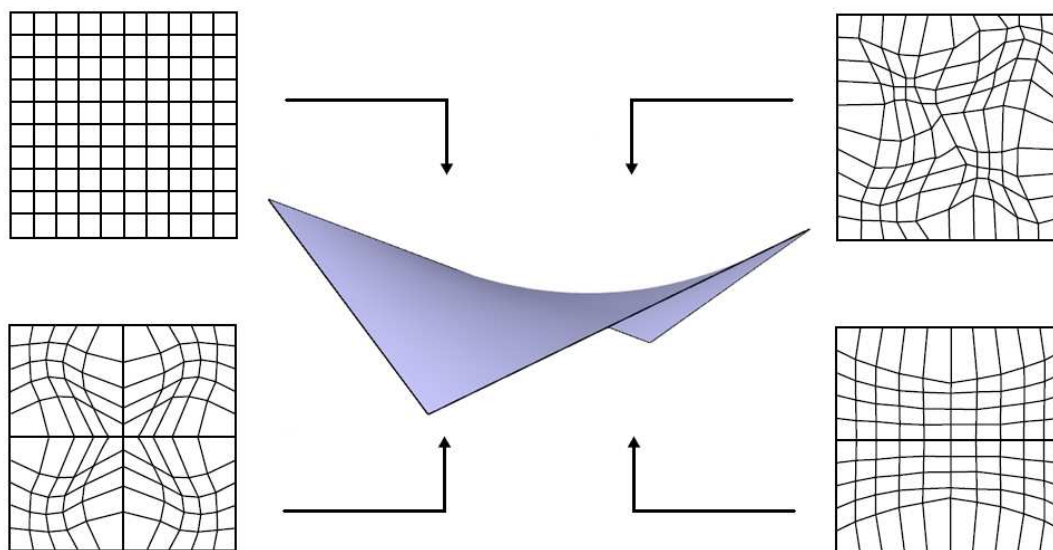

Fig. 2 – Arbitrarily deformed meshes for the same surface geometry ([6] with modification)

A way how to overcome this ambiguity is to define the problem with respect to the known (initial) position of the body. By solving the system of equations, we obtain the new geometry. This new geometry is closer to the equilibrium shape than the previous one and we use it for the next step (*Fig. 3*). Continuing in this process will lead to the shape improvement, which is closer to the required equilibrium position with each further iteration. This philosophy is related to the nonlinear analysis, where we assess the balance of the new shape after each calculated iteration. From a physical point of view, it thus does not make a difference whether we choose to use the *nonlinear analysis*, the *updated reference strategy* or the *dynamic relaxation* as a specific method for solving the task.
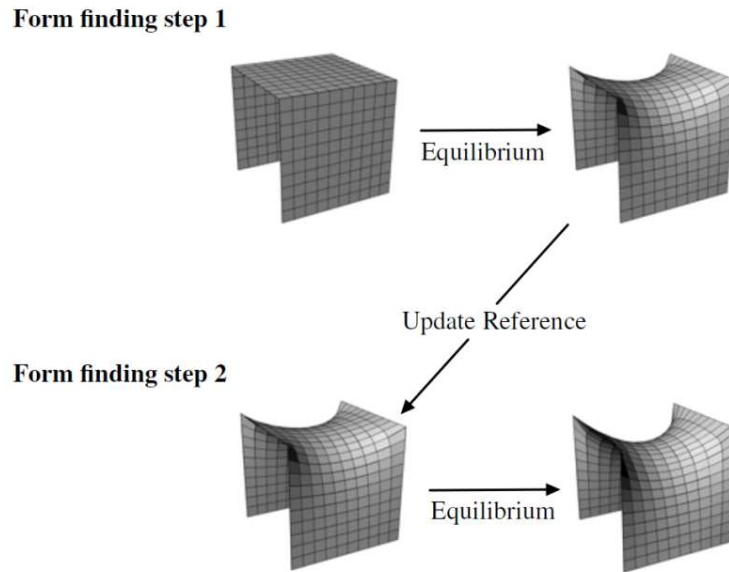
Form finding step 1

Equilibrium

Update Reference

Form finding step 2

Equilibrium

Fig. 3 – Iterations of the form-finding process ([20] with modifications)

This general finite element approach of the form-finding process allows us to combine searching the unknown equilibrium shapes with the nonlinear analysis of the supporting structure loaded by the prestress in membranes or cables. Even though the membranes and cables were only mentioned as the subjects of form-finding, the shapes can also be searched for shells and beams, as discussed later.

2.1.3 Force-Finding as Part of Form-Finding

In the previous text, the only task was solving the equilibrium shape for already defined spatial prestress in equilibrium. However, the only equilibrium prestress which can be defined in advance is actually the isotropic prestress. Constant orthotropic prestress is only in equilibrium if the Gaussian curvature is equal to zero $K = 0$, which is not the case of the double-curved shapes of tensile structures.

$$K = k_1 \cdot k_2 = \frac{1}{r_1 \cdot r_2} \tag{2}$$

Where k_1, k_2 are the principal curvatures, and r_1, r_2 are radii in this directions at the given point of the surface.

As a consequence of this fact, the membrane structures require general orthotropic prestress if the isotropic one is not applicable for some reason. However, it is virtually not possible to define the general orthotropic prestress in equilibrium. Therefore, the task of the form-finding process is not only to find the shape for the given prestress but also to find the prestress in equilibrium itself that approximates the required values in the warp and weft directions, which are defined by an engineer or an architect. There is no need to mention that the closest possible approximation of the defined values is required since the smooth prestress in the membrane without concentrations, if they are not necessary, is the most desirable.

2.1.4 Unstable Equilibrium Position of Elements Under Compression

There is one interesting phenomenon when comparing the shape calculation of a structure or structural parts under tension and under compression. While the structure under tension takes the stable equilibrium position, the structure under compression takes the unstable equilibrium position (*Fig. 4*).
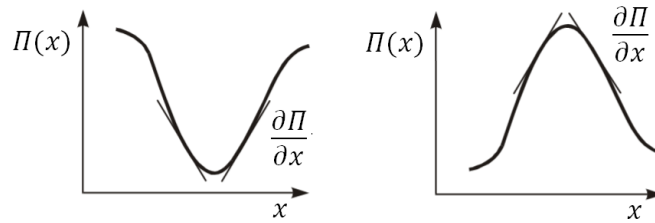
Fig. 4 – Stable and unstable equilibrium position

As a result of that fact, the tensioned structures converge to the equilibrium position if the required prestress is physically realizable. The compressed structures suffer instabilities, which has to be overcome during the calculation. The well-known way of solving this difficulty is to inverse the compression into the tension and to invert the load acting on the structure. This way, used on physical models already in the ancient time, may solve the calculation stability for structures subjected exclusively to the compression. However, when the form-finding deals with a combined structure where both the parts under the tension and the compression are used, this method is not sufficient. Such an inversion would solve the required parts under the compression which would be inverted into the tension; however, the parts under the tension would be inverted into the compression and the same problem with calculation divergence remains. Therefore, a local stabilisation of the parts under the compression has to be designed and implemented in order to solve the phenomenon described above. The example of such a structure will be presented later.

2.2 Practice

The practical part of the *Form-Finding* chapter will be focused on the presentation of several examples of both tensioned and inflated structures. The full integration of a supporting structure as well as examples focused on the previously described phenomena will be shown.

2.2.1 Form-Finding of Mechanically Prestressed Membrane

Two basic shapes will be presented here: a hypar and a cone-shaped structure (*Fig. 5, Fig. 14*). The hypar membrane will be presented for two different prestress tasks. The first one is the isotripic prestress, where $n_x = n_y = 1.00 \, kN/m$. The force in boundary cables is defined as $N = 10.00 \, kN$. As mentioned before, this prestress can be reached exactly as presented bellow (*Fig. 7 - Fig. 9*).
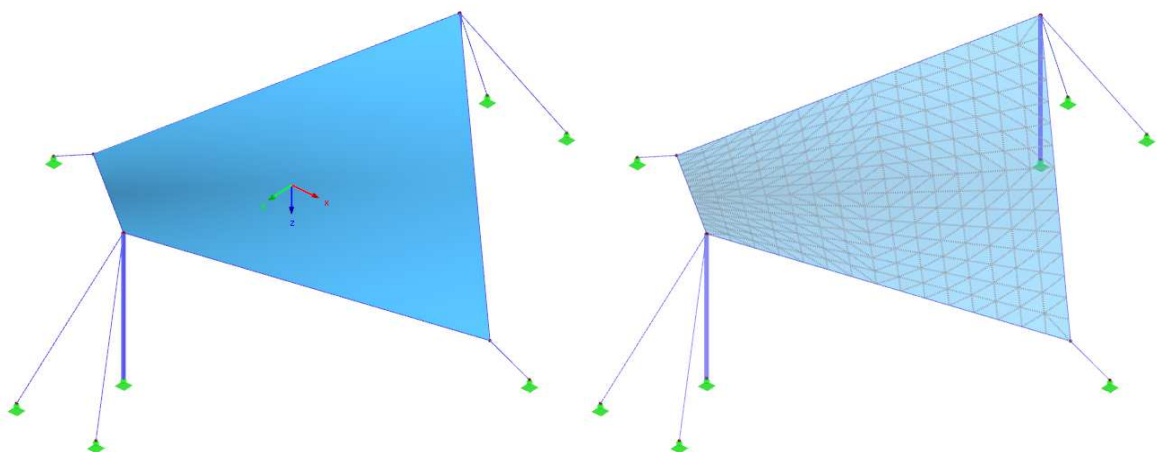

Fig. 5 – Initial shape of a hypar membrane structure with the x/y (warp/weft) orientation displaying (left), FE mesh (right)
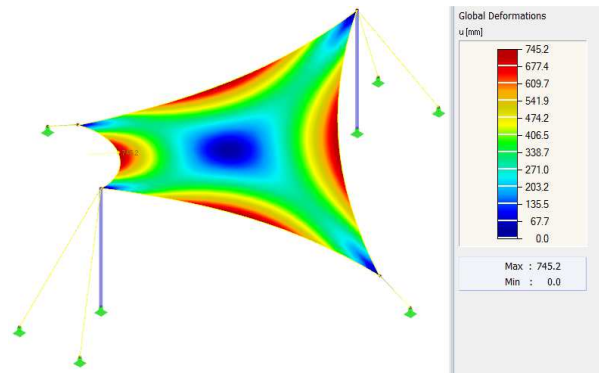
Fig. 6 – Global deformations u in the form-finding

Fig. 7 – Basic internal forces n_x, n_y, n_{xy} and the principal internal forces n_1, n_2
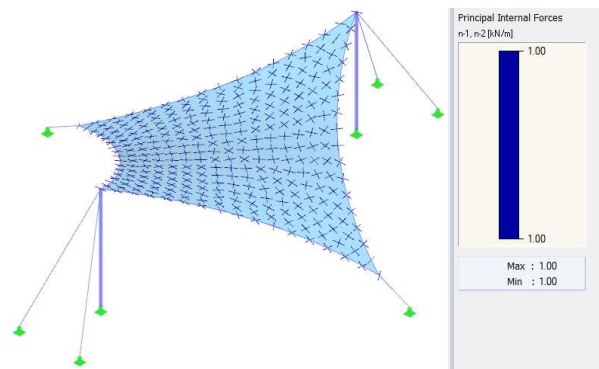

Fig. 8 – Vectors of the principal internal forces n_1, n_2

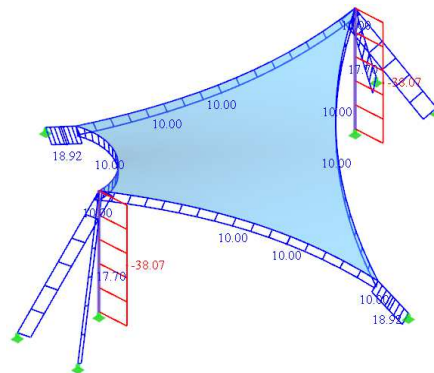*Fig. 9 – Normal forces N in the cables and beams*

The second task is the orthotropic prestress, where $n_x = 2.00 \ kN/m$, and $n_y = 1.00 \ kN/m$. The force in boundary cables is defined as $N = 15.00 \ kN$. Such a requirement cannot be fulfilled exactly as it is not possible because of the physical reasons as mentioned

previously. A prestress field that aproximates those values as close as possible should be calculated (*Fig. 11 - Fig. 13*).
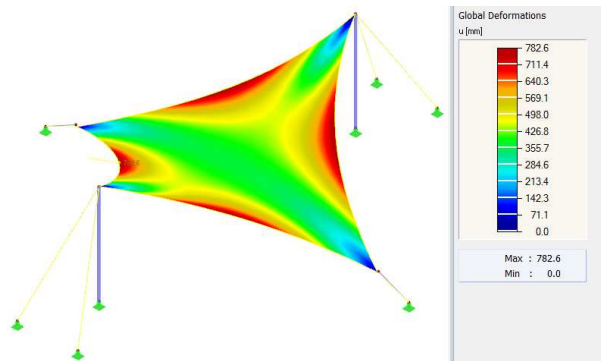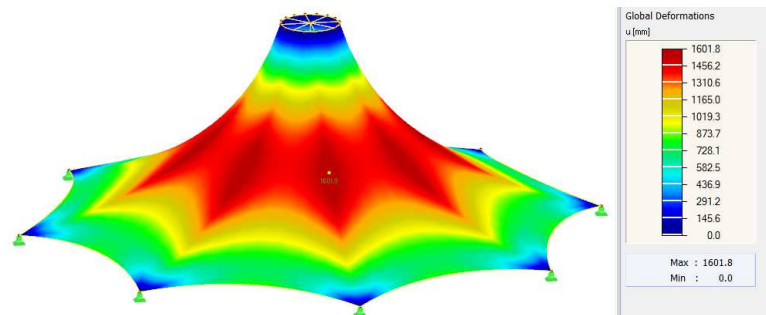

Fig. 10 – Global deformations u in the form-finding
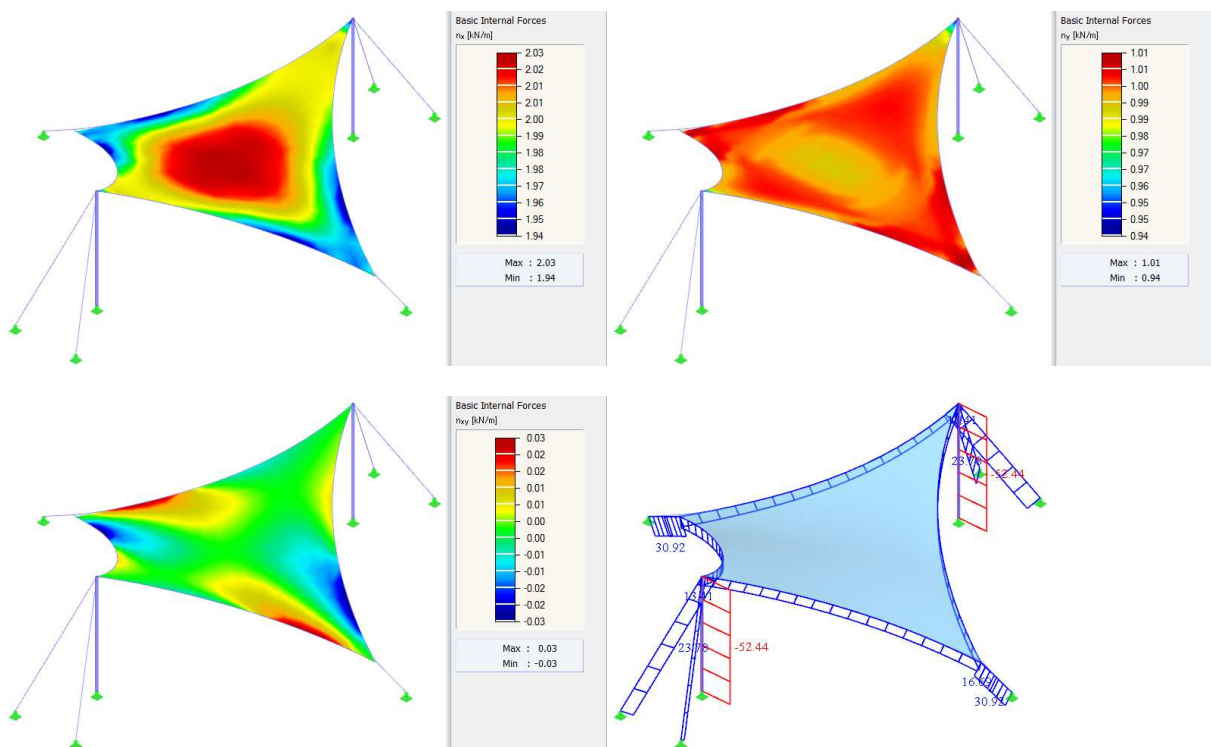
Fig. 11 – Basic internal forces n_x, n_y, n_{xy} in the membrane normal force N in the cables and beams
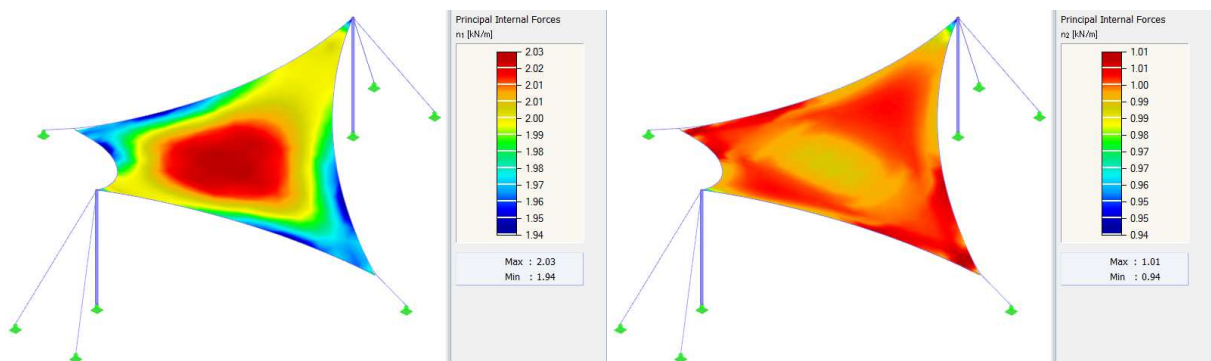
Fig. 12 – Principal internal forces n_1, n_2
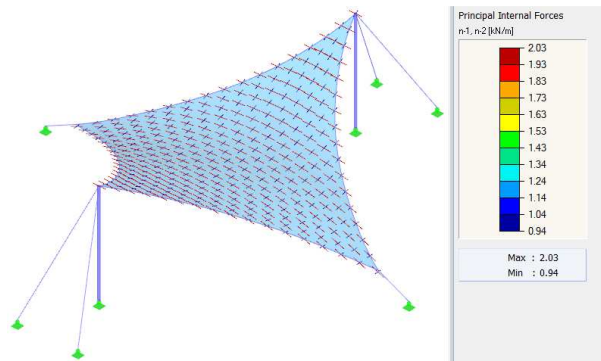
Fig. 13 – Vectors of the principal internal forces n_1, n_2

As already mentioned, concentrations should be avoided, if possible (*Fig. 7, Fig. 8, Fig. 11 - Fig. 13*). However, there are shapes that cannot avoid the high forces in some regions. This is the case of the high/low points of conical structures (*Fig. 16 - Fig. 18*). The concentrations near the top ring are necessary because of physical reasons.
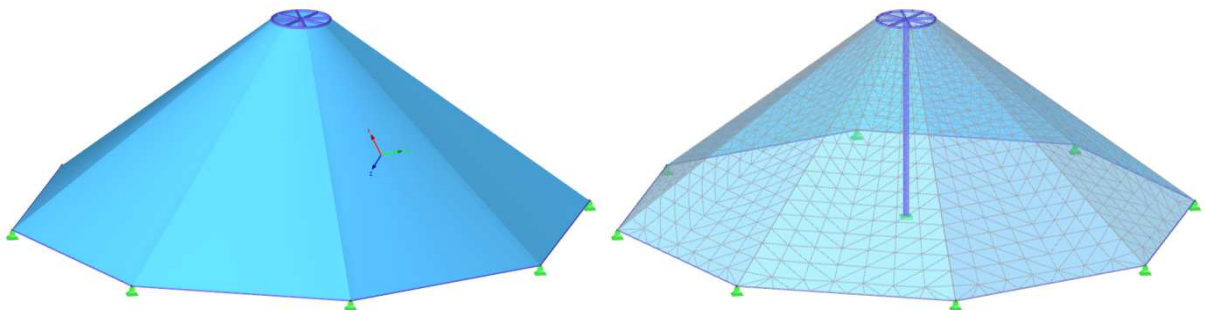
Fig. 14 – Initial shape of a conical membrane structure with the x/y (warp/weft) orientation displaying (left), FE mesh (right)

Fig. 15 – Global deformations u in the form-finding
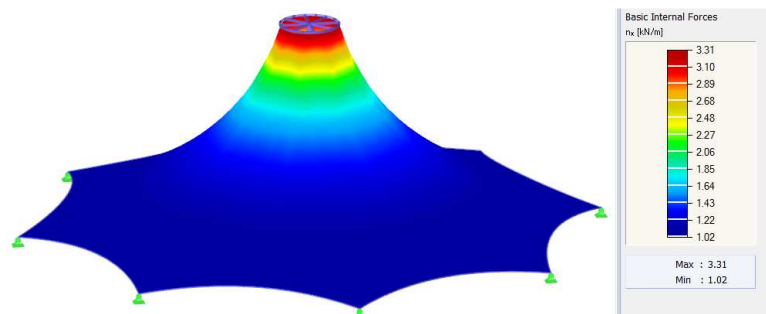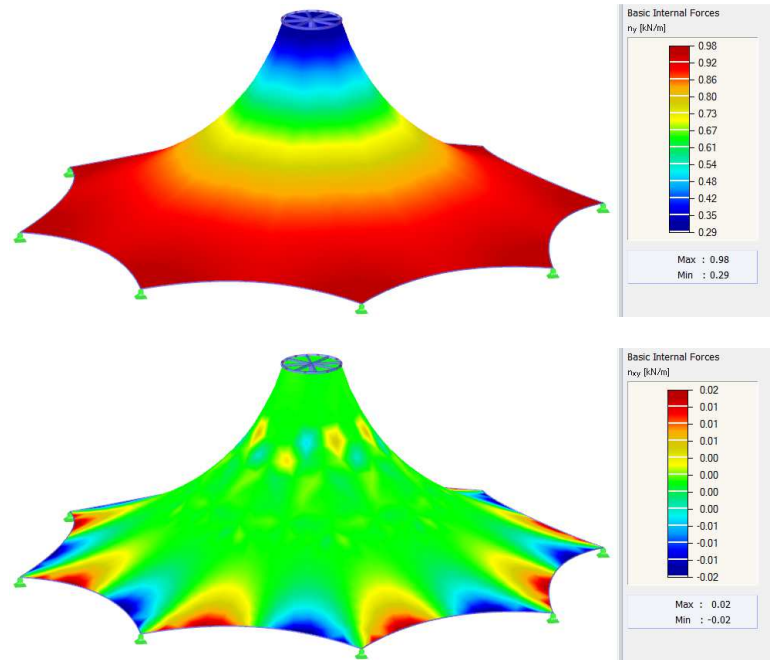
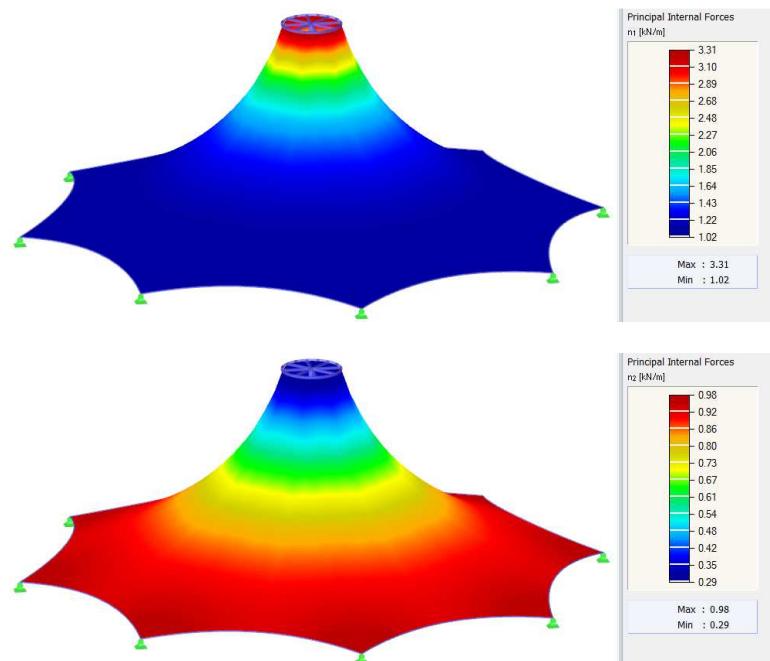*Fig. 16 – Basic internal forces n_x, n_y, n_{xy}*

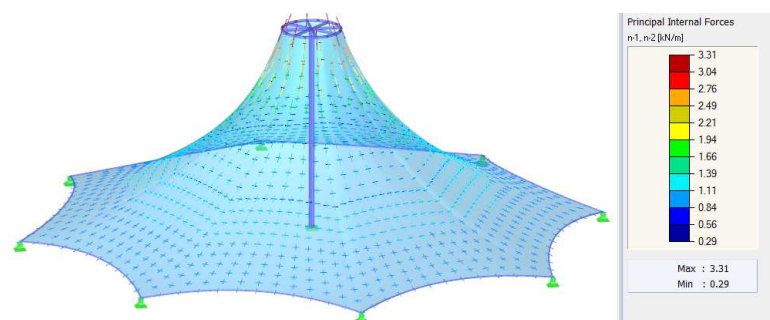*Fig. 17 – Principal internal forces n_1, n_2*

Fig. 18 – Vectors of the principal internal forces n_1, n_2

When deciding whether the concentrations are necessary or not, the following formula is useful. It states the equilibrium in the node of the surface,

$$\frac{n_1}{r_1} + \frac{n_2}{r_2} - p = n_1 \cdot k_1 + n_2 \cdot k_2 - p = 0 \qquad (3)$$

where k_1, k_2 are the principal curvatures, r_1, r_2 are the radii in these directions, n_1, n_2 are the forces in these directions, and p is the external load. It is obvious that the forces and curvatures are interconnected. Now, the case of anticlastic shapes (hypar, cone, etc.) will be considered, where forces in warp and weft act in opposite directions. If there is no need to change the curvatures of the surface, there is no need for concentrations as it is the case of hypar structures, for example (*Fig. 7, Fig. 8, Fig. 11 - Fig. 13*). If there is a need to change the curvatures rapidly in order to reach the required geometry, the concentrations are natural. This is the case of the cone structures (*Fig. 16 - Fig. 18*) where the tangential curvatures must be increased and the radial curvatures must be decreased when reaching the top ring (as we can imagine, the circles that will be created when the cone is intersected by horizontal planes, or the curved lines that will be created when the cone is intersected by a vertical plane).

The form-finding analysis exhibits some phenomena, such as the independence on the material, or the independence of the initial position of the model, for example. This is consistent with the statements in the theoretical part of this chapter that the shape in equilibrium is given by the internal forces, boundary conditions and the external load, if considered. The independence of the initial position will be proved by the following example of a hypar structure with two different initial geometries.
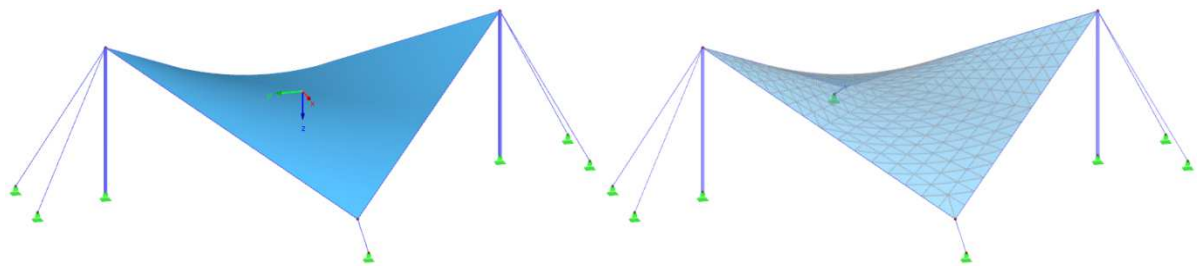

Fig. 19 – First initial shape of the hypar membrane structure with the x/y (warp/weft) orientation displaying (left), FE mesh (right)
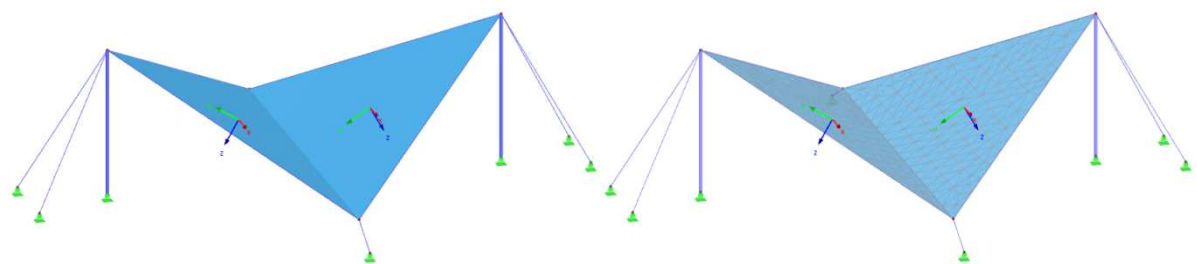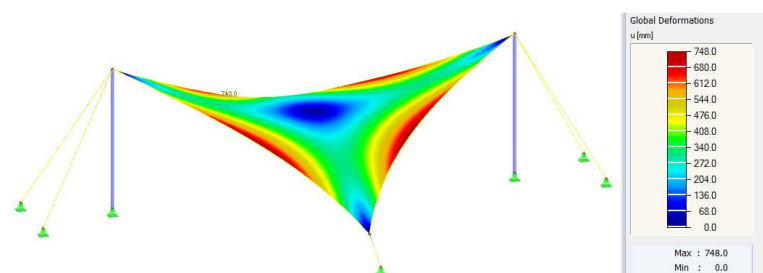

Fig. 20 – Second initial shape of the hypar membrane structure with the x/y (warp/weft) orientation displaying (left), FE mesh (right)
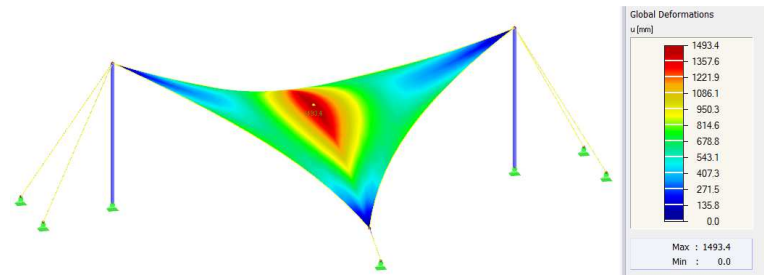
Fig. 21 – Global deformations u in the form-finding of the first (above) and the second (below) membrane structure
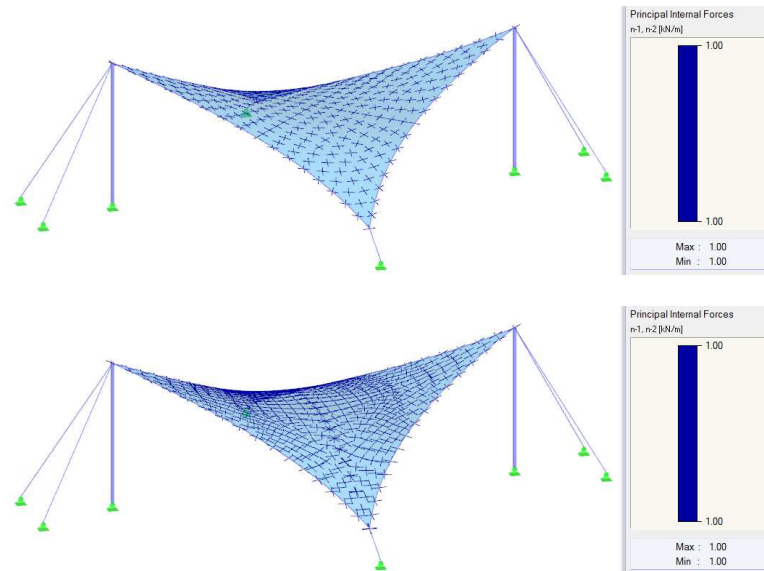

Fig. 22 – Vectors of the principal internal forces n_1, n_2 of the first (above) and the second (below) membrane structure

2.2.2 Pneumatic Structures

There are many different inflated structures types, such as those shown below. These structures are usually subjected to the overpressure; however, the cases with the inside pressure lower than the outside pressure are also possible (*Fig. 23*).
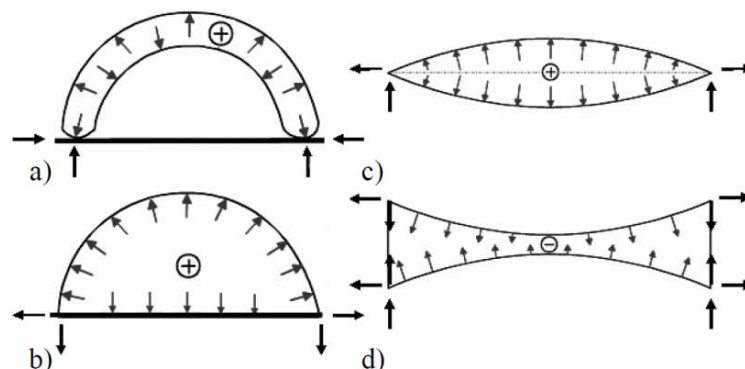

Fig. 23 – Pneumatic prestressed and stabilized structures (+ overpressure, − low pressure) [21]

An example of an air supported cushion will be presented below. This cushion is a part of the membrane structure presented in the subchapter *2.2.3 Full Interaction with Supporting Structures*. The input data for the form-finding process are the isotropic prestress of magnitude $n_x = n_y = 1.00\ kN/m$ and the overpressure $p_o = 250.00\ Pa$.
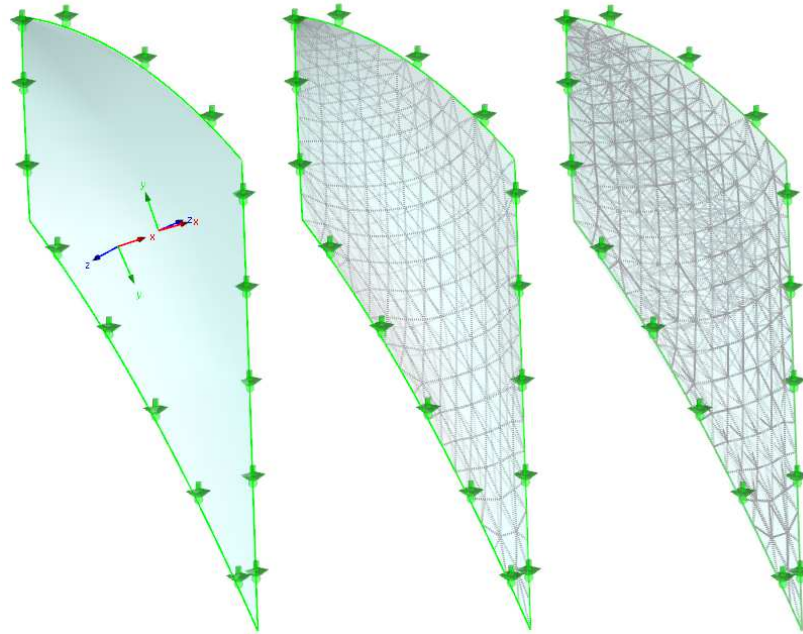
Fig. 24 – ETFE cushion with the axis orientation displaying (left), FE mesh of the layers (middle), FE mesh of the air chamber (right)

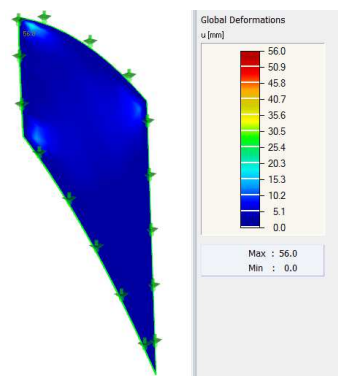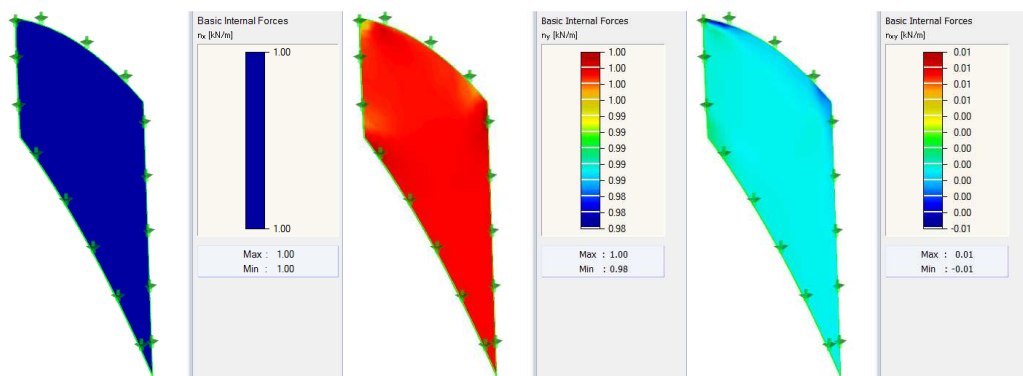*Fig. 25 – Global deformations u*

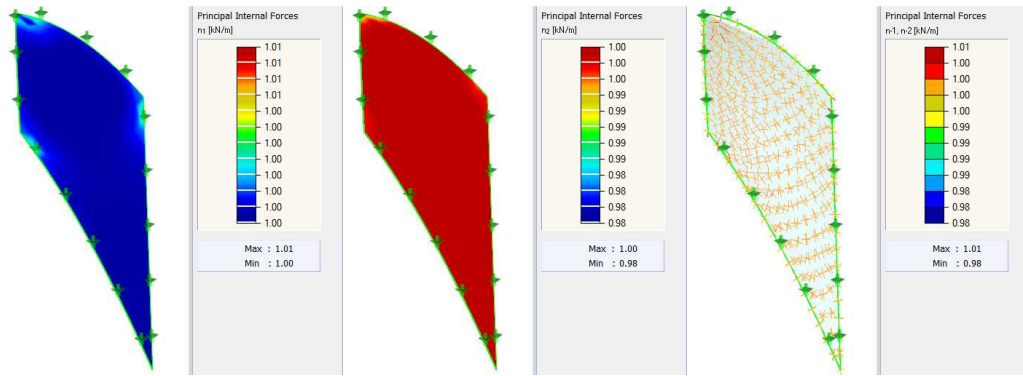*Fig. 26 – Basic internal forces n_x, n_y, n_{xy}*

Fig. 27 – Main internal forces n_1, n_2 and vectors of the main internal forces
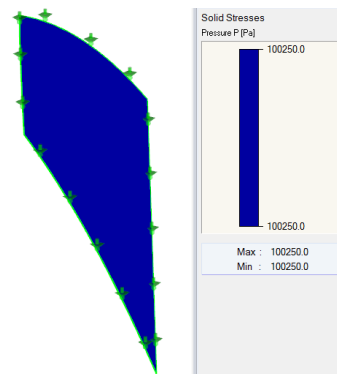

Fig. 28 – Total pressure $p = p_a + p_o$ (p_a...atmospheric pressure + p_o...overpressure)

The presented pressure is the overall pressure, and it is a summation of the atmospheric pressure and the overpressure defined for the form-finding. In this example, the atmospheric pressure is $p_a = 100\ 000.00\ Pa$.

It is not a problem to create any other example of the pneumatic structure and use the positive or the negative overpressure without any problems. The input for the gas chamber can be defined as the pressure or the required volume. The pneumatic structures will be described by two further subchapters *3.2.3 Pneumatic Structures* and 3.2.4 *Analysis of Pneumatic Structure*, presenting other possibilities and behaviour.

2.2.3 Full Interaction with Supporting Structures

As mentioned in the theoretical part of this chapter *Form-finding,* the full interaction of structural parts subjected to the form-finding with the parts, which are usual structural elements, is possible in the global nonlinear analysis. Such examples for both, the pneumatic and tensioned membrane structures, will be presented below.

The first example to be presented is a greenhouse made of steel arches, ETFE cushion of two layers and wooden shells. The internal overpressure is $p_0 = 250.00\ Pa$, the prestress of ETFE layers is $n_x = n_y = 1.00\ kN/m$. The greenhouse geometry is presented below (*Fig. 29, Fig. 30*) as well as some results of the form-finding process (*Fig. 31 - Fig. 39*), which takes into account the entire structure.
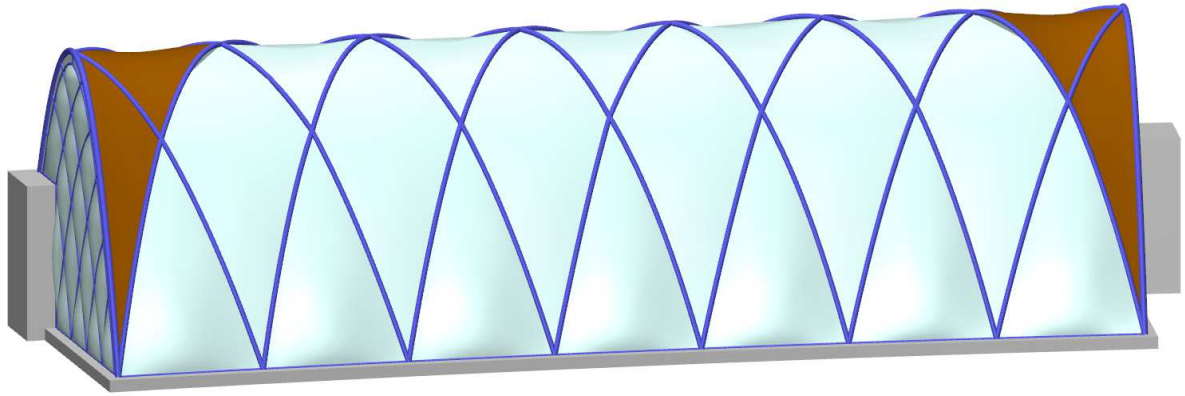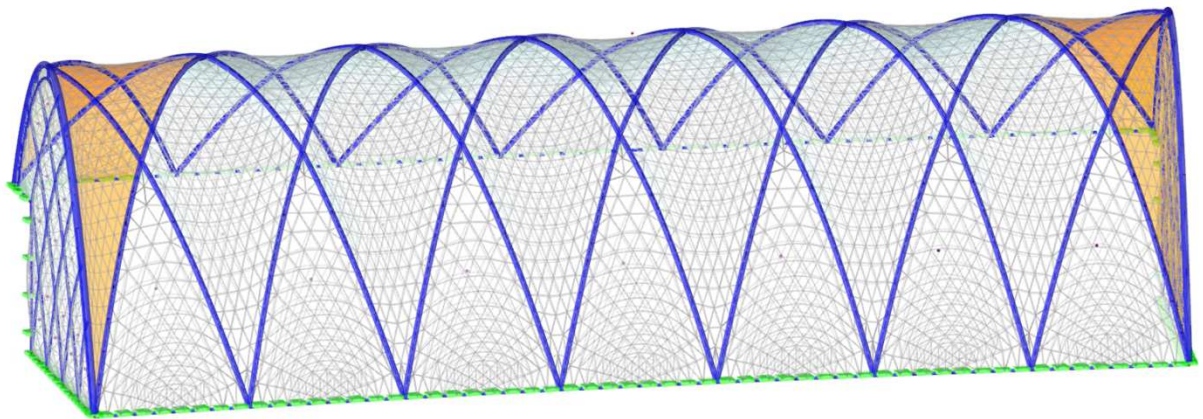
Fig. 29 – Geometry of the greenhouse structure

Fig. 30 – FE model of the greenhouse structure (1221 1D elements, 16508 2D elements, 20172 3D elements)
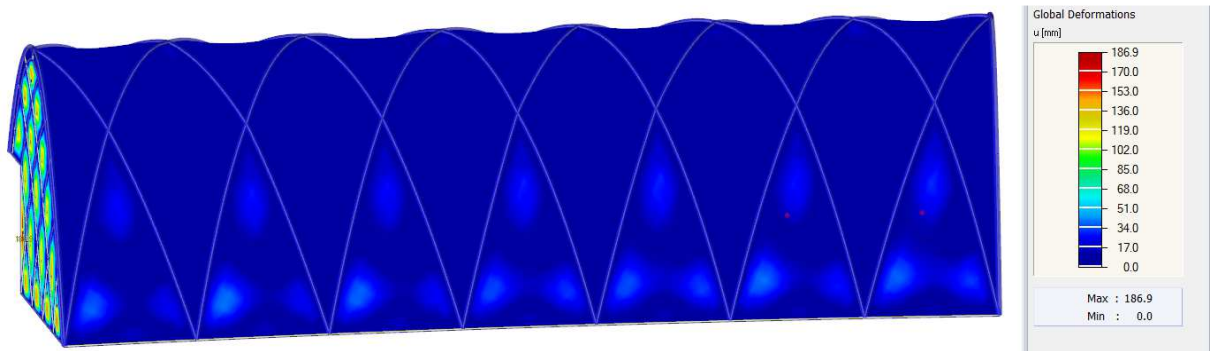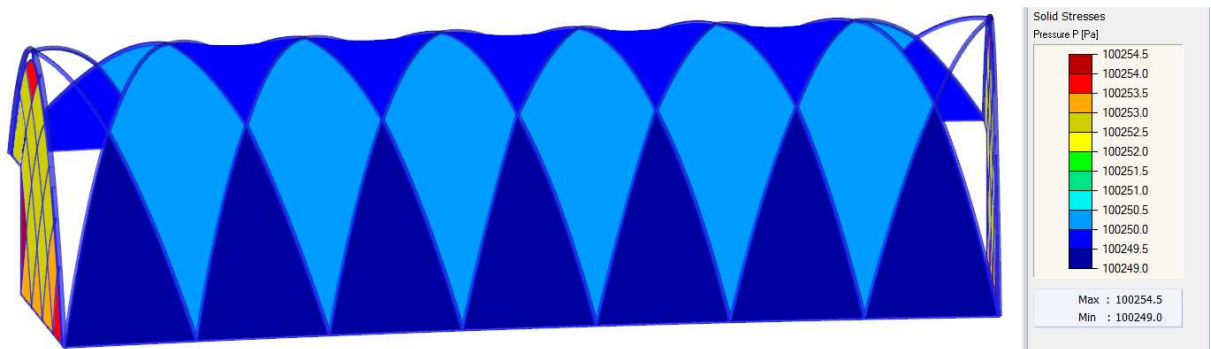

Fig. 31 – Global deformations u

Fig. 32 – Total pressure $p = p_a + p_o$ (p_a...atmospheric pressure + p_o...overpressure)

As well as in the previous subchapter *2.2.2 Pneumatic Structures*, the presented pressure is an overall pressure. The atmospheric pressure is $p_a = 100\,000.00\,Pa$ here. The values in the figure (*Fig. 32*) approximate the required value $p = 100\,250.00\,Pa$. The higher precision can be used for closer approximation of the required values.

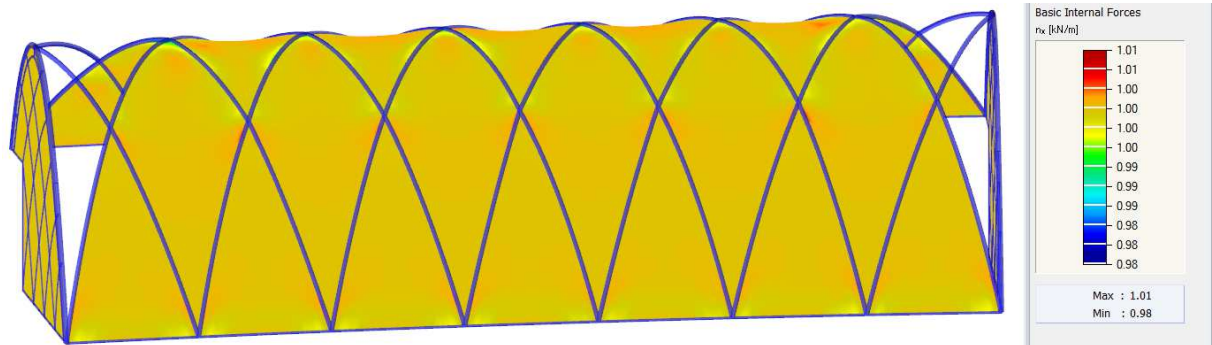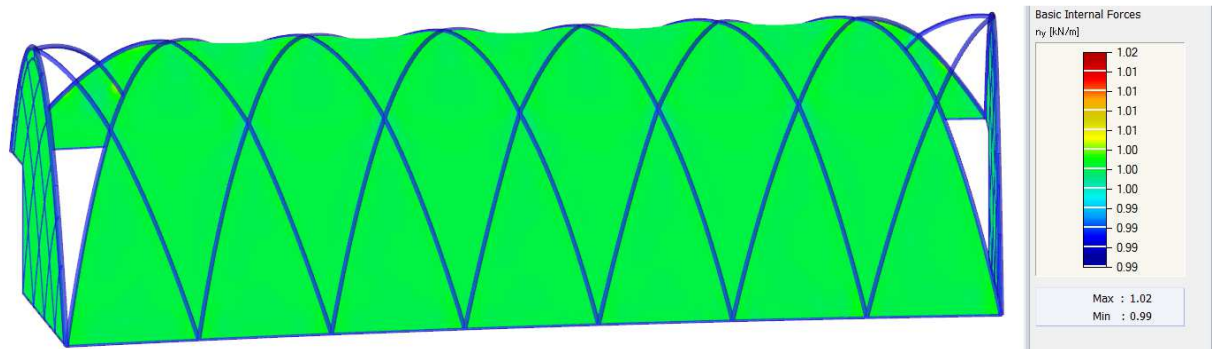*Fig. 33 – Basic internal forces n_x in the ETFE layers*

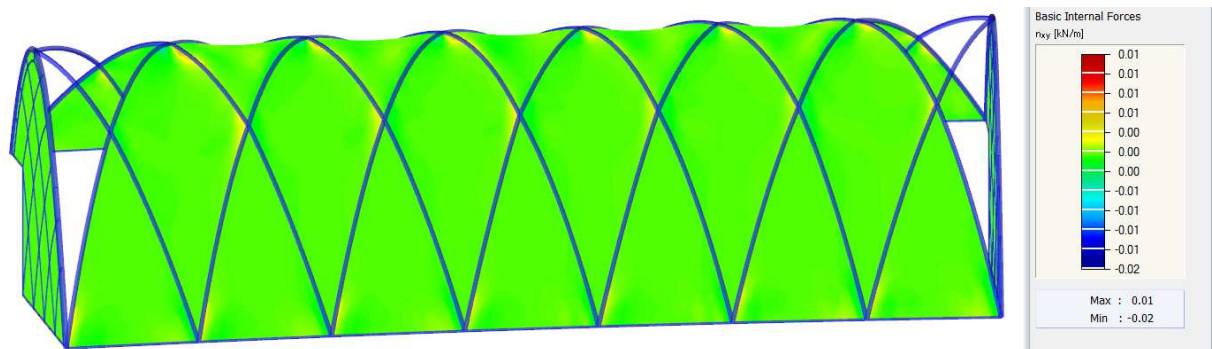*Fig. 34 – Basic internal forces n_y in the ETFE layers*

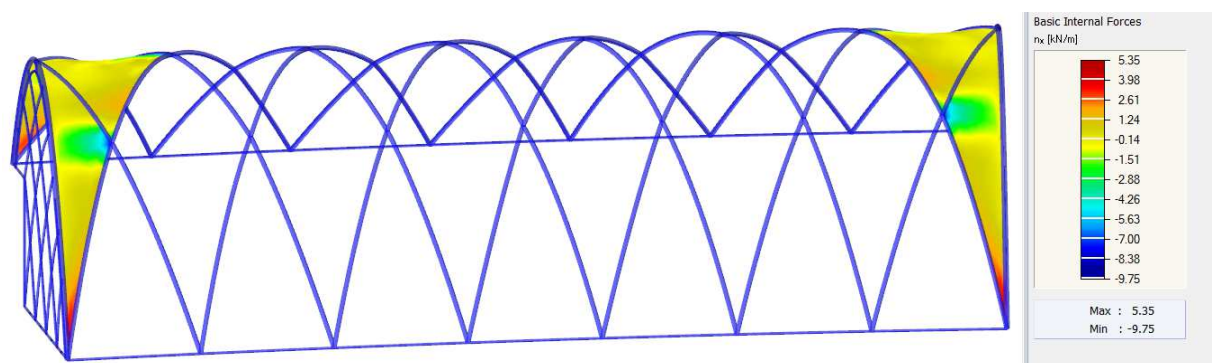*Fig. 35 – Basic internal forces n_{xy} in the ETFE layers*

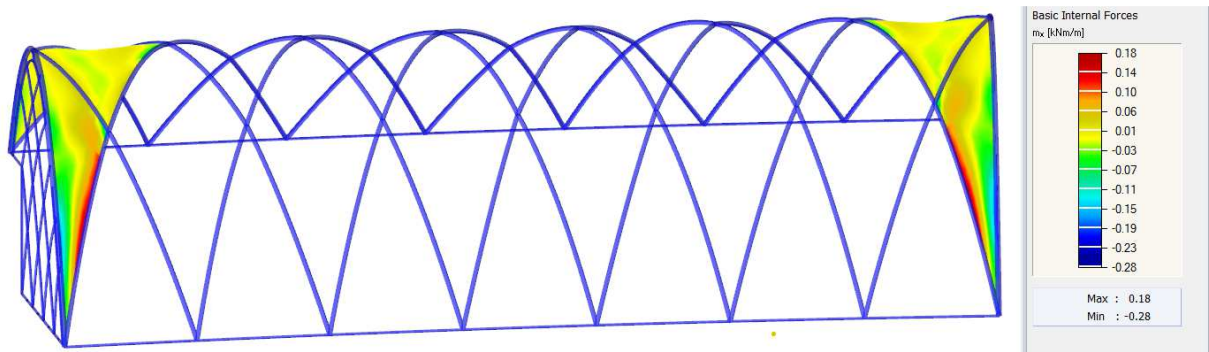*Fig. 36 – Basic internal forces n_x in the wooden shells*

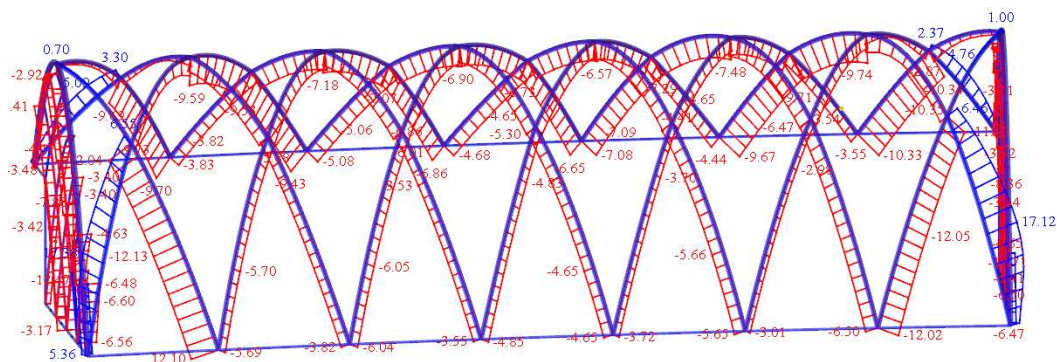*Fig. 37 – Basic internal forces m_x in the wooden shells*
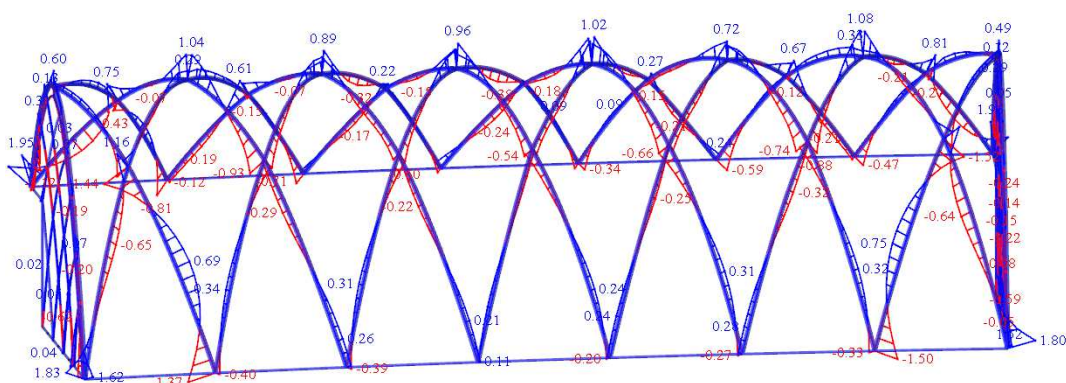

Fig. 38 – Normal forces N

Fig. 39 – Bending moments M_y

As presented above, the complex structure of the greenhouse can be subjected to the form-finding analysis and at the same time, the nonlinear analysis of the supporting structure is performed. The resulting internal forces in the ETFE foils and wooden parts were presented separately since higher values of normal forces appear in the wooden shells than in the ETFE foil, and the mixed display would not be very clear.

Further, the example of mechanically prestressed structure will be shown. This structure is composed of four conical parts, which are complemented by eight saddle shaped parts. The conical parts are supported by four columns fixed on the ground, the columns supporting the hypar parts are pin-jointed to the ground and each of them is fixed by two cables (*Fig. 40, Fig. 41*). The prestress in warp and weft is $n_x = n_y = 1.00\ kN/m$. The stabilization of conical parts is used to obtain the necessary concentrations near the top rings. Only those positions need concentrations, which cannot be avoided. Other parts do not need any concentrations, so the smooth prestress is the result of the form-finding process as can be seen below (*Fig. 43 - Fig. 48*).
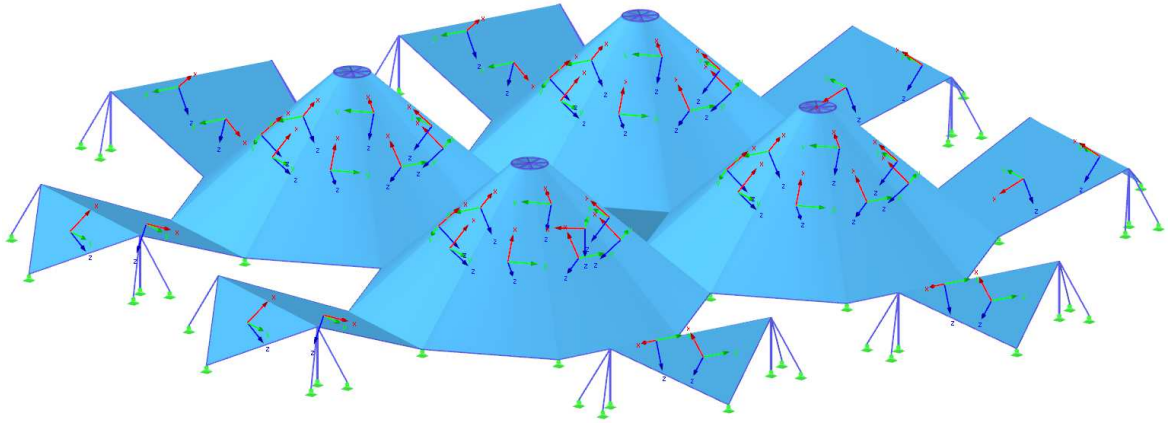
Fig. 40 – Initial shape of the membrane structure with the warp/weft orientation displaying
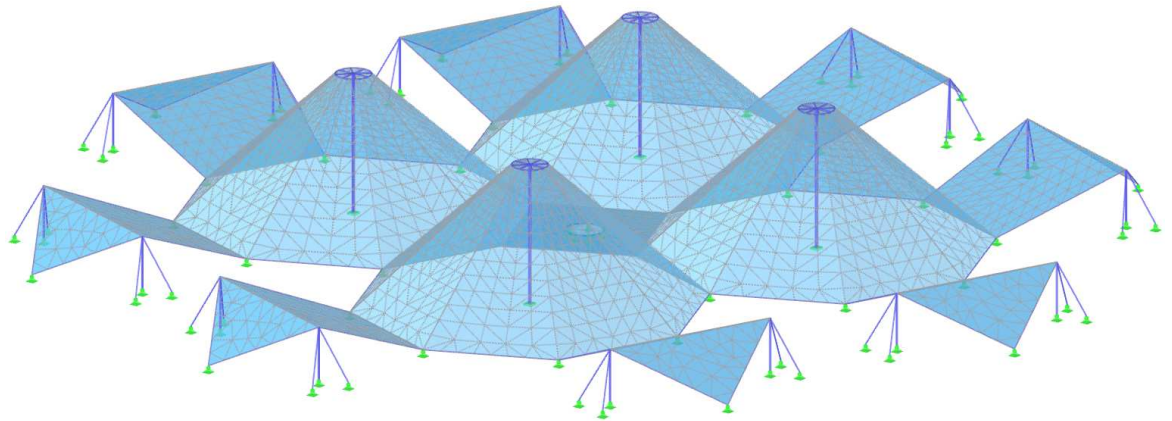
Fig. 41 – FE mesh of the membrane structure in the initial position
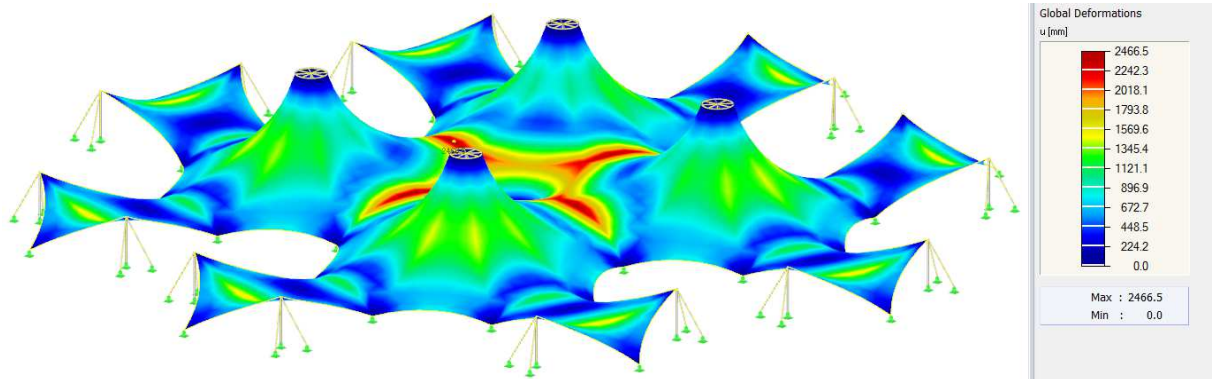
Fig. 42 – Global deformations u in the form-finding
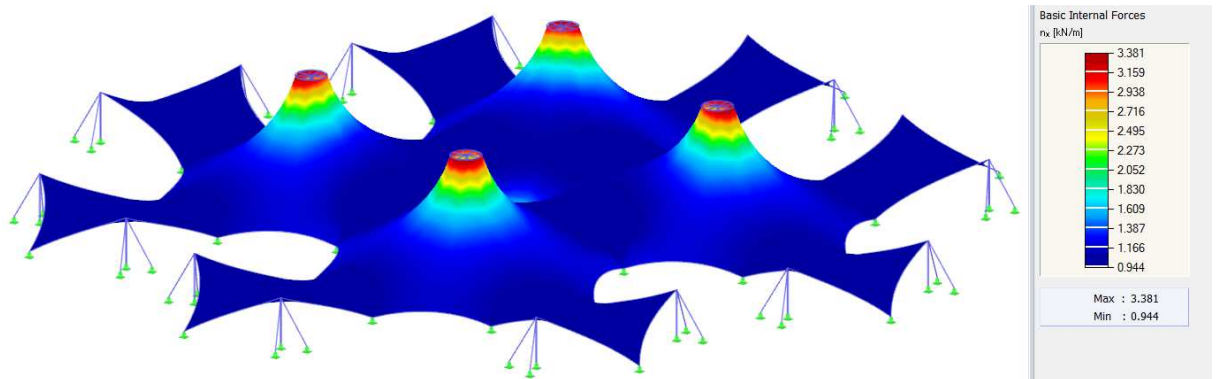
Fig. 43 – Basic internal forces n_x
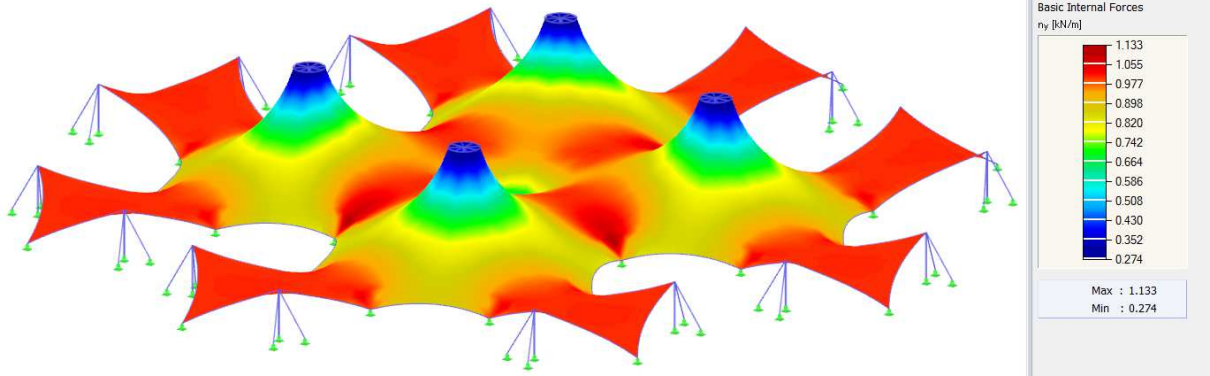
Fig. 44 – Basic internal forces n_y
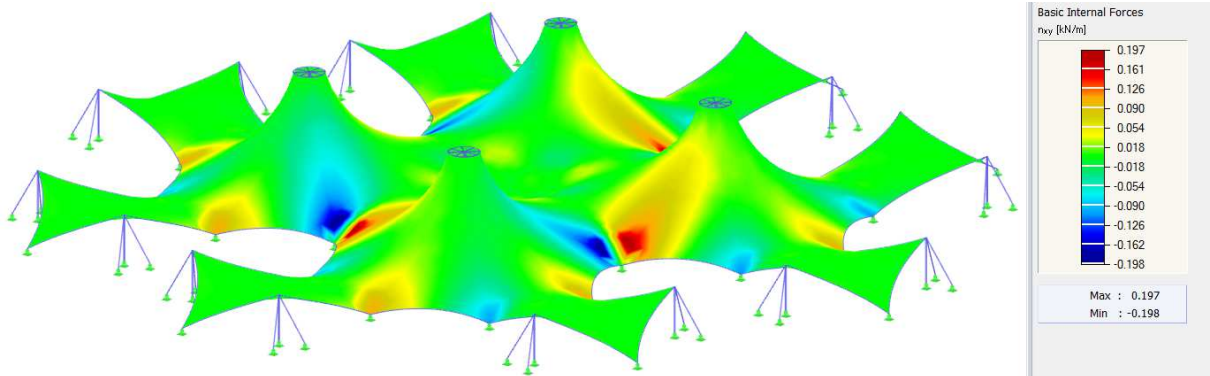
Fig. 45 – Basic internal forces n_{xy}
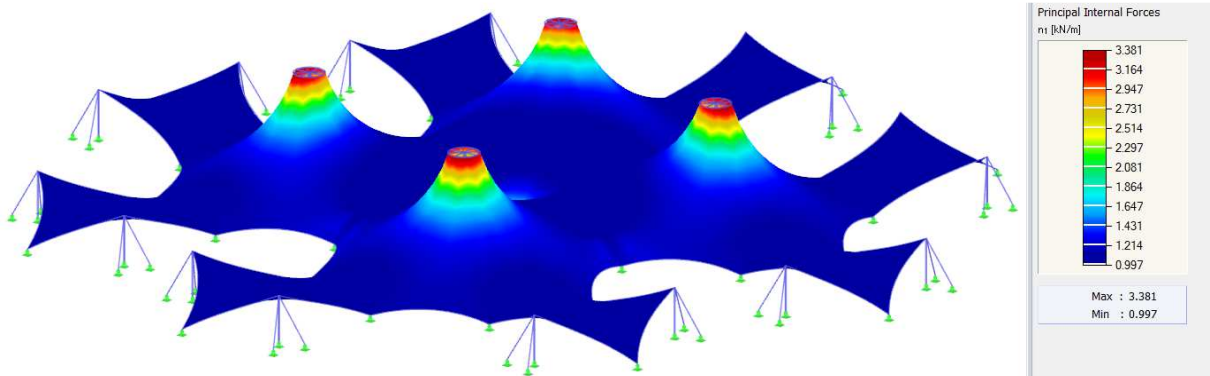
Fig. 46 – Principal internal forces n_1
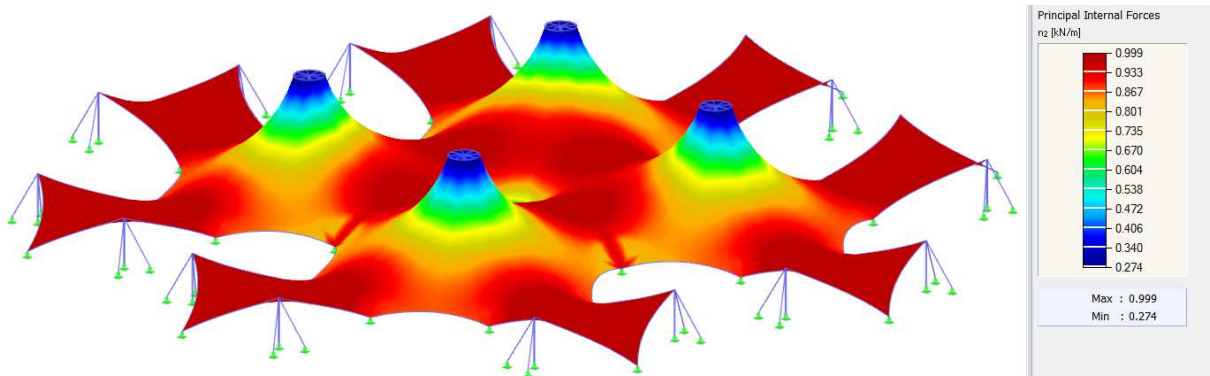
Fig. 47 – Principal internal forces n_2
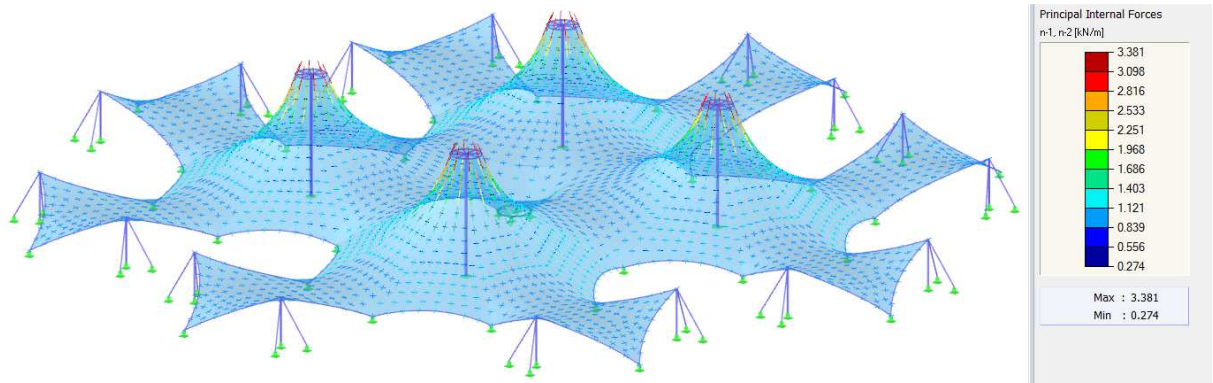
Fig. 48 – Vectors of principal internal forces n_1, n_2

The prestress values that are close to the prescribed ones can be seen when moving away from the top rings.
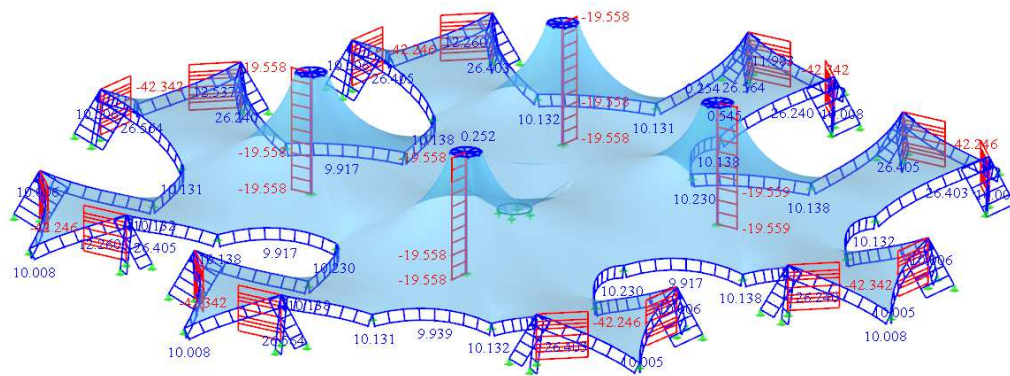
Fig. 49 – Normal forces N
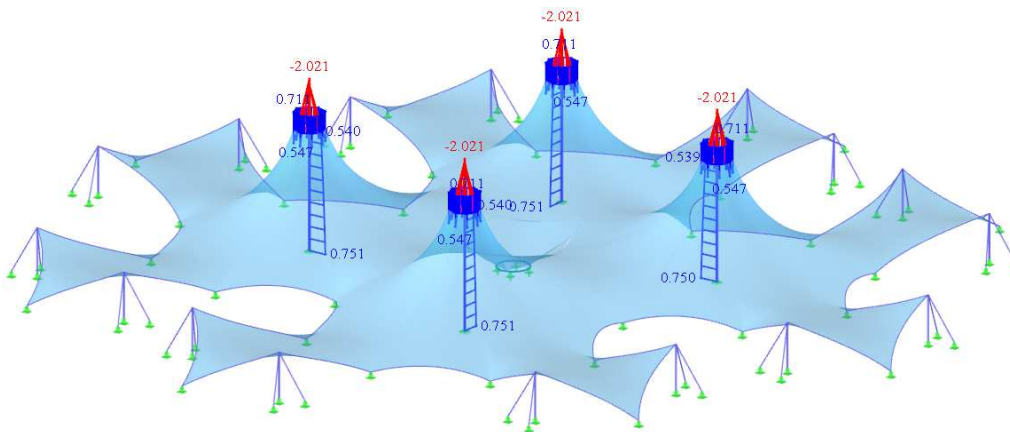
Fig. 50 – Bending moments M_y

The last three figures show the shape of the membrane structure after the form-finding process as contour lines and slopes. These values could be of use when loading the structure, for example in the case of the snow accumulation in the blue parts of the figure *Slopes of the surface* (*Fig. 52, Fig. 53*) since the surface has really low inclinations in these positions.
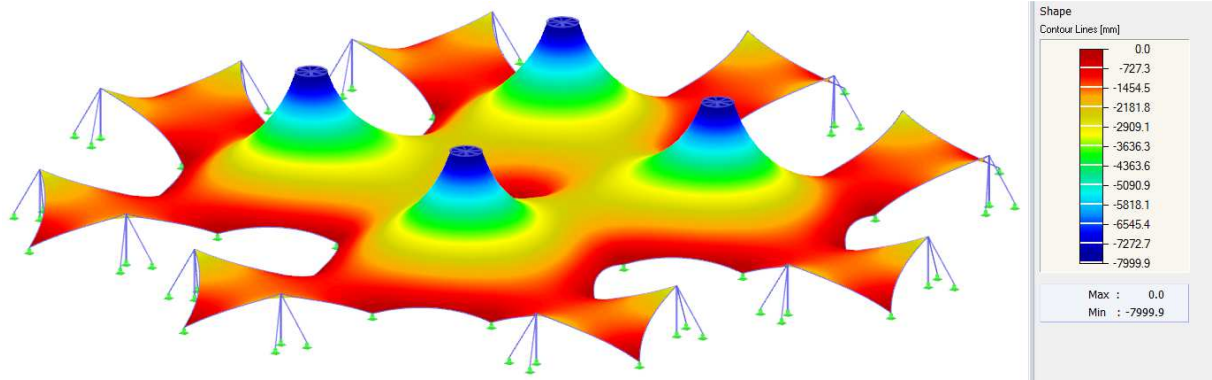
Fig. 51 – Contour lines on the surface
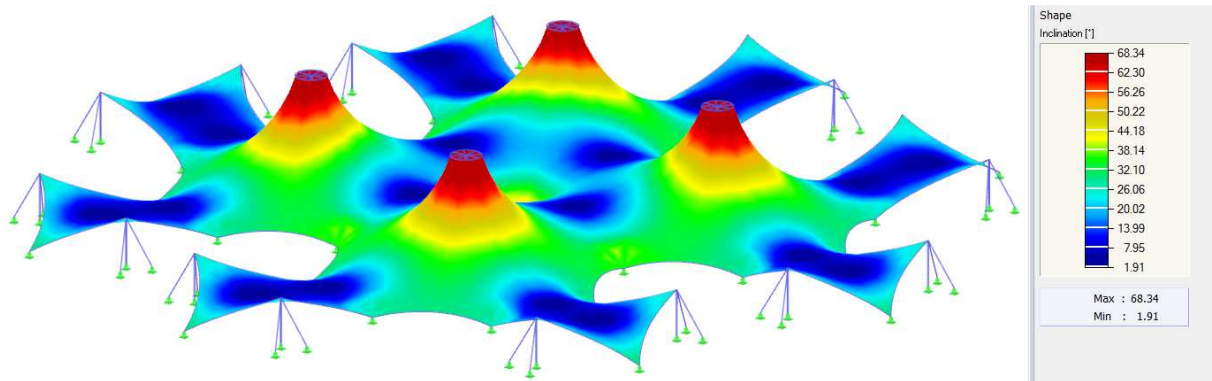
Fig. 52 – Slopes of the surface
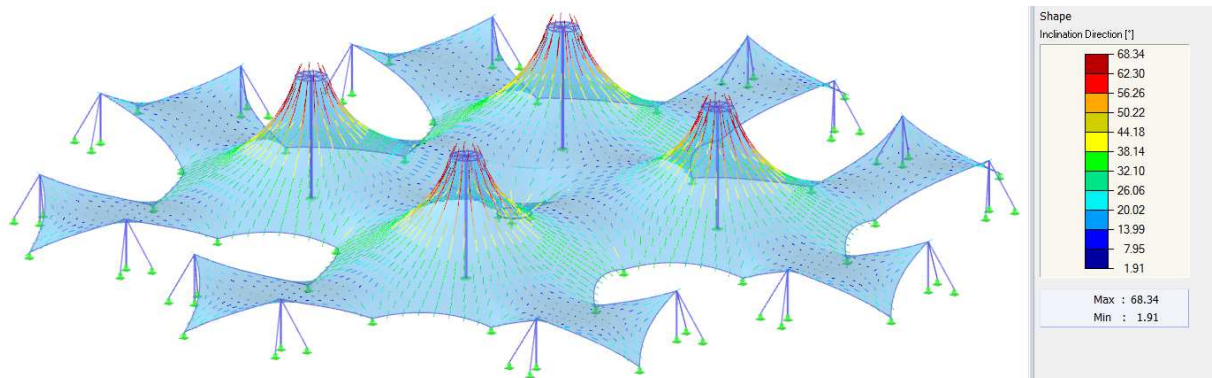
Fig. 53 – Vectors of the slopes of the surface

The membrane structure was created in its initial position (*Fig. 40, Fig. 41*) and the form-finding process deformed the mesh into a new/equilibrium position according to the defined prestress. This new position is an initial state for further structural analysis. Since the loads are placed on the surfaces/beams and then transferred to the mesh, the difference between the initial position of the model and the new/real position of the mesh can be confusing for an engineer or architect. Because of this fact, the function of NURBS transformation was developed in the RFEM software. This feature transfers the model in the initial position into the new position according to the mesh deformation. Then, the FE mesh is regenerated and a new form-finding is calculated. The resulting shape will be the same as well as the prestress. The calculation with/without the use of the NURBS transformation makes no difference in the physical meaning of the task. However, it is really helpful to unify the model with the equilibrium position in order to facilitate the loading process. There is only one limitation: the surfaces to be transformed can have 3 or 4 boundary lines as it is a limitation according to the mathematical definition of the surface, which defines a NURBS surface for 4 boundary

lines. If one of them is degenerated into a node, it is also possible to have 3 boundary lines. This transformation was used for the presented example and the final geometry of the model can be seen below (*Fig. 54, Fig. 55*).
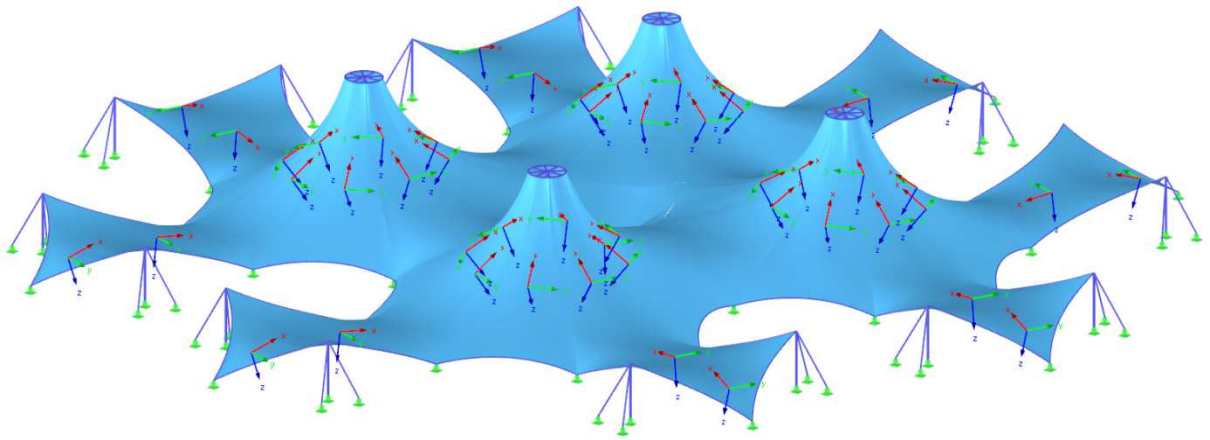
Fig. 54 – Transformed shape of the membrane structure with the warp/weft orientation displaying (NURBS surfaces/lines)
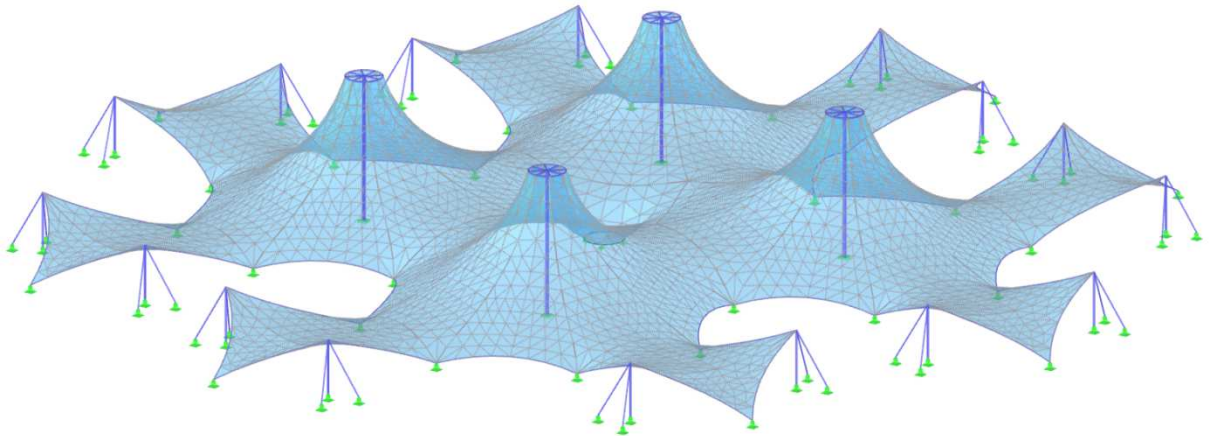
Fig. 55 – FE mesh of the membrane structure after the transformation (NURBS surfaces/lines)

2.2.4 Shell Structures

In the following, the shell structure with boundary beams (*Fig. 56*) will be subjected to the form-finding process. The required normal forces of the shell are $n_x = n_y = -4.00 \ kN/m$ and $N = -40.00 \ kN$ for the beams. The self-weight is considered in the form-finding process as the structure is subjected to virtually pure compression under this permanent load.

As you can see below, the values of the normal forces approximate the prescribed values, while bending moments and shear perpendicular to the surface are near to zero. The same can be observed for the beams, where the normal forces approximate the required values while the bending moment is near to zero.
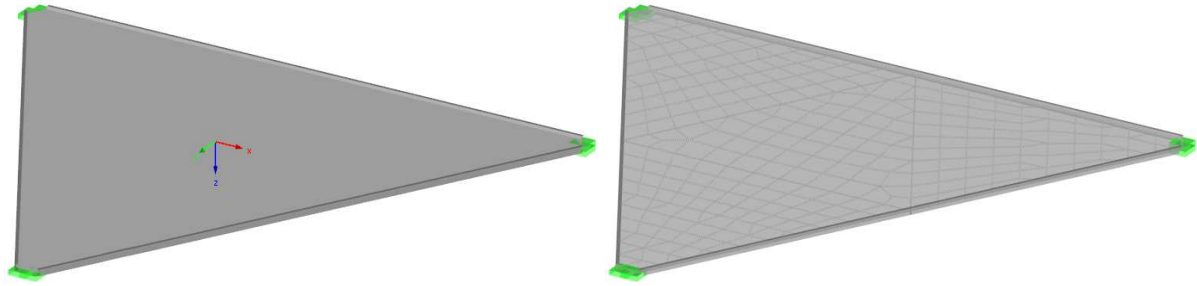
Fig. 56 – Initial shape of a shell structure with the axis orientation displaying, FE mesh
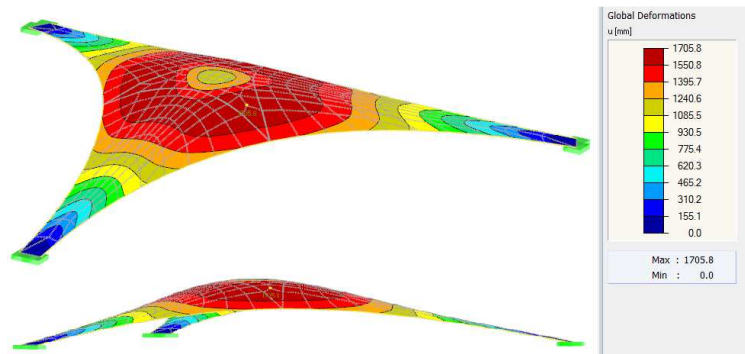
Fig. 57 – Two views of global deformations u in the form-finding
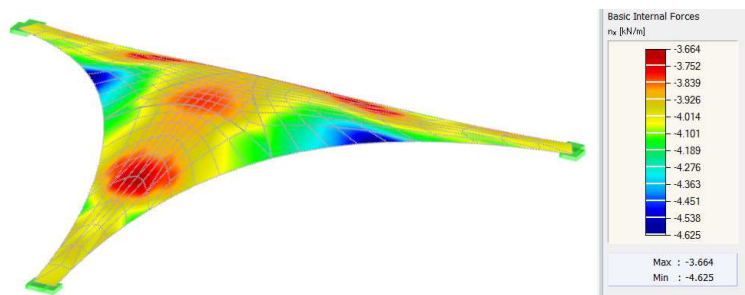
Fig. 58 – Basic internal forces n_x
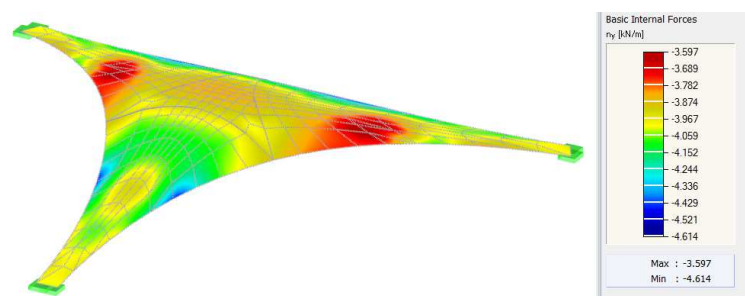
Fig. 59 – Basic internal forces n_y
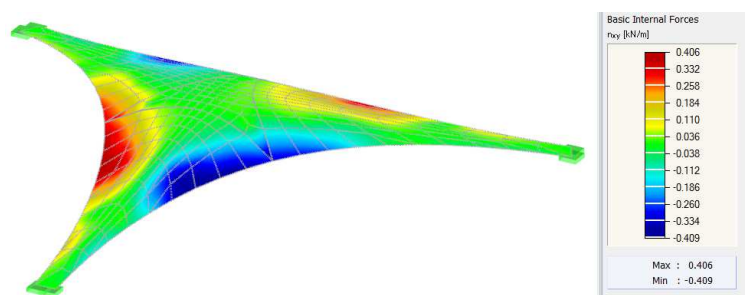
Fig. 60 – Basic internal forces n_{xy}
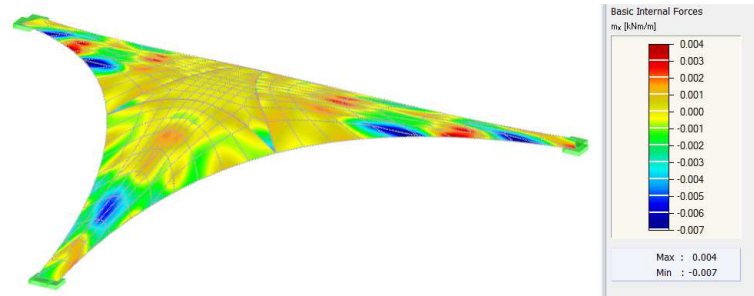
Fig. 61 – Basic internal forces m_x
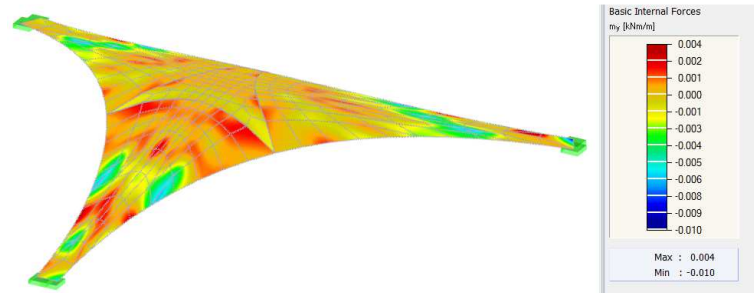
Fig. 62 – Basic internal forces m_y
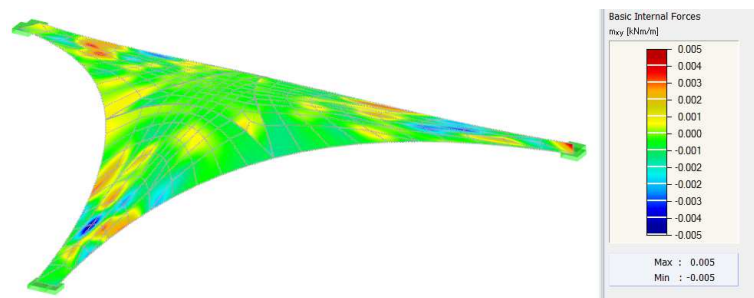
Fig. 63 – Basic internal forces m_{xy}
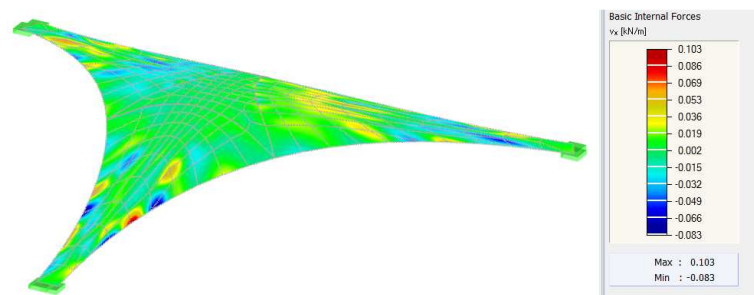
Fig. 64 – Basic internal forces v_x
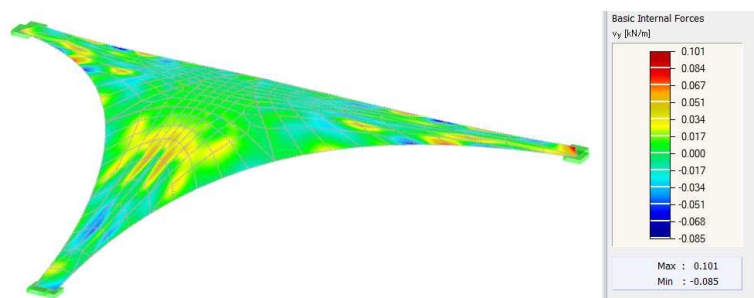
Fig. 65 – Basic internal forces v_y
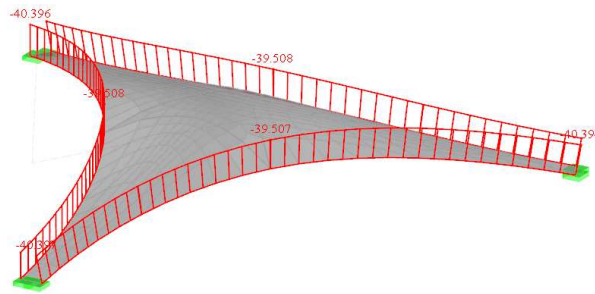
Fig. 66 – Normal forces N
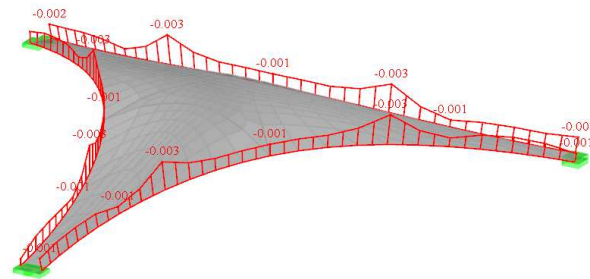
Fig. 67 – Bending moments M_y

2.2.5 Combined Structures

In the previous text, the form-finding process of tensioned structures was shown for both mechanically prestressed membranes and pneumatic structures. Further, the possibility of the form-finding analysis for a structure under compression was presented, and the shell structure with boundary beams was shown. In the theoretical part, there is mentioned that the form-finding process of the structures under compression is susceptible to instability as the unstable equilibrium position of the structure is searched for. Any deviation causes pushing the structure away from the steady state that should be found (*Fig. 4*). A well-known stabilization of inverting the negative input values for shells into positive forces with simultaneous load reversal is only applicable to compression-only constructions (*Fig. 56*). However, a combined structure (*Fig. 68*) with both positive and negative forces entered for the shape analysis cannot use this stabilization. Based on that fact, the local stabilization of the unstable part was developed in the RFEM software in order to find the equilibrium shape of such structures. However, unstable cases for such an analysis can still appear due to the complexity and the physical sensitivity of the task described above.

In the following, a membrane structure with orthotropic prestress with magnitudes in warp $n_x = 2.50 \ kN/m$ and weft $n_y = 2.00 \ kN/m$ is analysed. The requirements for cables are the sag magnitudes $s = 10.0 \ \%$, as both the force and the geometry (sag/length) can be the form-finding input. The geometrical input was also used for the two steel arches, where the unchanged length is required. The structure is subjected to the form-finding process and compared to the structure, where the shape of steel arches is not analysed but given. The differences of shapes and internal forces in the beams are obvious (*Fig. 70, Fig. 72 - Fig. 74*). While the arches with given shapes are subjected to the bending moments and shear forces, those quantities are almost zero in the case of arches with the shape according to the form-finding analysis. By this way, the combined structure can be optimized to be subjected axial forces for specific load assumption only.
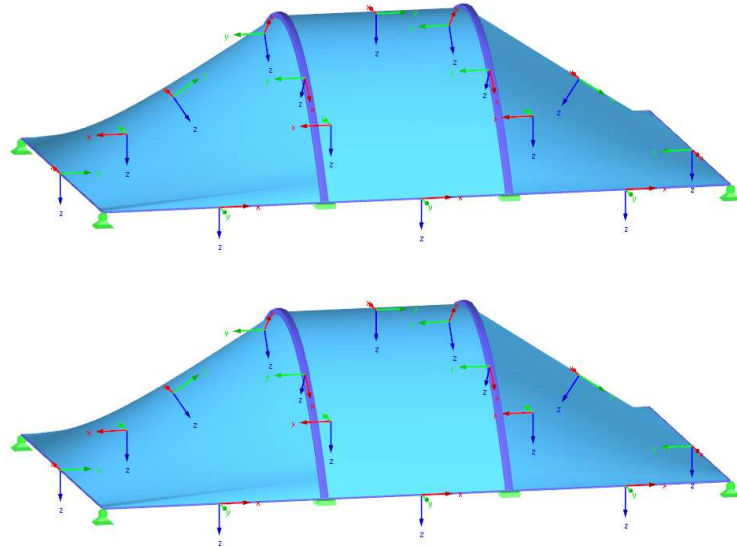
Fig. 68 – Initial shape of the membrane structures displayed with the x/y (warp/weft) orientation and beam axes, the structure with (above) and without (bellow) the analysis of the shape of steel arches
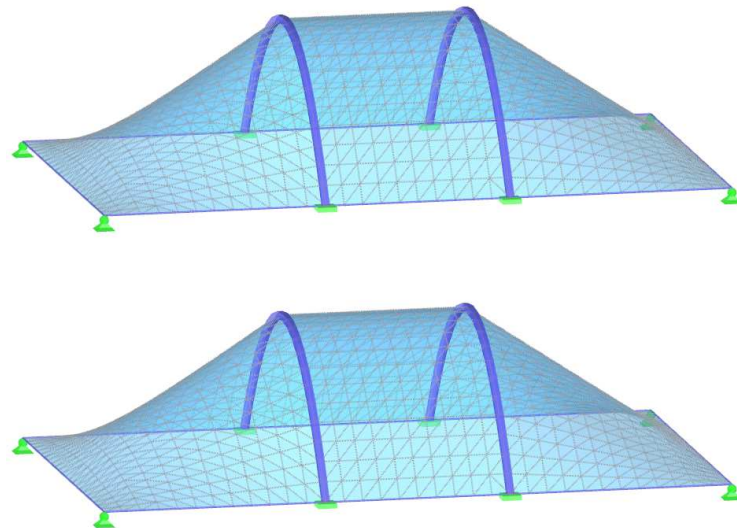
Fig. 69 – FE mesh of the membrane structures in the initial position, the structure with (above) and without (bellow) the analysis of the shape of steel arches
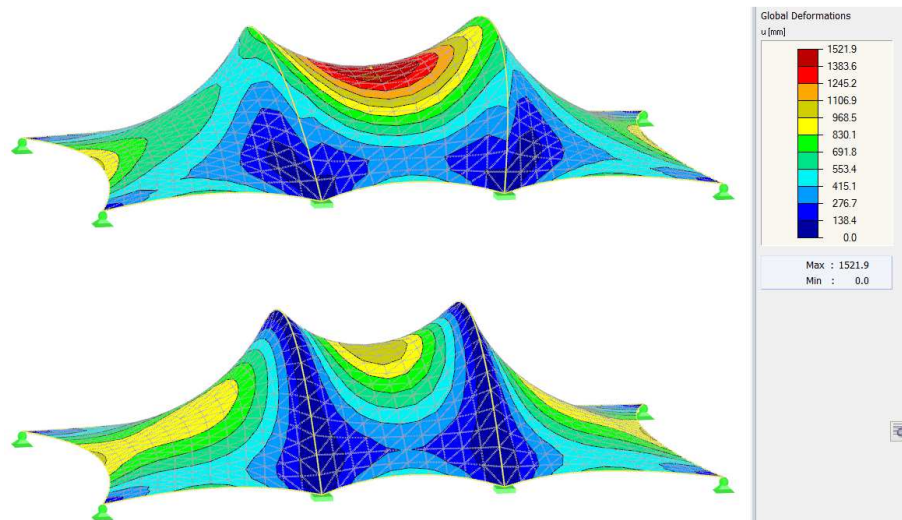
Fig. 70 – Global deformations u during the form-finding, the structure with (above) and without (bellow) the analysis of the shape of steel arches
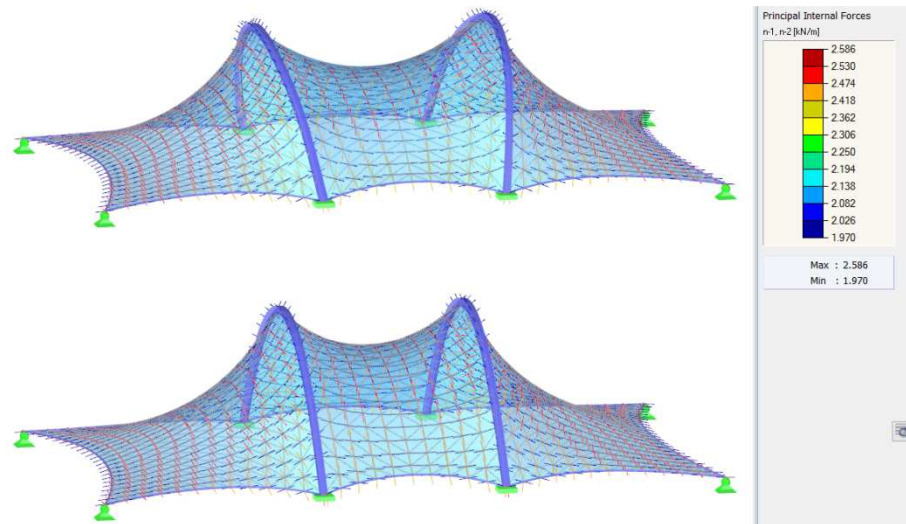
Fig. 71 – Vectors of the principal internal forces n_1, n_2, the structure with (above) and without (bellow) the analysis of the shape of steel arches
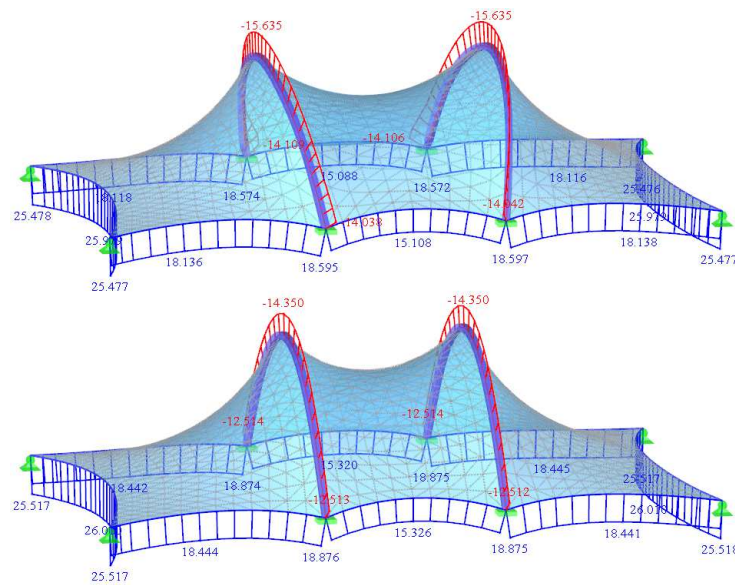
Fig. 72 – Normal forces N, the structure with (above) and without (bellow) the analysis of the shape of steel arches
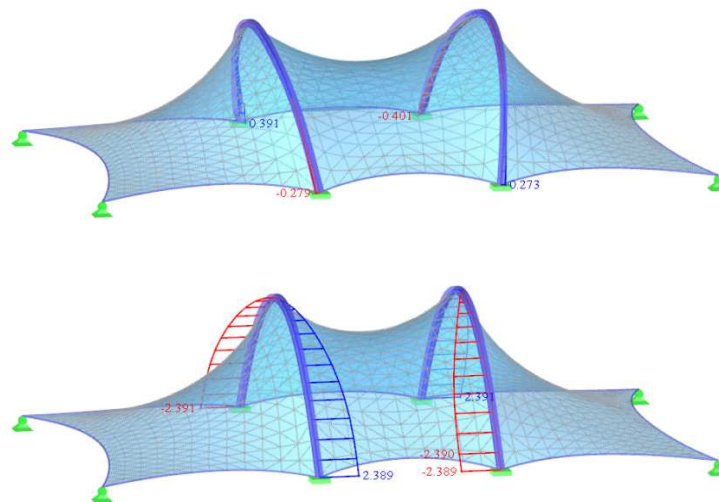
Fig. 73 – Shear forces V_y, the structure with (above) and without (bellow) the analysis of the shape of steel arches
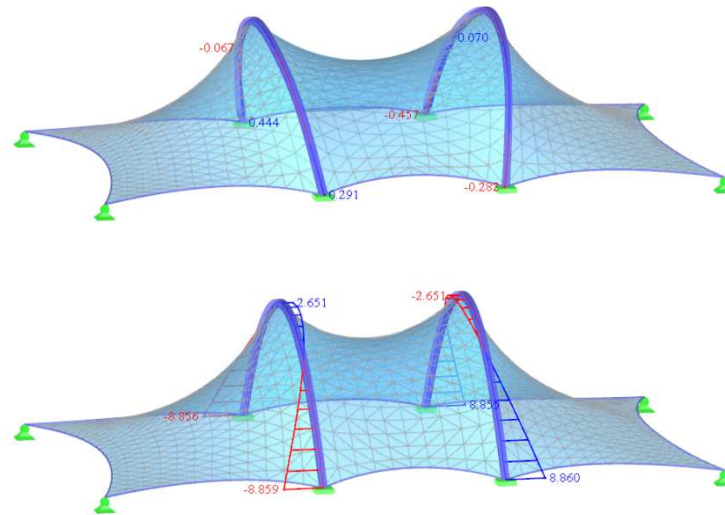
Fig. 74 – Bending moments M_z, the structure with (above) and without (bellow) the analysis of the shape of steel arches

The combined structures exhibit a specific phenomenon that more than one equilibrium position can exist for them (*Fig. 75 - Fig. 77*). In the example presented below, the requirements for the arches are to increase their lengths of $\Delta l = 30.0$ %. Four possible equilibrium positions can be reached (*Fig. 77*), and each initial shape converges to the closest one.
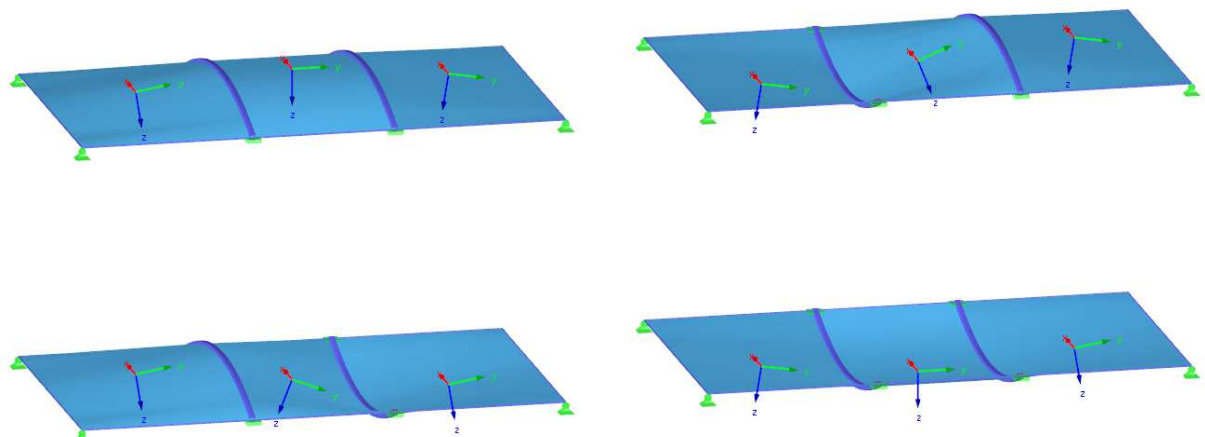
Fig. 75 – Different initial shapes of the membrane structures with the warp/weft orientation displayed
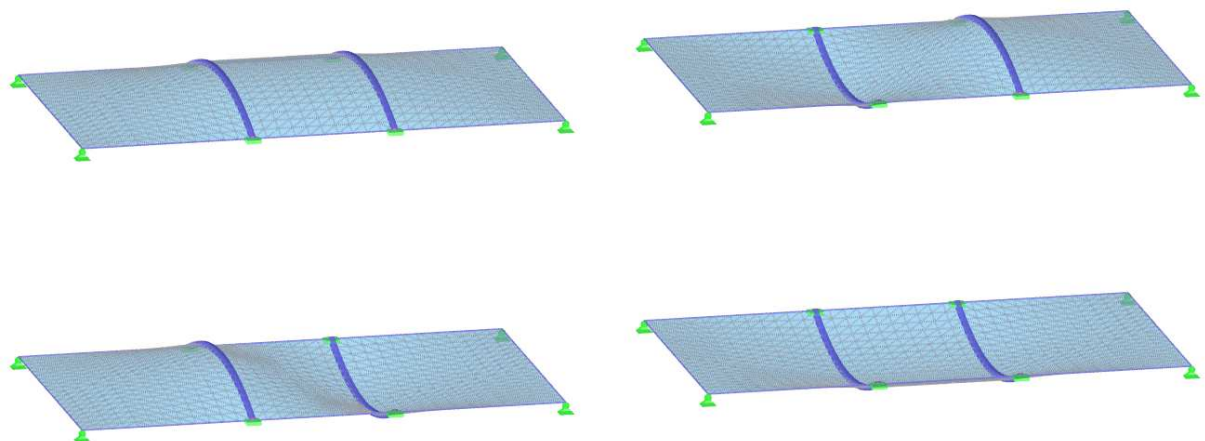
Fig. 76 – FE mesh of the membrane structures in the initial position
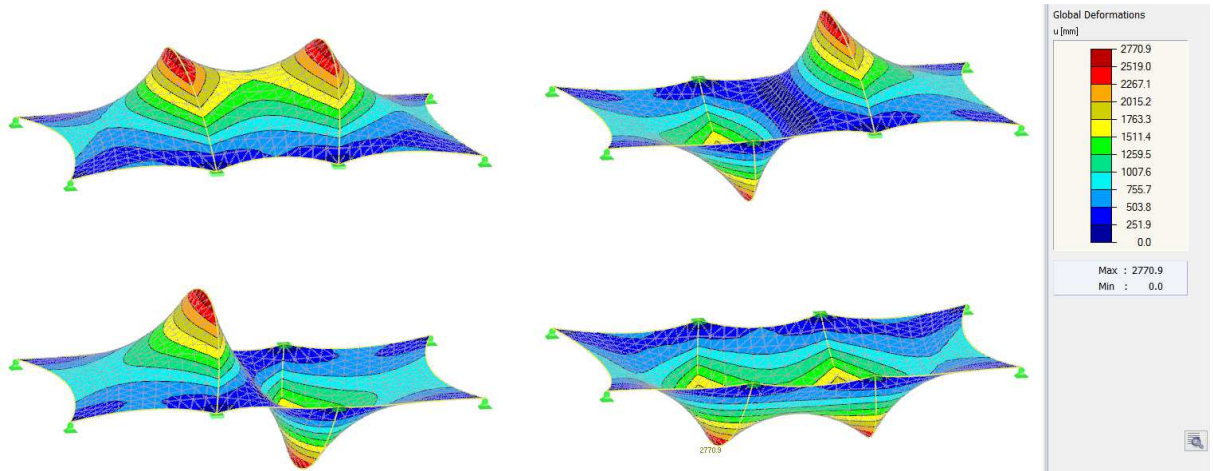
Fig. 77 – Global deformations u *in the form-finding*

3 STRUCTURAL ANALYSIS

The structural analysis of tensile structures exhibits significant nonlinearities. These are caused by both the geometrical changes of the structure during its loading and the non-proportional changes of the internal forces depending on the strains of material because it is necessary to consider at least zero compression resistance. The basic principles of this analysis and FEM will be described in the first part of this chapter *Structural Analysis*. The second part will be focused on practical examples which will complete and illustrate the discussed topics.

3.1 Theory

In the following text, the fundamentals of FEM and nonlinear structural analysis of structures will be described.

3.1.1 Principles of FEM Analysis

When speaking about a general concept of the finite element method, the mathematical nature inheres in what is termed discretisation of the problem. Searching for *unknown functions* in domain $\boldsymbol{\Omega}$ with boundary $\boldsymbol{\Gamma}$ is replaced by searching for a *finite number of values* of these functions or displacement parameters $\boldsymbol{d}$, which can be used to formulate an approximate solution. The decomposition of the *unknown function* is closely related to the division of the domain $\boldsymbol{\Omega}$ into subdomains $\boldsymbol{\Omega_e}$, briefly called *finite elements*, and *base functions* of these finite elements [22].

The basis of numerical software used in practical statics is the deformation variant of the FEM. This method produces well-conditioned equation systems. The core of this method lies in the energetic concept of the problem, generally in the variational formulation of the problem, where we search for an extreme of an operator $\boldsymbol{\Pi}$ that is of additive nature. This means, the value for the whole system (domain) is equal to the sum of values in the subdomains (finite elements) of the system. This nature is characteristic especially for all equations defined by means of any bounded integral in the domain. Thus, as an example, the total potential energy $\boldsymbol{\Pi} = \boldsymbol{\Pi^{int}} + \boldsymbol{\Pi^{ext}}$ of the internal and external forces in the body is minimal just for the real state of the body $(\boldsymbol{d}, \boldsymbol{\varepsilon}, \boldsymbol{\sigma})$, in accordance with the Lagrange variational principle. In this particular situation, the FEM equation can be obtained through the differentiation of the total potential energy $\boldsymbol{\Pi}$ with respect to the individual deformation parameters $d_1, d_2, \dots, d_m, \dots, d_N$, where N is the number of degrees of freedom. Here, the *m-th* equations can be written as [22].

$$\frac{\partial \Pi}{\partial d_m} = \frac{\partial \Pi_{int}}{\partial d_m} + \frac{\partial \Pi_{ext}}{\partial d_m} = K_m d - f_m = \underset{(1,N)}{K} \underset{(N,1)}{d} - f_m = 0 \tag{4}$$

We can use the addition theorem as the energy is a scalar, and the energy derivations. The *m-th* equation parts can be rewritten as follows.

$$\frac{\partial \Pi^{int}}{\partial d_m} = \frac{\partial \sum_{e=1}^{p} \Pi_e^{int}}{\partial d_m} = \sum_{e=1}^{p} \frac{\partial \Pi_e^{int}}{\partial d_m} = K_m d = \underset{(1,N)}{K} \underset{(N,1)}{d} \tag{5}$$

$$\frac{\partial \Pi^{ext}}{\partial d_m} = \frac{\partial \sum_{e=1}^{p} \Pi_e^{ext}}{\partial d_m} = \sum_{e=1}^{p} \frac{\partial \Pi_e^{ext}}{\partial d_m} = -f_m \tag{6}$$

The great advantage of this method lies in the fact, that there is no problem to combine elements of different dimensions. In one system, there can be beams, shells and 3D elements

combined. Each element is considered in the global stiffness matrix **K** by its contribution of the $\mathbf{K}_e$, and the vector of nodal forces **f** is composed of the elements contributions $\mathbf{f}_e$. The global stiffness matrix is assembled by merging the elements stiffness matrixes $\mathbf{K}_e$ into the global stiffness matrix according to the global code numbers, in other words, by the explicit position of the element contributions in the whole structure.

$$\frac{\partial \Pi}{\partial d} = \frac{\partial \Pi^{int}}{\partial d} + \frac{\partial \Pi^{ext}}{\partial d} = Kd - f = \underset{(N,N)}{K} \underset{(N,1)}{d} - \underset{(N,1)}{f} = 0 \tag{7}$$

This formula can be rewritten into the well-known form

$$Kd = f \tag{8}$$

or in the matrix notation

$$\underset{(N,N)}{K} \underset{(N,1)}{d} = \underset{(N,1)}{f} \tag{9}$$

3.1.2 Nonlinear Analysis

Since the material used for tensile structures is characterized by its load resistance practically only in tension, these structures have to change their shapes significantly to find the equilibrium positions. Such a shape change has a great influence on the stiffness $K(d)$ and the force $f(d)$ redistribution, and this fact has to be considered in the structural analysis. This behaviour is well known as a *geometric nonlinearity*. Since the material itself does not withstand the compression, the stress-strain diagram exhibits the nonlinear nature. This *Material nonlinearity* has to be considered as well. The formula mentioned above will obtain its dependency on the deformation.

$$K(d)d = f(d) \tag{10}$$

The stiffness matrix is composed of components as written in following formula,

$$K(d) = K_M(d) + K_\sigma(d) \tag{11}$$

where $K_M(d)$ is the constitutive stiffness matrix and $K_\sigma(d)$ is the geometric stiffness matrix. $K_M(d)$ depends on the constitutive low, i.e. the stress-strain diagram, and on the change of the spatial shape of the structure as the changes of the structural parts size and orientation leads to the changes of their spatial constitutive stiffness. For membrane and cable elements, $K_M(d)$ represents the in-plane stiffness (although it represents the general stiffness for a general element). $K_\sigma(d)$ can also be called the stress stiffness matrix, which is dependent on the stress state in the elements. For membrane and cable elements, $K_\sigma(d)$ represents the out-of-plane stiffness and it helps to make the tensile structures solvable, as they would tend to singularities without this term.

3.1.3 Geometric Nonlinearity

At the beginning of this part, it is necessary to define two essential configurations of the body. First, the reference configuration that represents the initial state of the structure, and second, the current configuration that represents the state of the structure after the deformation.
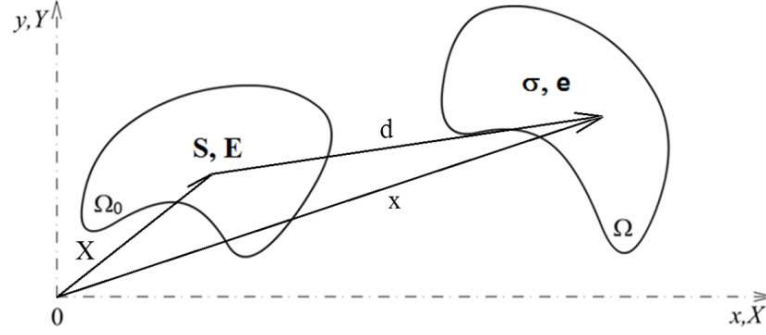
Fig. 78 – Reference (X,Ω₀) and the current (x,Ω) configuration of the body

The state of the body in the reference configuration Ω_0 is described by the *2ⁿᵈ Piola-Kirchhoff stress S* and the *Green-Lagrange strain E* while the state of the body in actual configuration is described by the *Cauchy stress σ* and the *Euler-Almansi strain e*, which are intuitive measures as they are actually the description of the state we observe in reality. These stresses and strains form the energetically conjugated couples, and we can describe the derivatives of the total potential energy as follows.

$$\frac{\partial \Pi}{\partial d} = \frac{\partial \Pi^{int}}{\partial d} + \frac{\partial \Pi^{ext}}{\partial d} = \int_{\Omega_0} S : \delta E \, d\Omega_0 - \int_{\Omega_0} q \cdot \delta d \, d\Omega_0 = \int_{\Omega} \sigma : \delta e \, d\Omega - \int_{\Omega} q \cdot \delta d \, d\Omega = 0 \quad (12)$$

When the structure is calculated, its physical description (the stiffness matrix K and the vector of forces f) is created on the initial (current) configuration. After the system of equations is solved, the structure takes a new (actual) configuration that can be described as $x = X + d$.

If the deformations d are small enough, the differences between those configurations can be neglected and we assume the initial and new configurations as the same. Thus, we do not recalculate the strains and stresses according to the new configuration but assume that $\sigma \approx S$ and $e \approx E$. This approximation is precise enough for the most of the engineering tasks and is well known as *the geometrically linear analysis*, *the small deformation analysis*, or *the first order analysis*.

However, the analysis described above cannot be sufficient for large deformations. The considerable differences between the initial and the new configurations (which can be described by deformation gradient $F = \partial x / \partial X$) require recalculation of the stress state in the structure according to the new geometry. The stress state in the actual configuration σ cannot be approximated by the stress state calculated in consideration of the initial configuration S anymore. Whenever the structure undergoes the deformation, a new stress/strain state is recalculated according to the new configuration, and a new stiffness matrix K and vector of nodal forces f is assembled. This new configuration of the first iteration becomes the initial configuration of the second iteration. After solving the second iteration, the new configuration for this iteration is obtained, which is the initial configuration of the third iteration. This process continues until the convergence criteria are reached. This process is well known as *the geometrically nonlinear analysis*, *the large deformation analysis*, or *the third order analysis*.

The large deformation analysis is performed by the sequence of linear steps/iterations, which approximate the nonlinear nature of the structure response $K(d)d = f(d)$. Both parts of the global stiffness matrix $K(d) = K_M(d) + K_\sigma(d)$ as well as the nodal force vector $f(d)$ are changing during the iterations. However, each step is considered as linear. This solving of the nonlinear equation system by the sequence of the linear equation system can be performed using many iterative methods., The Newton-Raphson method is the most common one.
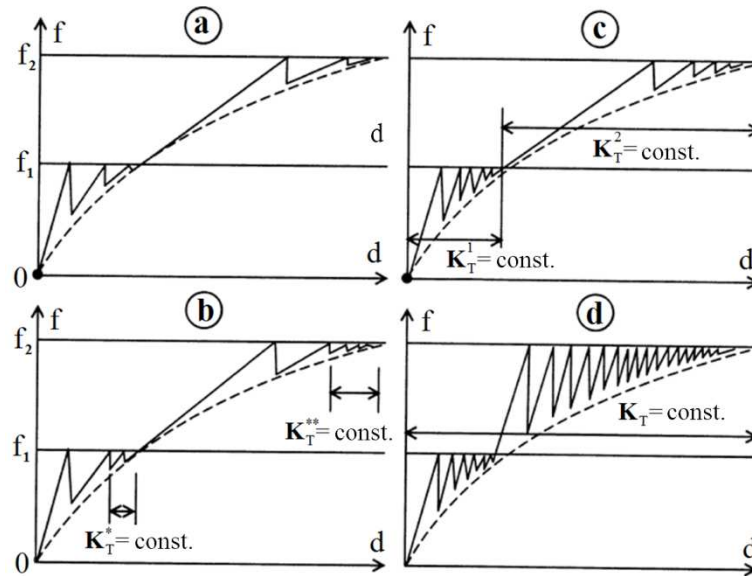
Fig. 79 – Diagram of the Newton-Raphson iterative method a) and its three modifications b),c),d)

3.1.4 Material Nonlinearity

As the material resistance of membrane or cable elements in the structure is considered to withstand only in tension, these structures are also subjected to significant material nonlinearity. The material behaviour in the tensile part of the stress-strain diagram can be approximated by the linear elastic, non-linear elastic, elastic-plastic or even general material response (*Fig. 80*).
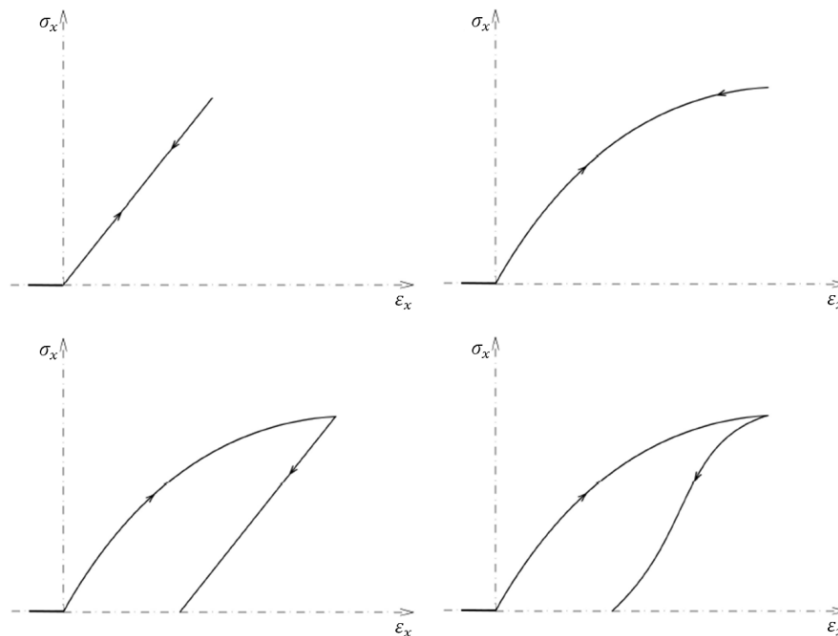
Fig. 80 – Elastic, non-linear elastic, elastic-plastic and general material models

Regardless the particular material model, the stress state of the membrane or cable element has to satisfy that only the tension occurs. For the membrane, the stress state of each element $(\sigma_x, \sigma_y, \tau_{xy})$ has to be transformed into the main directions (σ_1, σ_2) to eliminate the possible occurrence of the compression. This transformation can be performed by the Mohr circle analogy, or by the eigenvalue problem.
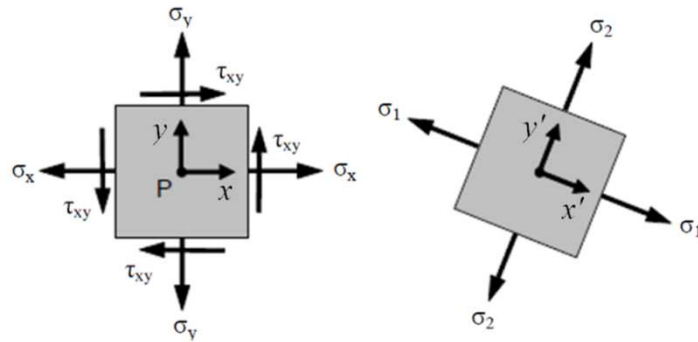
Fig. 81 – Stress state: stresses in the planar axis direction, main stresses in the main directions ([19] with modifications)
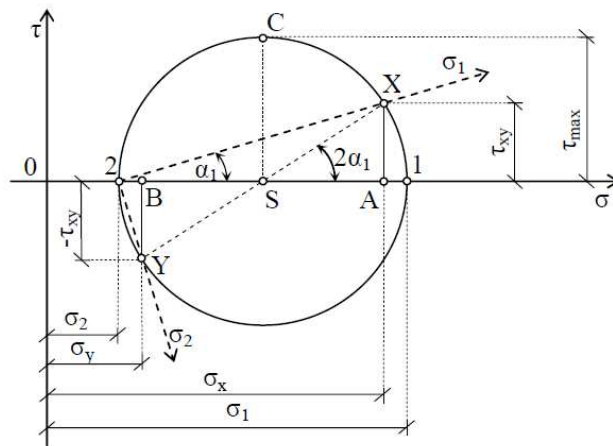
Fig. 82 – Mohr circle

$$\sigma_{1,2} = \frac{(\sigma_x + \sigma_y)}{2} \pm \sqrt{\left(\frac{(\sigma_x - \sigma_y)}{2}\right)^2 + \tau_{xy}^2} \tag{13}$$

$$det(\sigma - \sigma_0 I) = 0 \tag{14}$$

The material nonlinearity influences the global stiffness matrix $K(d)$, which is therefore nonlinear as well. The influence on the material part of the global stiffness matrix $K_M(d)$ is direct while the influence on the geometric part $K_\sigma(d)$ is indirect. However, the nonlinear material response has nonlinear influence on the stress state, which affects this geometric part of the global stiffness matrix (if the geometric nonlinearity is considered in the analysis).

3.2 Practice

This part of the *Structural Analysis* chapter will be focused on practical demonstrations of the calculation of mechanically prestressed membrane structures as well as the calculation of pneumatic structures.

3.2.1 Analysis of Membrane Structure

The first structure to be presented has a hypar shape. The horizontal distance between the low points as well as between the high points is $10.0\ m$. The material used for the membrane is the woven fabric, whose mechanical properties are approximated by the orthotropic linear elastic material model with consequent characteristics.

$$E_x = 1000.0\frac{kN}{m}, E_y = 800.0\frac{kN}{m}, G_{xy} = 100.0\frac{kN}{m}, \nu_{xy} = 0.10, \nu_{yx} = 0.08 \tag{15}$$

The constitutive matrix of this material is:

$$C = \begin{bmatrix} C_{11} & C_{12} & C_{13} \\ & C_{22} & C_{23} \\ sym. & & C_{33} \end{bmatrix} = \begin{bmatrix} C_{xxxx} & C_{xxyy} & C_{xxxy} \\ & C_{yyyy} & C_{yyxy} \\ sym. & & C_{xyxy} \end{bmatrix} = \begin{bmatrix} 1008.06 & 80.65 & 0.00 \\ & 806.45 & 0.00 \\ sym. & & 100.00 \end{bmatrix} \frac{kN}{m}$$

(16)

The high points of the membrane structure are supported by the columns fixed by cables, and the low pints are supported by single cables as displayed below (*Fig. 83*). The triangle FE were used for the membrane since they are not as susceptible to deplanation as quadrangles.
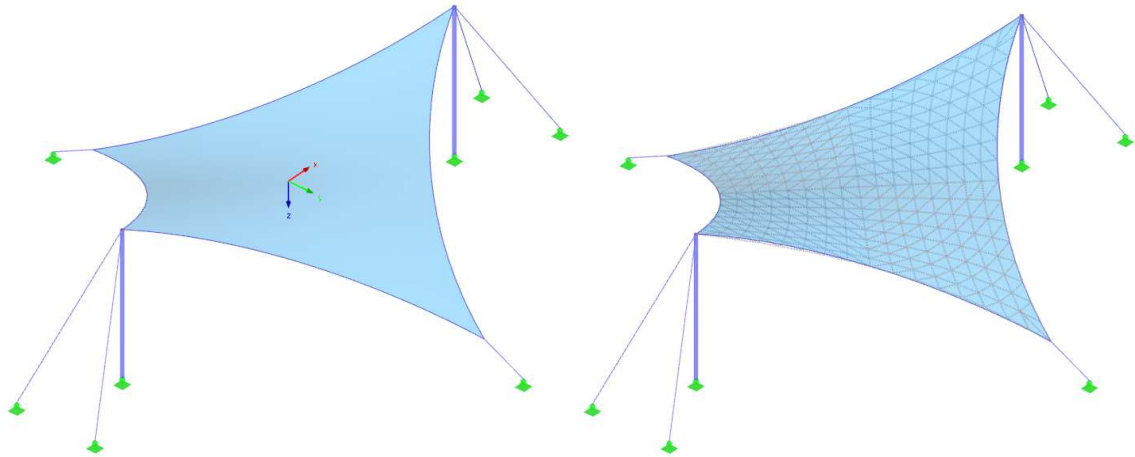
Fig. 83 – Hypar membrane structure with the x/y (warp/weft) orientation displayed, FE mesh

The form-finding results are used as an initial equilibrium state for the further analysis. The isotropic prestress $1.00\ kN/m$ is used for the membrane, $10.00\ kN$ is used as a prestress of the boundary cables (*Fig. 84*).
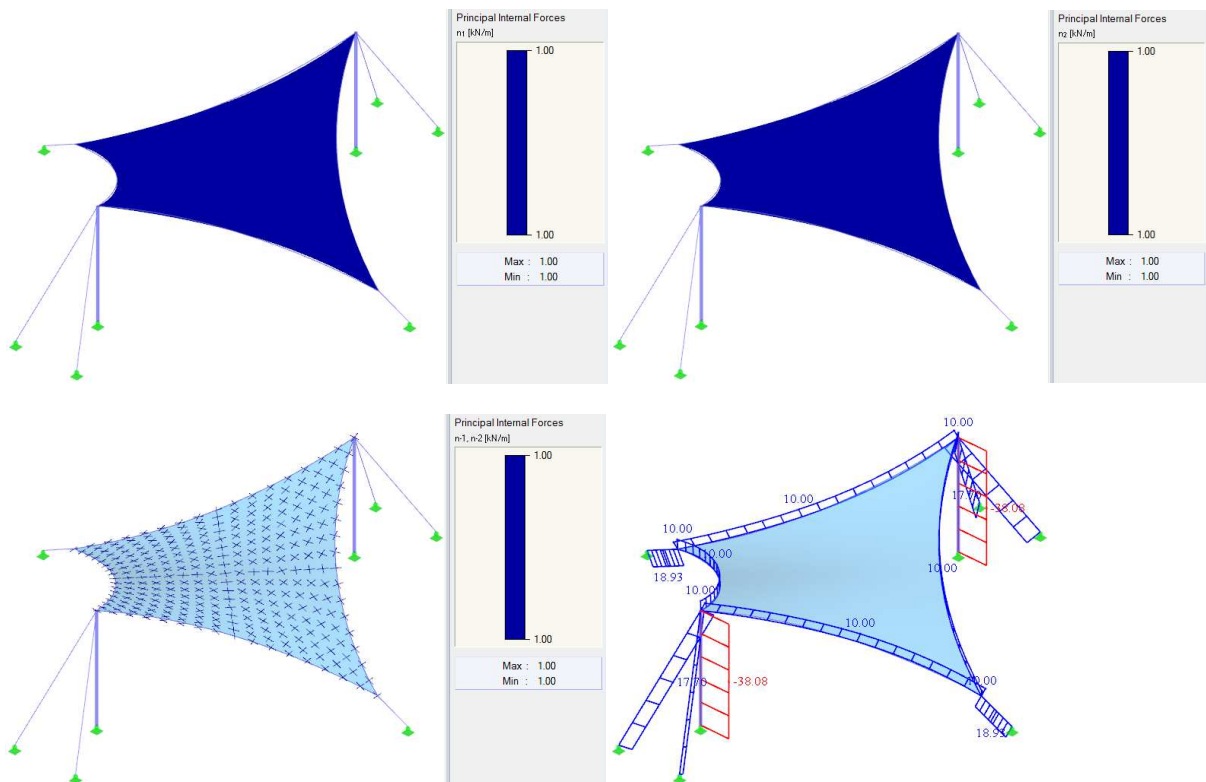
Fig. 84 – The membrane prestress as the result of form-finding

For the structure, eight load cases are considered: self-weight, four different wind loads, and three different snow loads (*Fig. 88 - Fig. 91*). For the wind load, the maximal dynamic pressure is $q_p(z) = 0.61 \, kN/m$, and C_p values are used according to *Appendix A1* of *European Design Guide* [35] (*Fig. 86, Fig. 87*). The characteristic value of the snow load is $s_k = 0.80 \, kN/m$.
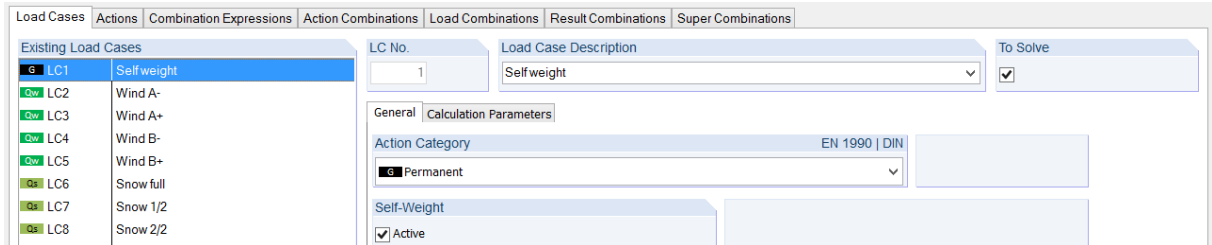
Fig. 85 – *Definition of load cases*
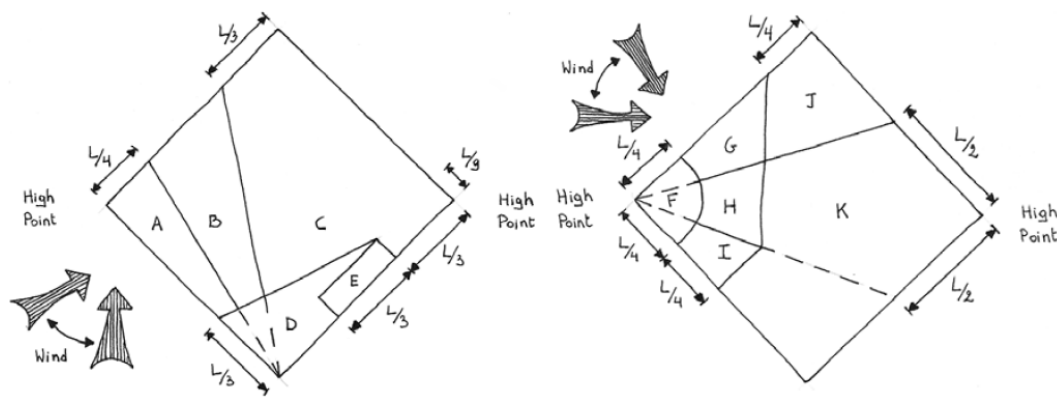
Fig. 86 – C_p *zones definition on the hypar structure [35]*

External C_p Values	Zones										
	A	B	C	D	E	F	G	H	I	J	K
positive	+0	+0	+0.3	+0.3	+0.3	+0	+0	+0.2	+0	+0	+0.2
negative	-1.45	-0.9	-0.65	-0.70	-1.20	-1.80	-1.20	-0.90	-1.20	-0.65	-0.65

Fig. 87 – *External C_p values for the hypar structure [35]*
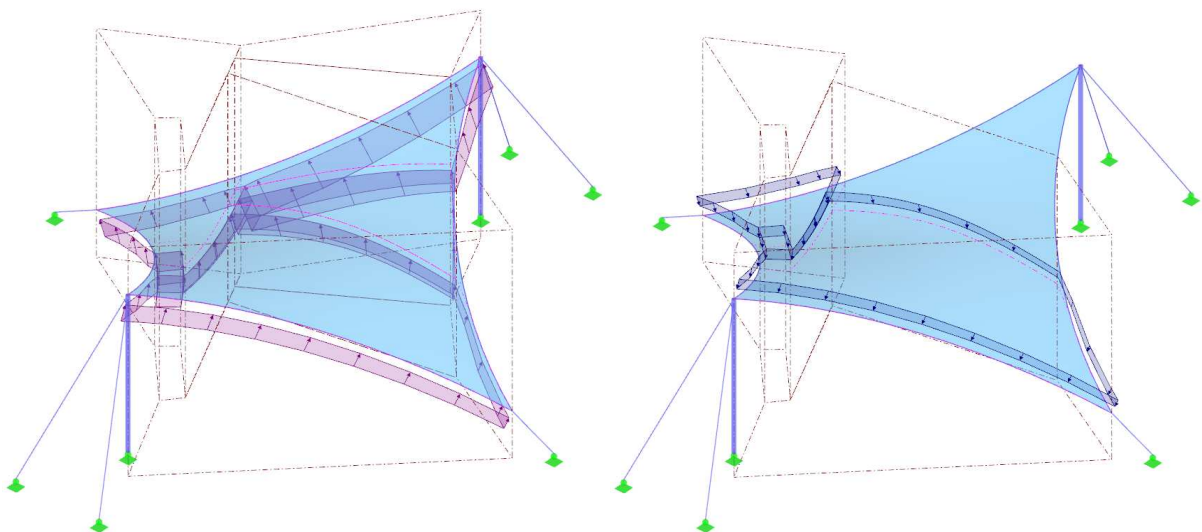
Fig. 88 – *Load cases LC2 (Wind A-) and LC3 (Wind A+)*
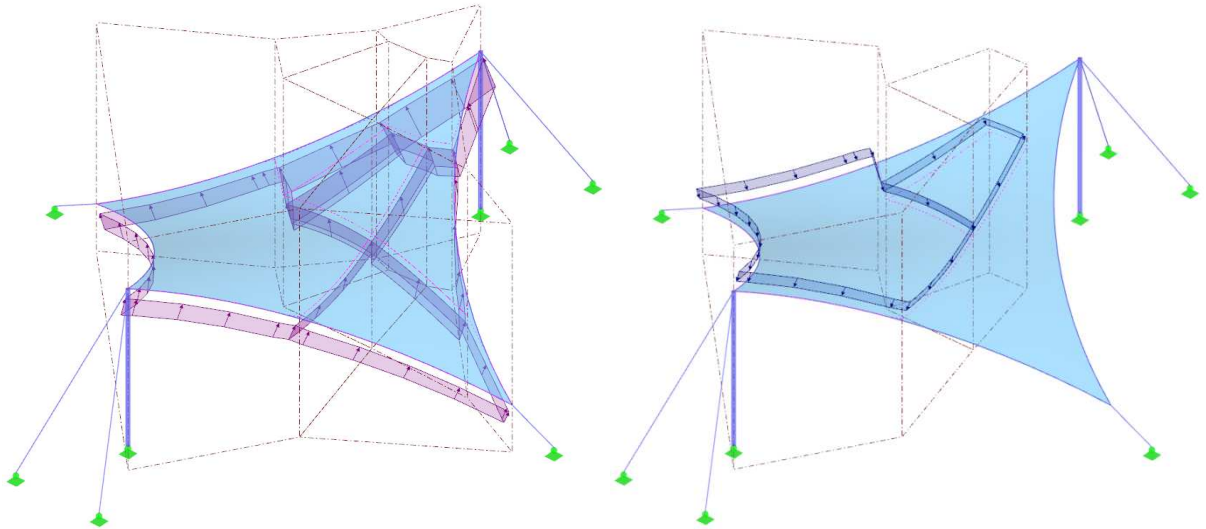
Fig. 89 – Load cases LC4 (Wind B-) and LC5 (Wind B+)
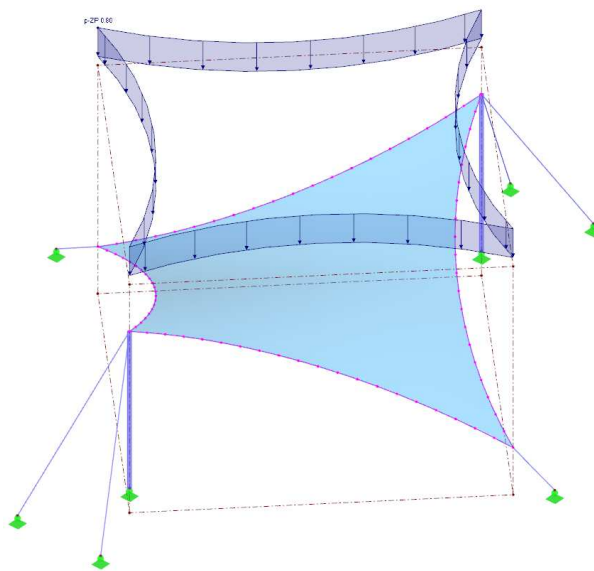
Fig. 90 – Load case LC6 (Snow full)
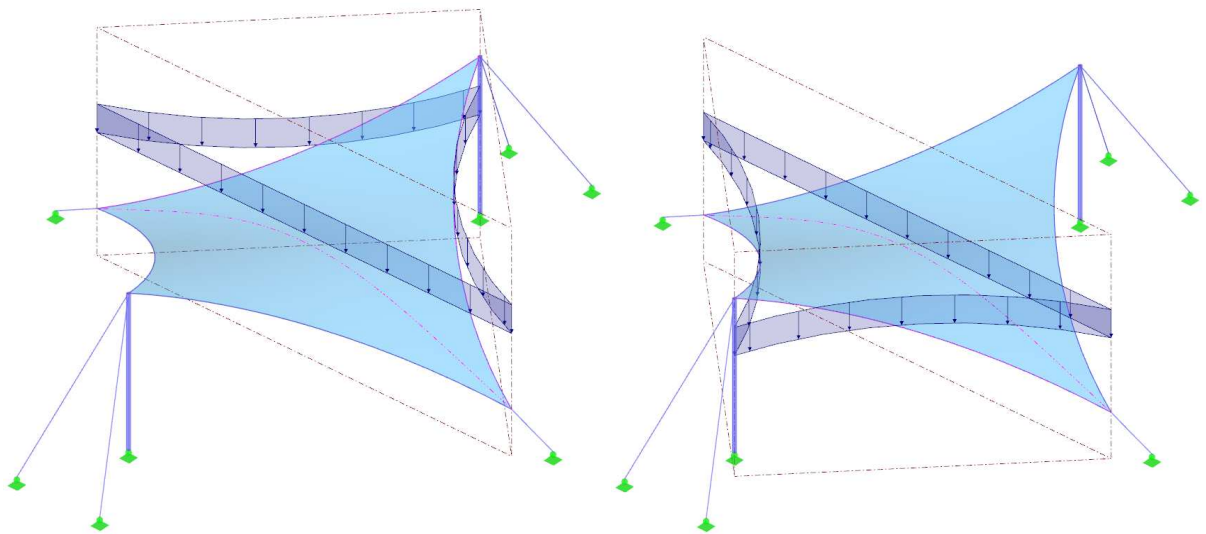
Fig. 91 – Load cases LC7 (Snow 1/2) and LC8 (Snow 2/2)

The loads described above belong to three different *Actions* (*Fig. 92*). For the consequent structural analysis, the combination expressions for *Ultimate Limit State (ULS)* and *Servicability Limit State (SLS)* are used (*Fig. 93*). The combinations of *Action types* (*Fig. 94*) as well as the final *Load combinations* (*Fig. 95*) are generated automatically. For this structure, there are 32 ULS combinations and 32 SLS combinations to be calculated.
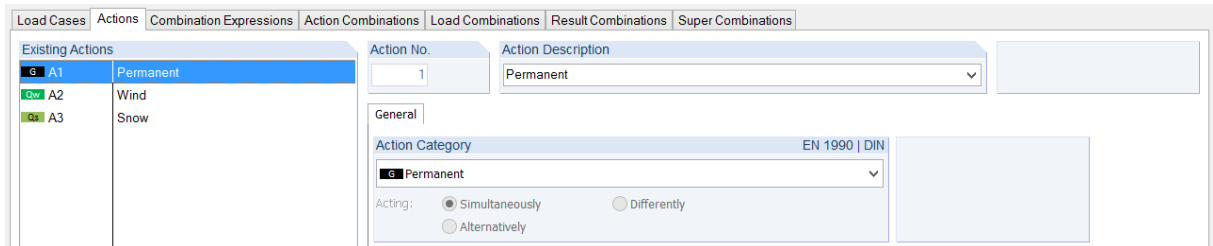
Fig. 92 – Actions (types of loads)
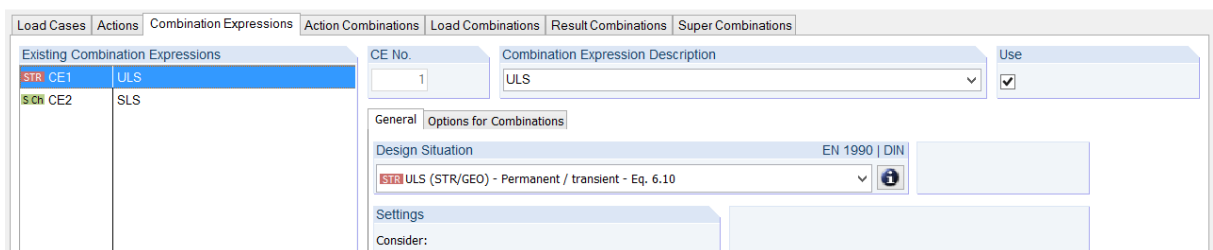
Fig. 93 – Combination Expressions (ULS and SLS)
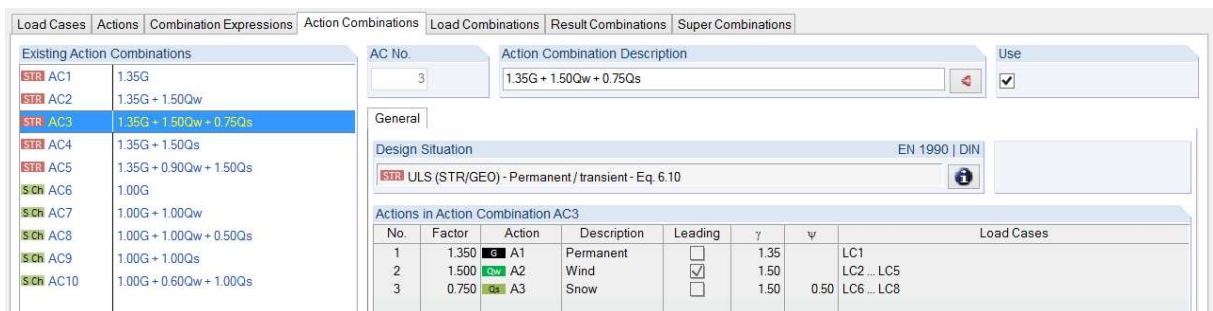
Fig. 94 – Action types combinations (ULS and SLS)
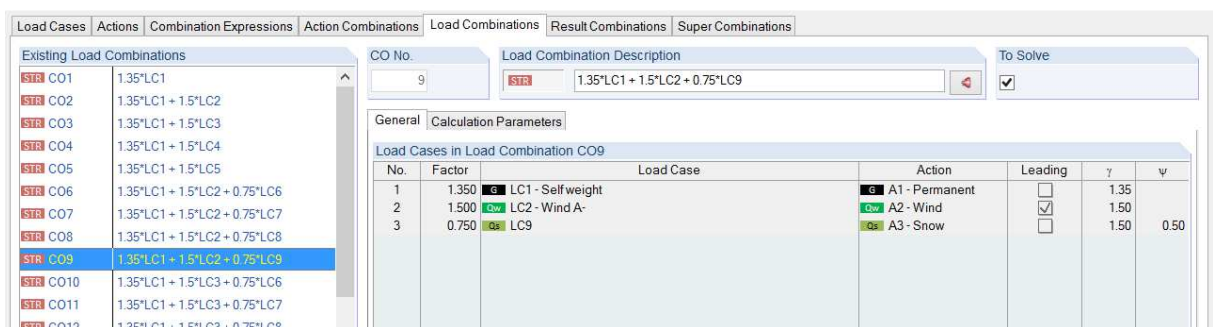
Fig. 95 – Load combinations (ULS and SLS)

If the following, the results of the combination CO18 with the maximal snow load $(1.35 \cdot LC1 + 1.50 \cdot LC6)$ will be presented as an example (*Fig. 96 - Fig. 101*). The envelope of the results of all ULS combinations will be presented as well (*Fig. 102 - Fig. 107*). First, the deformation will be presented, then the internal forces, and finally the contour lines and slopes of the membrane surface after the deformation, as an information for estimation of ponding occurrence.
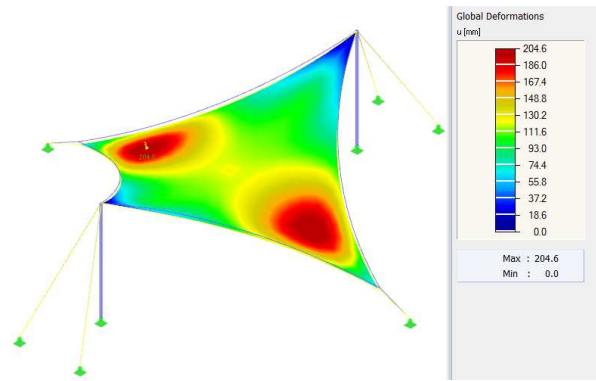
Fig. 96 – Global deformations u (CO18)
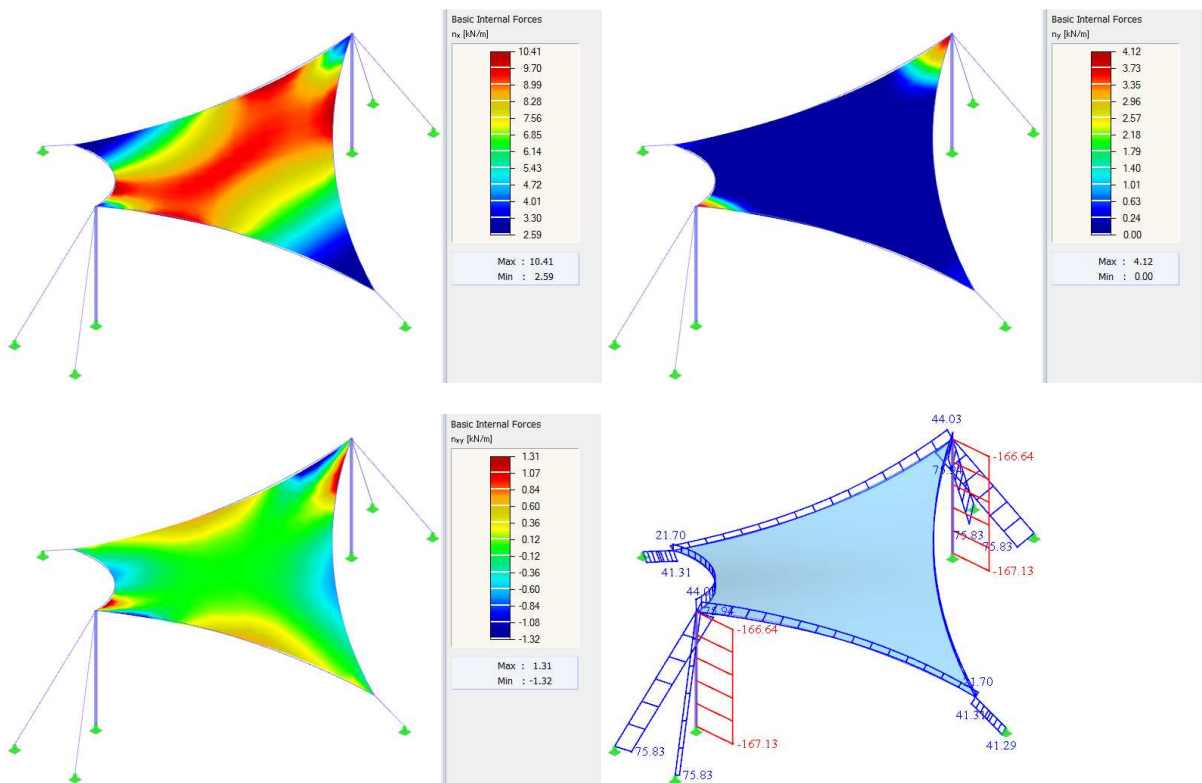
Fig. 97 – Basic internal forces n_x, n_y, n_{xy} in the membrane, normal force N in cables and beams (CO18)
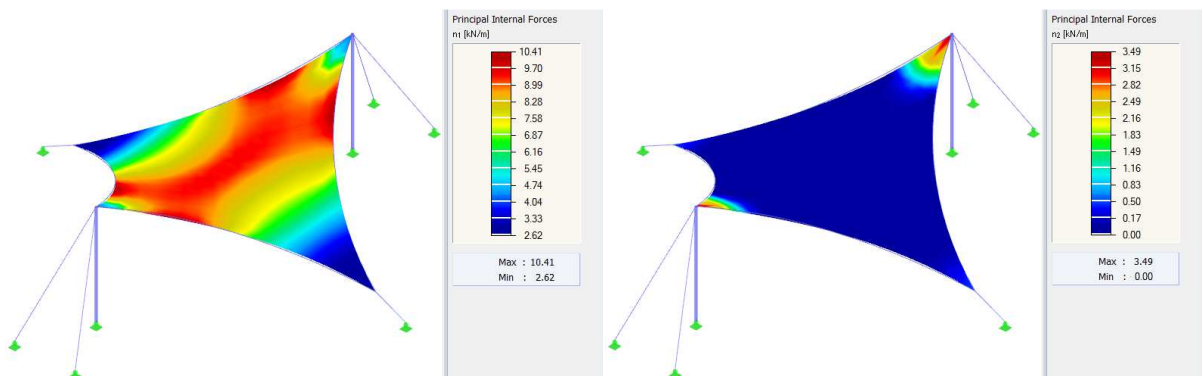
Fig. 98 – Main internal forces n_1, n_2 (CO18)
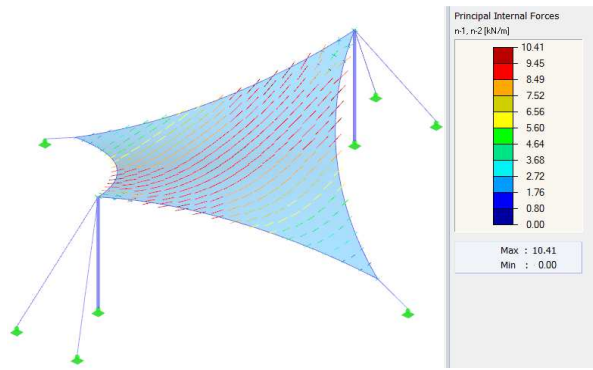
Fig. 99 – Vectors of main internal forces n_1, n_2 (CO18)
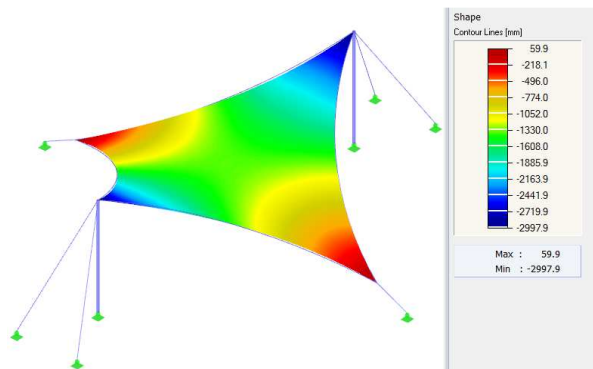
Fig. 100 – Contour lines on the surface after deformation (CO18)
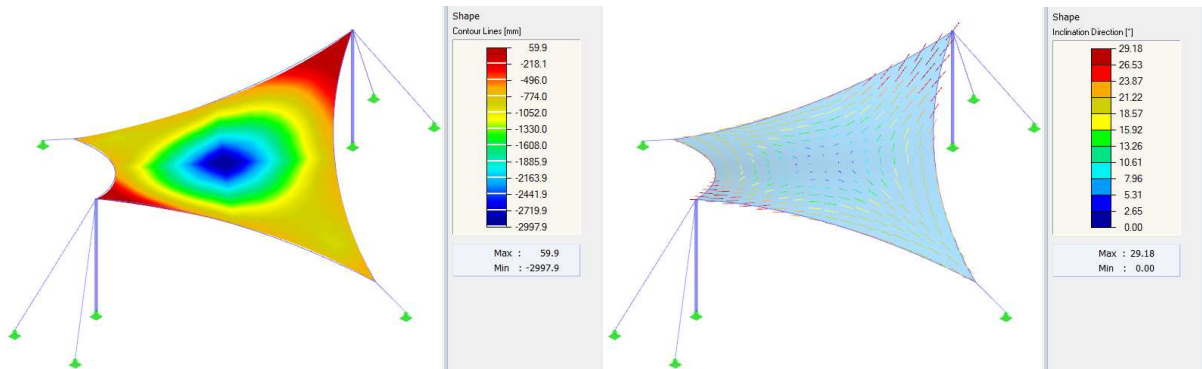
Fig. 101 – Slopes of the surface after deformation (CO18)

The envelope of the results of all ULS considers the critical value in each position on the membrane, therefore the displayed values are not as smooth as the results of the particular load cases in general (*Fig. 104, Fig. 105*).
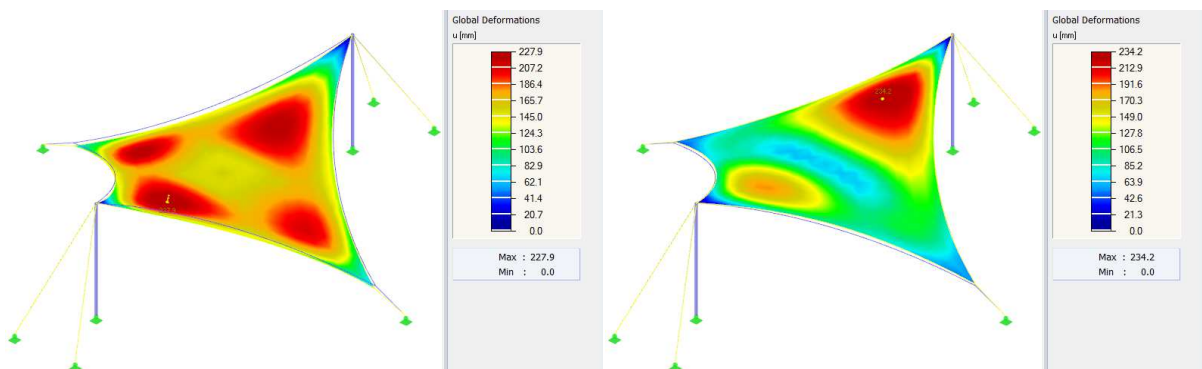
Fig. 102 – The envelope of the maximal positive and negative deformations u (ULS)
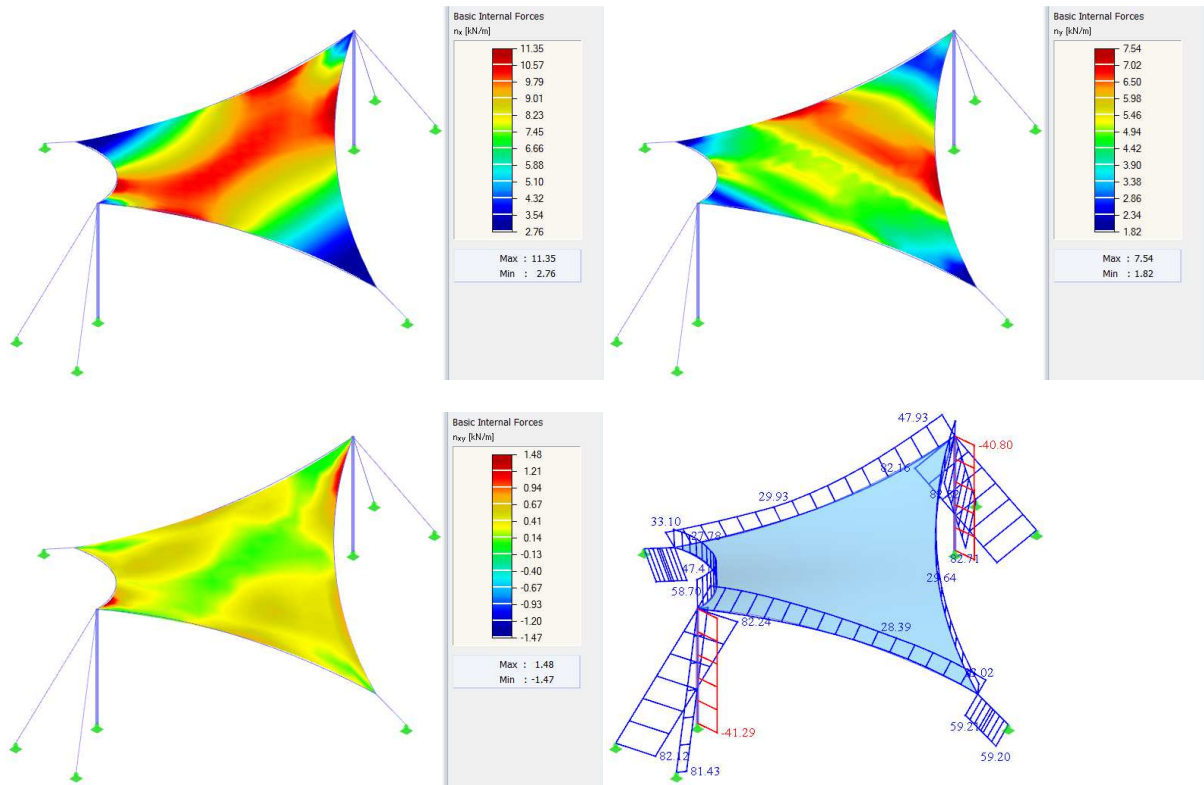
Fig. 103 – The envelope of the basic internal forces n_x, n_y, n_{xy} in the membrane, the envelope of the normal forces N in cables and beams (ULS)
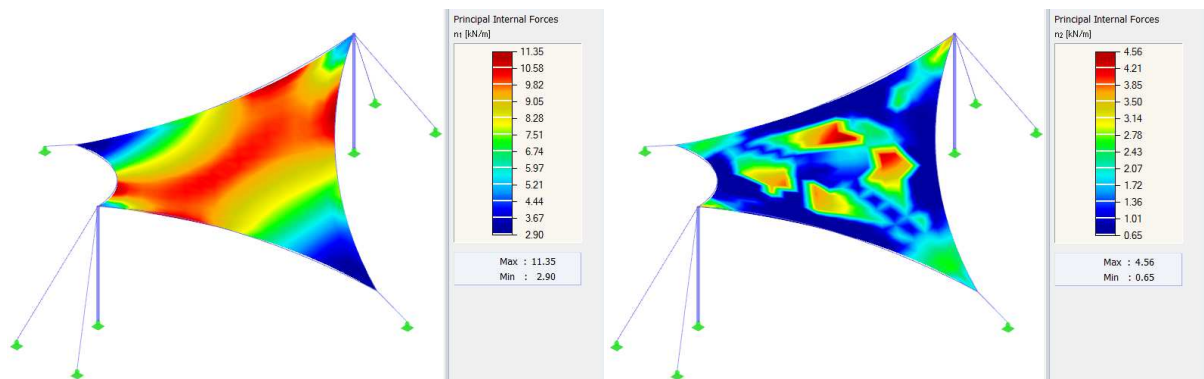
Fig. 104 – The envelope of the main internal forces n_1, n_2 (ULS)
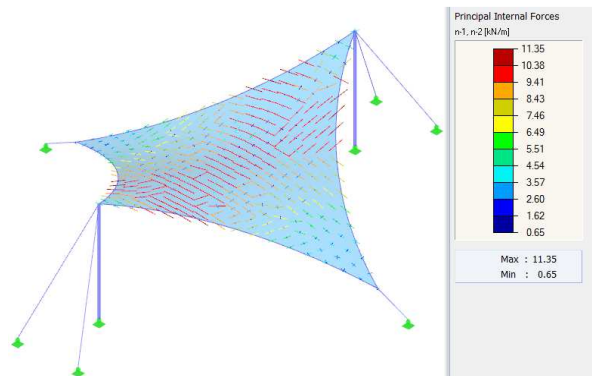
Fig. 105 – The envelope of the vectors of the main internal forces n_1, n_2 (ULS)
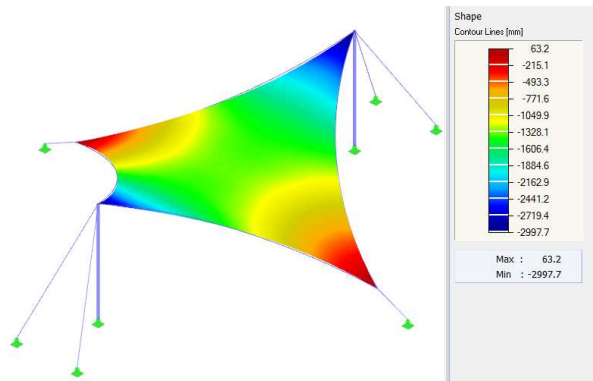
Fig. 106 – The envelope of the contour lines on the surface after the deformation (ULS)
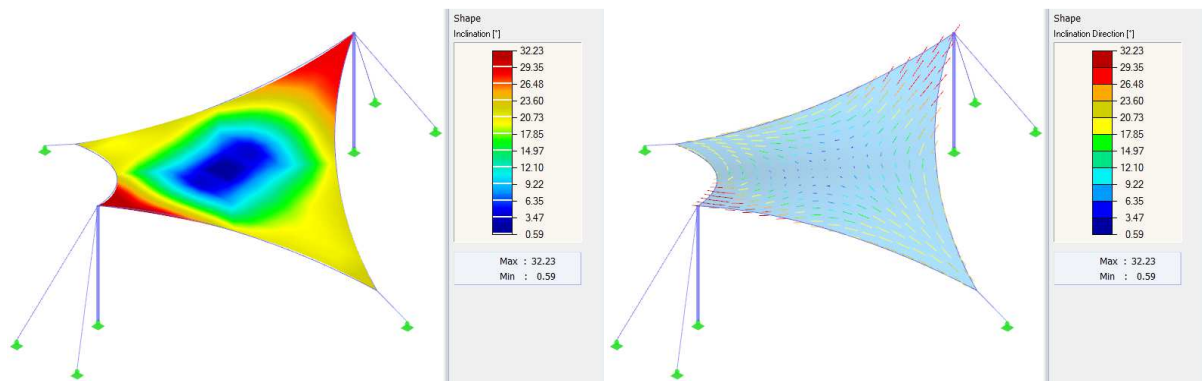
Fig. 107 – The envelope of the maximal slopes of the surface after the deformation (ULS)

3.2.2 Warp/Weft Orientation

The structure presented above will be further analysed with respect to the influence of the warp/weft orientation setting. The same geometry, construction elements and materials are used. The only difference between these two examples is the change of the axis (fibre) orientation (*Fig. 108*). The nonlinear analysis will be performed for the load combination CO18.
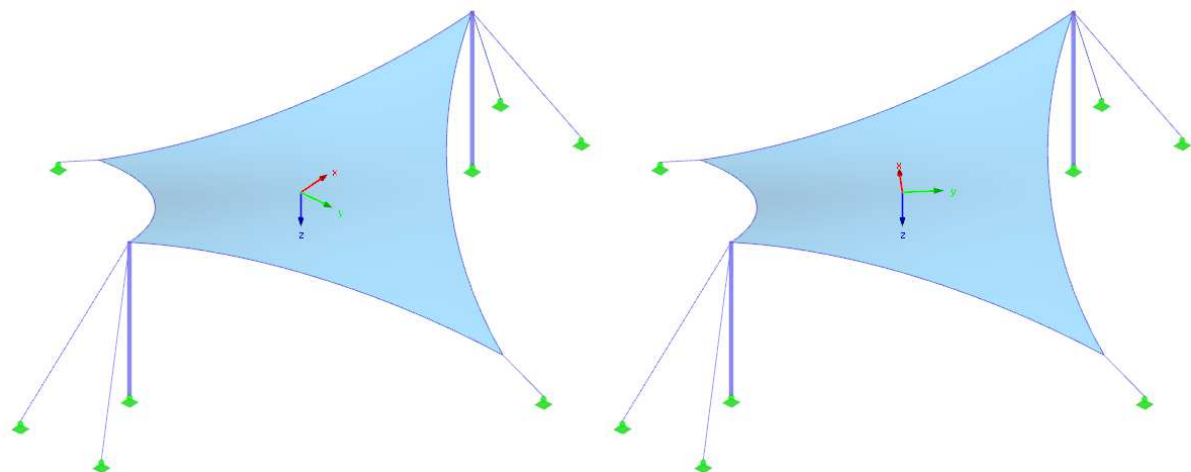
Fig. 108 – Axes (fibres) orientation of Model 1 and Model 2
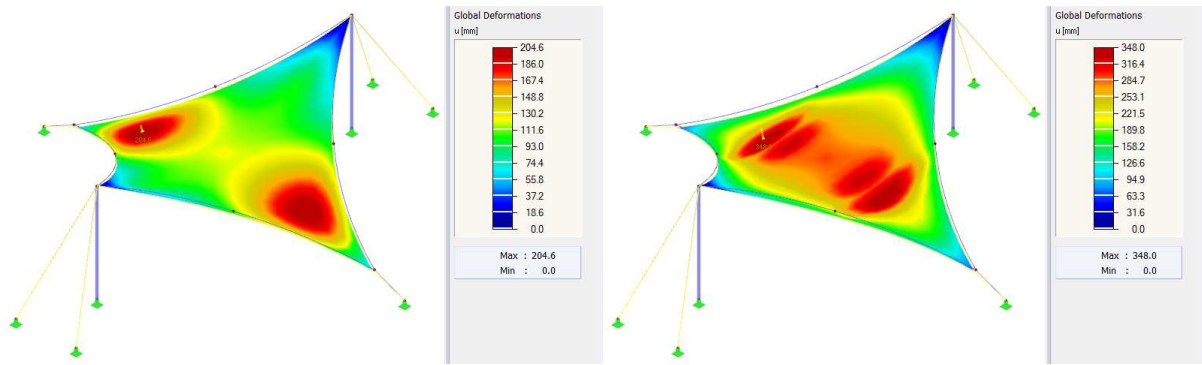
Fig. 109 – Global deformations u of Model 1 and Model 2 (CO18)
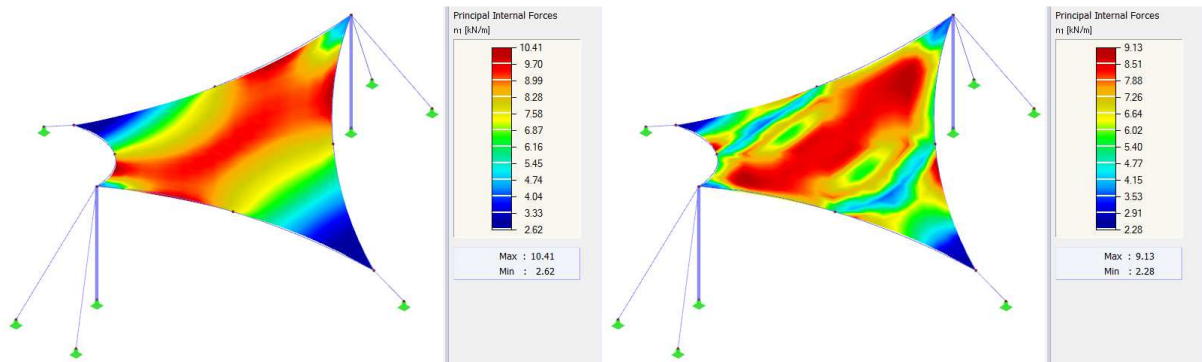
Fig. 110 – Main internal forces n_1 of Model 1 and Model 2 (CO18)
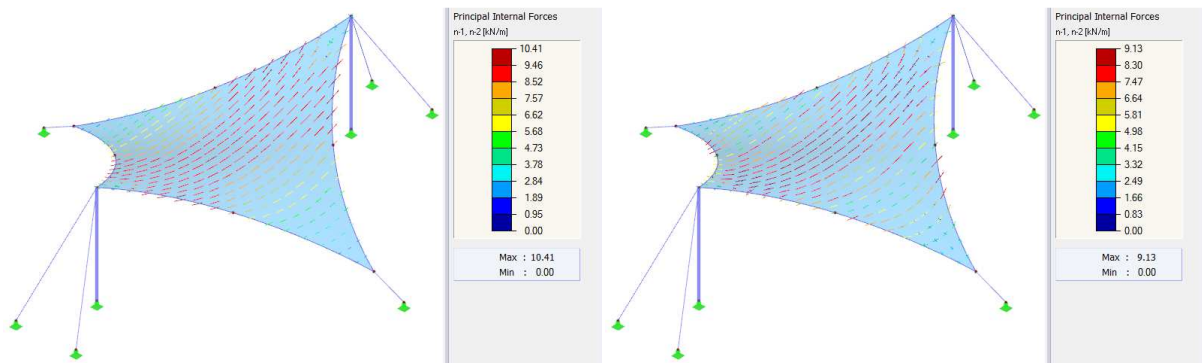
Fig. 111 – Vectors of main internal forces n_1, n_2 of Model 1 and Model 2 (CO18)
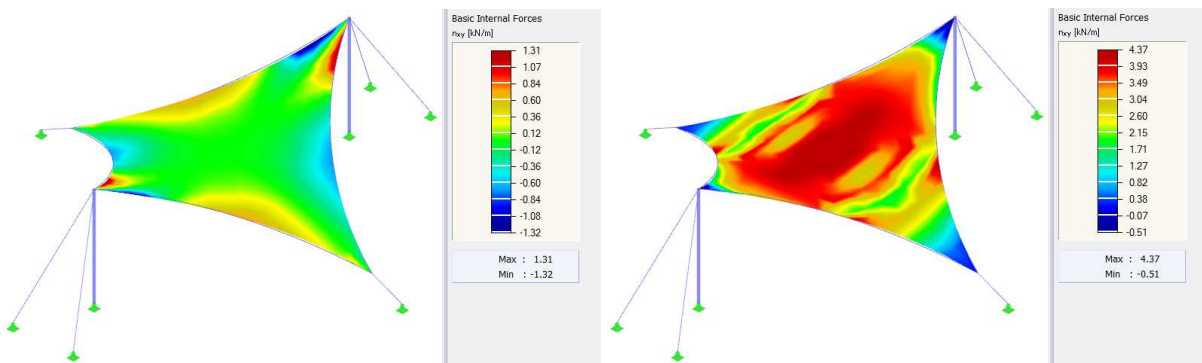
Fig. 112 – Shear forces n_{xy} of Model 1 and Model 2 (CO18)
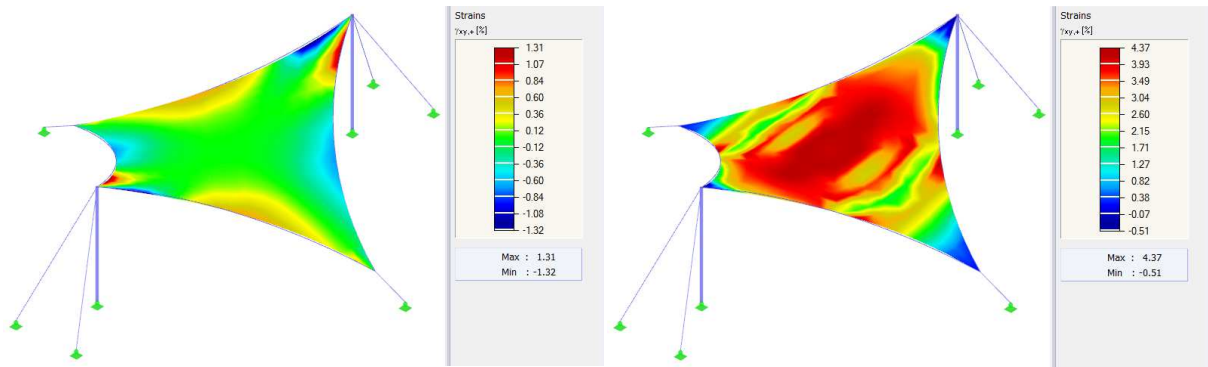
Fig. 113 – Shear deformations γ_{xy} of Model 1 and Model 2 (CO18)

The orthotropy orientation has a considerable influence on the structural behaviour. The maximal deformation of *Model 1* is $u_{max,M1} = 204.6\ mm$, and the maximal deformation of *Model 2* is $u_{max,M2} = 348.0\ mm$. Even though the maximal principal forces of *Model 2* ($n_{1,M2} = 9.13\ kN/m$) are of lower value than the maximal principal forces of *Model 1* ($n_{1,M1} = 10.41\ kN/m$), the disadvantage of the *Model 2* axis orientation can be seen in comparison with the shear forces/deformations, where the force values are $n_{xy,M1} = 1.31\ kN/m$ and $n_{xy,M2} = 4.37\ kN/m$, and the shear deformation values are $\gamma_{xy,M1} = 1.31\ \%$ and $\gamma_{xy,M1} = 4.37\ \%$. Such a great shear deformation may cause undesirable wrinkles.

3.2.3 Pneumatic Structures

The following picture shows the selection of the pneumatic structures according to the air management as they can be with or without air supply (*Fig. 114*). Different numbers of layers/chambers are also an option to be designed by an engineer (*Fig. 114, Fig. 115*).
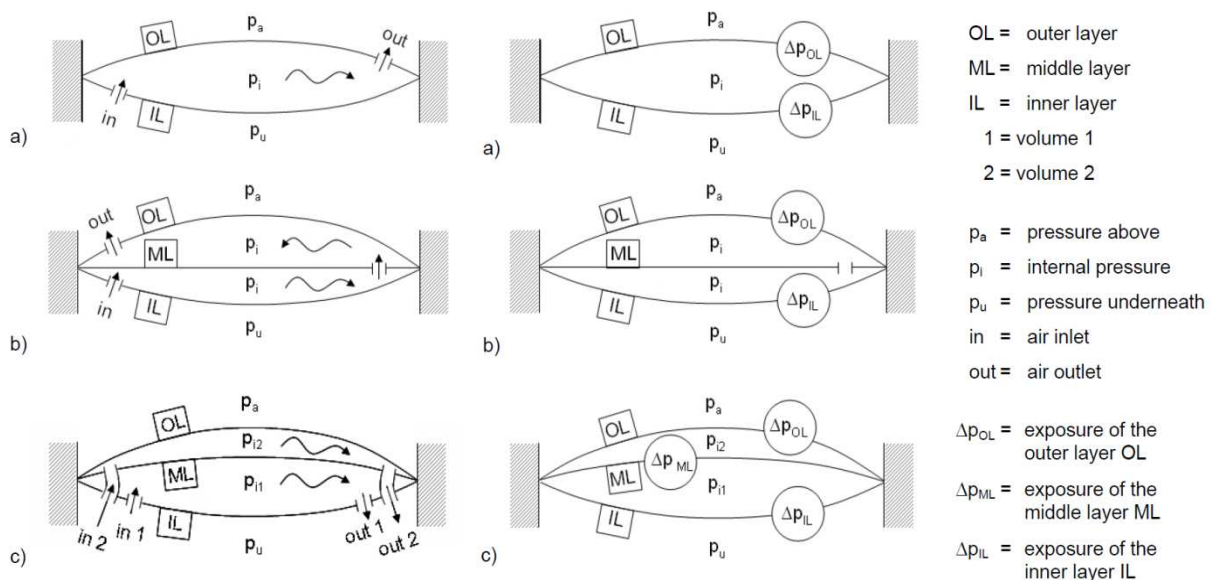
Fig. 114 – Air management of pneumatic stabilized and prestressed cushions (on the left) and air behaviour of enclosed cushions (on the right): a) 2-layer system, b) 3-layer system, flat middle layer (mechanically prestressed) and c) 3-layer system, curved middle layer (pneumatically prestressed) [21]

In the structural analysis, it is possible to consider different gas modes, which simulate the desired structural response during the loading process. Generally, there are two basic types of gas behaviour. The first one is the gas low.

$$\frac{p \cdot V}{T} = kons. \tag{17}$$

This assumption is appropriate for enclosed cushions or for fast processes acting on air supplied structures, if the compressor is not able to quickly change the amount of the air inside the cushion. The gas low is usually considered as an isothermal process.

$$p \cdot V = kons. \tag{18}$$

The change of the temperature that has an influence on enclosed cushions during the seasons can be considered in the calculation by using the temperature load.

The second general option is the simulation of the air supply/compressor. In this case, you can consider different requirements, such as *resulting overpressure*, *overpressure increment*, *resulting volume,* or *volume increment*.

1. **1-layer system** (one chamber with a rigid base)

2. **2-layer system** (one chamber)

3. **3-layer system** (two chambers, flat middle layer)

4. **3-layer system** (two chambers, curved middle layer)

5. **3-layer system** (two chambers, flat middle layer, layer separation at the boundary)

6. **3-layer system** (two chambers, curved middle layer, layer separation at the boundary)
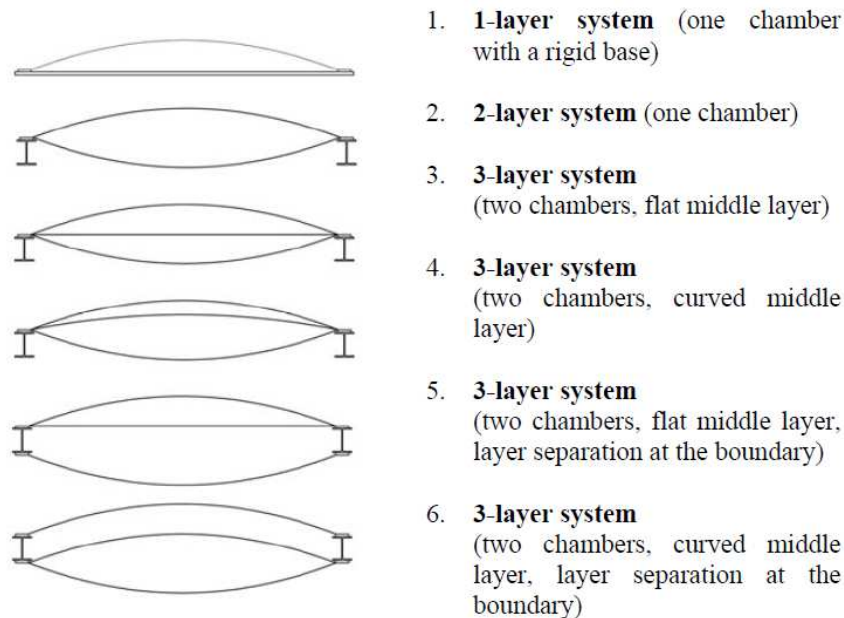
Fig. 115 – Common formation of ETFE layers in a foil cushions [23]

The collapse of the cushion can occur (*Fig. 116*). This situation can be simulated by the options described above when the resulting overpressure or the resulting volume is set to zero.
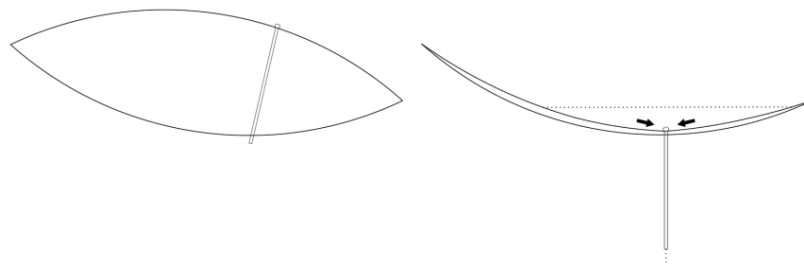
Fig. 116 – The function of the cushion drainage: a) cushion with regular internal pressure, b) breakdown of the operating system, the collected water is emptied through the drainage pipe [23]

Note: The software tool for calculating the behaviour described above is currently in the development process, and will be included in the RFEM software in the near future. Below, the analysis of a pneumatic structure performed in this tool is presented.

3.2.4 Analysis of Pneumatic Structure

The second structure to be presented is a greenhouse made as a pneumatic structure. The inflated cushions consist of two ETFE layers with a thickness $t = 300.0\ \mu m$ (light-blue parts in *Fig. 117, Fig. 118*). The linear isotropic material model is considered for this material, where consequent characteristics are used.

$$E = 900.0\ MPa, G = 310.0\ MPa, \nu = 0.452 \qquad (19)$$

The constitutive matrix of this material is:

$$C = \begin{bmatrix} C_{11} & C_{12} & C_{13} \\ & C_{22} & C_{23} \\ sym. & & C_{33} \end{bmatrix} = \begin{bmatrix} C_{xxxx} & C_{xxyy} & C_{xxxy} \\ & C_{yyyy} & C_{yyxy} \\ sym. & & C_{xyxy} \end{bmatrix} = \begin{bmatrix} 339.18 & 153.18 & 0.00 \\ & 339.18 & 0.00 \\ sym. & & 93.00 \end{bmatrix} \frac{kN}{m} \quad (20)$$

The cushions are supported by steel arches (steel S355, *Fig. 117, Fig. 118*). The composition of the steel and the foil is completed by wooden parts (glulam timber GL 28h; brown parts in *Fig. 117, Fig. 118*). The length of the structure is $l \approx 35\ m$, the width and high are $w \approx h \approx 10\ m$.

The form-finding was performed with the isotropic prestress $n_x = n_y = 1.00\ kN/m$ of the ETFE foil layers and the internal overpressure $p_o = 250.0\ Pa$ of the gas in chambers. The resulting shape is the initial equilibrium state for the nonlinear structural analysis.
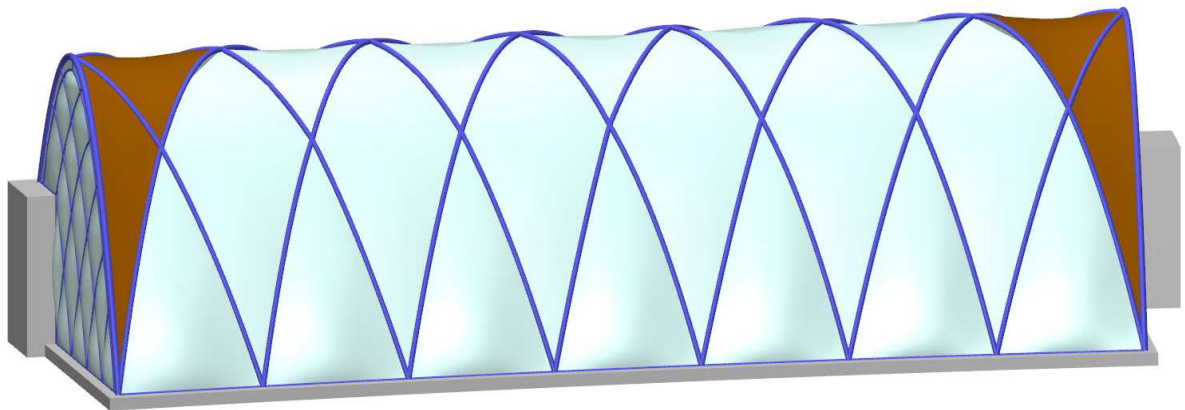
Fig. 117 – Geometry of the greenhouse structure
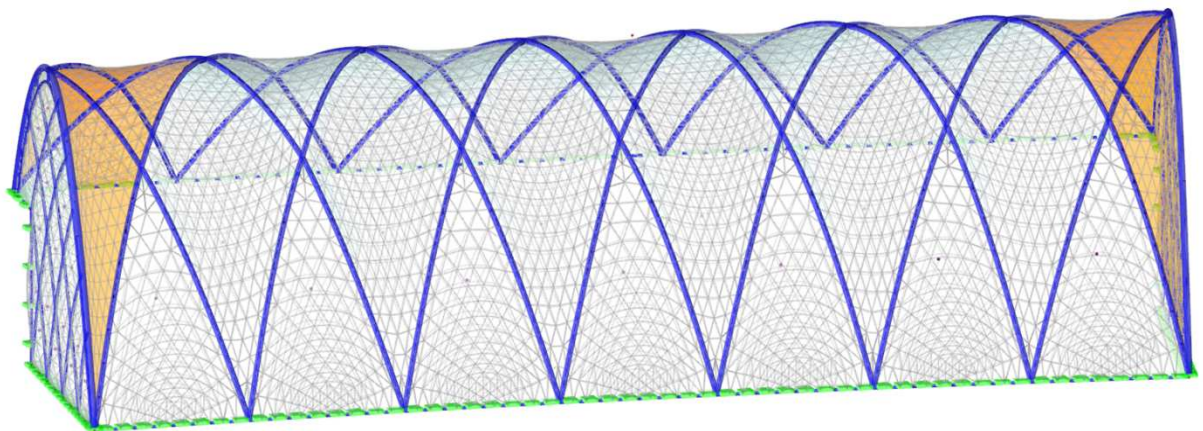
Fig. 118 – The FE model of the greenhouse structure (1221 1D elements, 16508 2D elements, 20172 3D elements)

The form-finding was performed for the *resulting overpressure* requirement with the value described above. The structural analysis applies different combinations with different gas behaviour requirements. As an example, the analysis of the structure subjected to the load combination $CO2$ ($CO2 = 1.35 \cdot LC1 + 1.50 \cdot LC5$, where $LC1$ is the self-weight and $LC5$ is the wind load) is presented, considering the isothermal gas low. For estimation of the wind load, the following C_p values redistribution is used (*Fig. 119*). The load of $CO2$ is presented below (*Fig. 120, Fig. 121*).
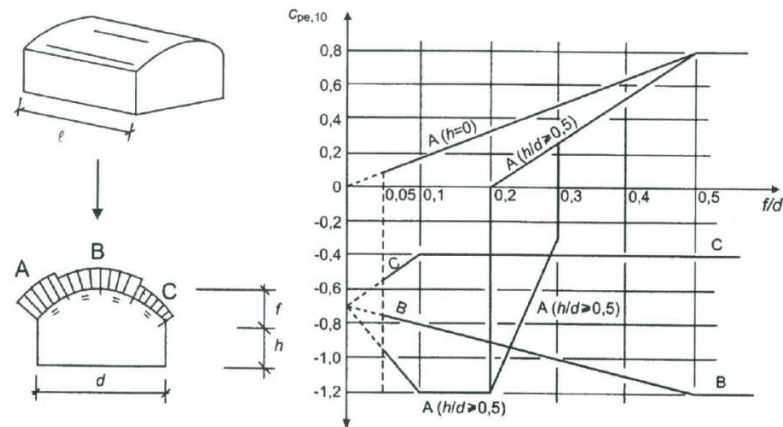
Fig. 119 – Recommended values of the external pressure coefficients C_p for vault roofs with the rectangular ground plan (EN 1991-1-4)
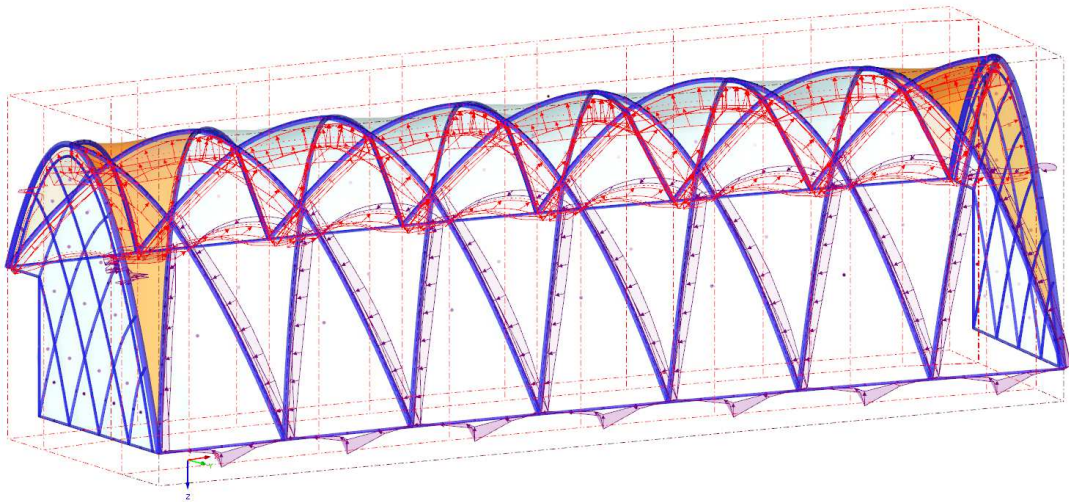
Fig. 120 – Load combination $CO2 = 1.35 \cdot LC1 + 1.50 \cdot LC5$
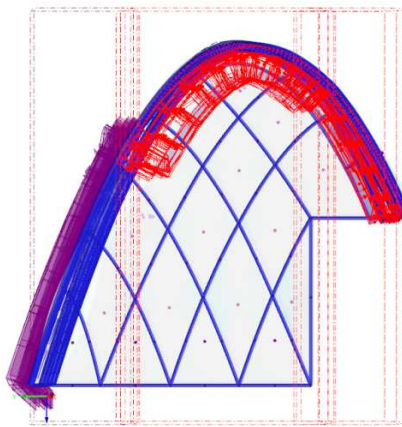
Fig. 121 – Load combination $CO2 = 1.35 \cdot LC1 + 1.50 \cdot LC5$

In particular, results of the nonlinear structural analysis are presented. First, the global deformations (*Fig. 122*) and second, the resulting pressure (*Fig. 123*). It is important to note that this pressure is the absolute pressure, not an overpressure. The atmospheric (outside) pressure was considered as $p_a = 100\,000.0 Pa$. Most of the cushions are subjected to the overpressure after the analysis; however, the dark-blue parts are subjected to the inside pressure that is lower than the outside pressure. The reason for this unusual behaviour is that the lower layer is double-curved and therefore, it does not move upwards without accumulating internal forces. This situation may occur when the wind lifts up the outer layer and the lower layer does not significantly deform (*Fig. 123*).
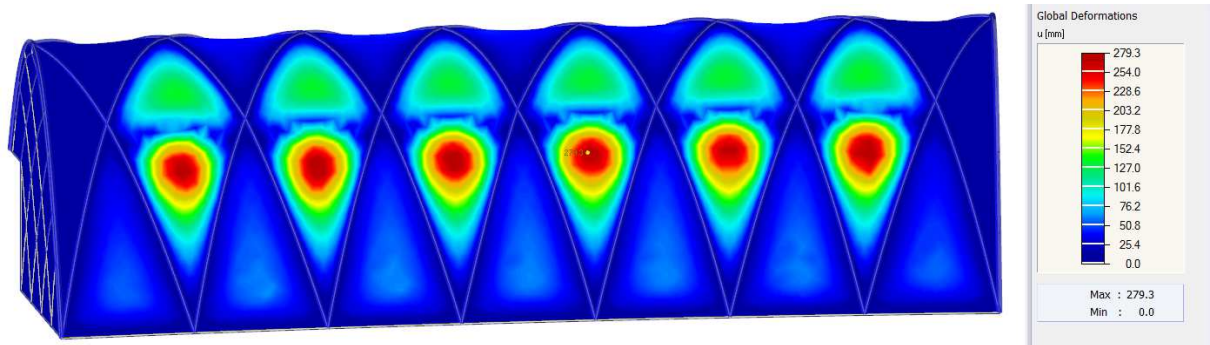
Fig. 122 – Global deformations u (CO2)
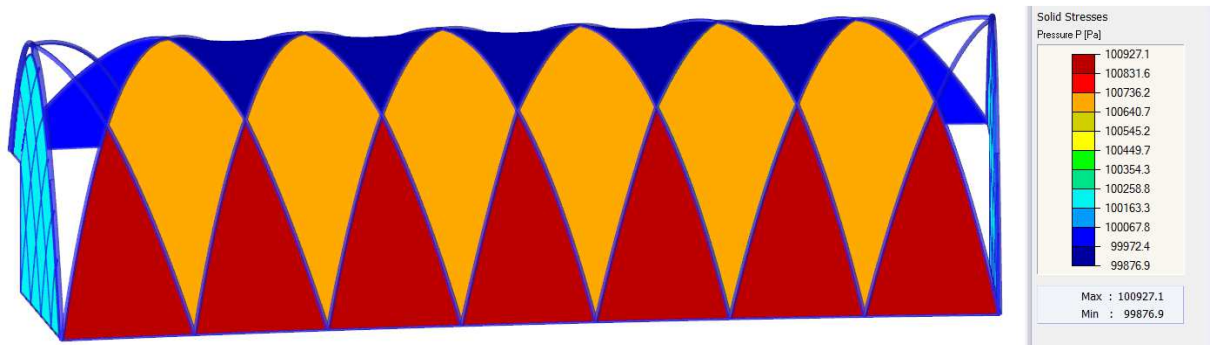
Fig. 123 – Total pressure (atmospheric pressure + change of pressure)

Further, the main internal forces are presented (*Fig. 124 - Fig. 127*) separately for the ETFE layers and the wooden shells as the magnitude is very different and the common result would not be very clear. Finally, the bending moments in the wooden shell (*Fig. 128*), the normal force and the bending moments in steel beams (*Fig. 129 - Fig. 130*) are shown.
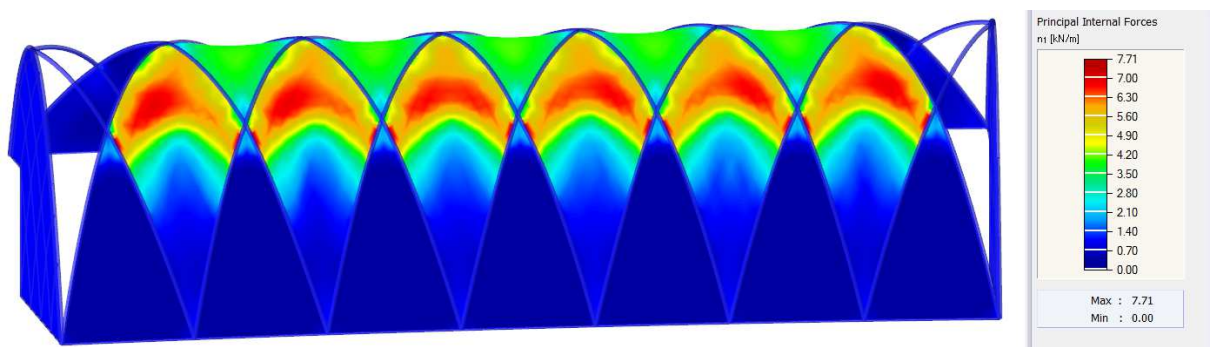
Fig. 124 – Main internal forces n_1 in ETFE layers (CO2)
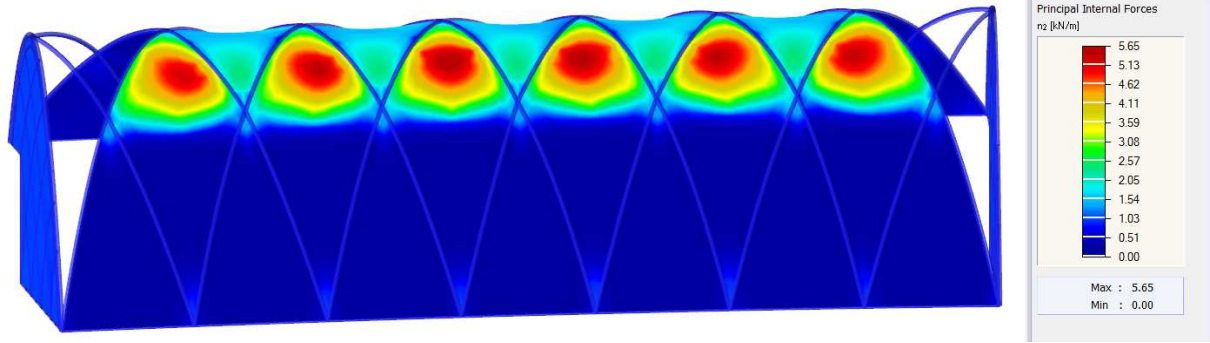
Fig. 125 – Main internal forces n_2 in ETFE layers (CO2)
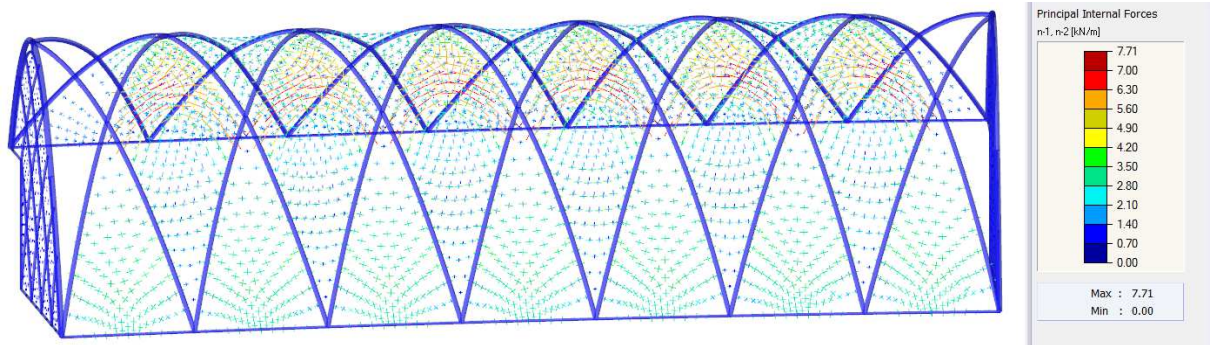
Fig. 126 – Vectors of the main internal forces n_1, n_2 in ETFE layers (CO2)
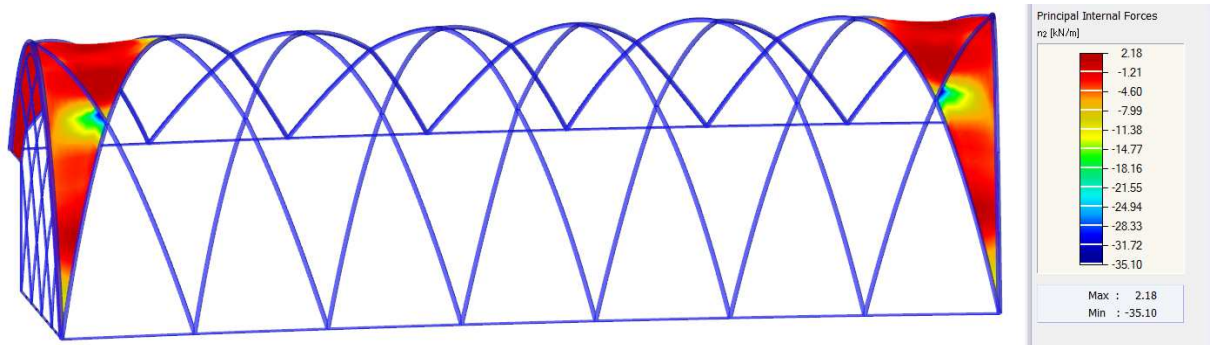
Fig. 127 – Main internal forces n_2 in wooden shells (CO2)
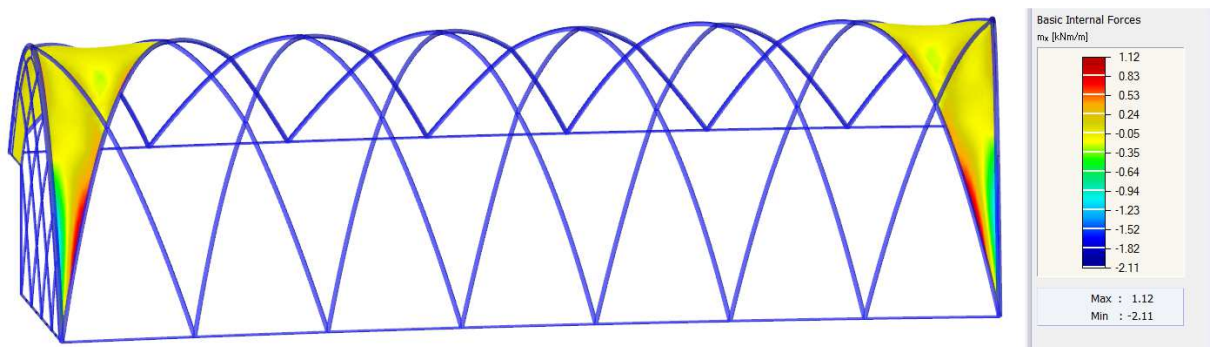
Fig. 128 – Bending moments m_x in wooden shells (CO2)
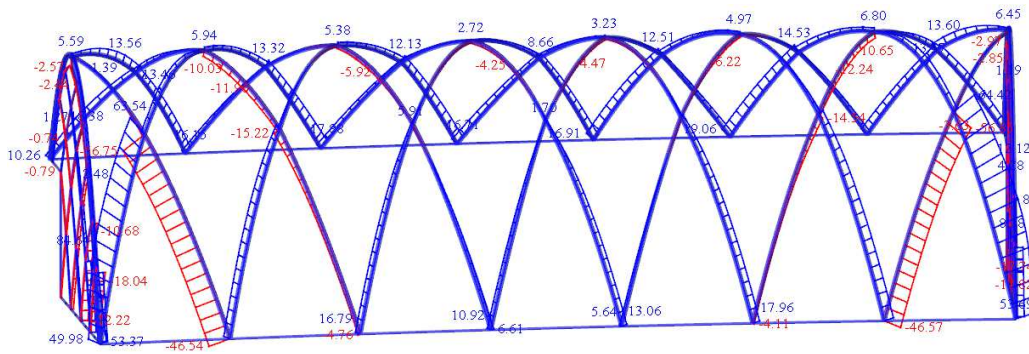
Fig. 129 – Normal forces N (CO2)
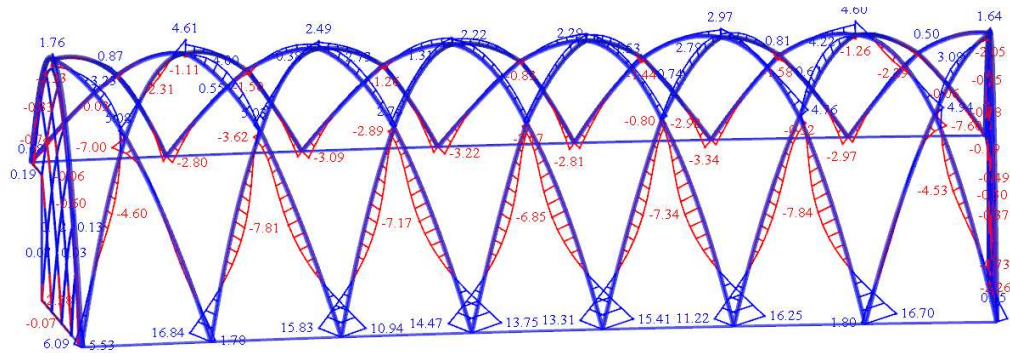
Fig. 130 – Bending moments M_y (CO2)

4 GENERATION OF CUTTING PATTERNS

In addition to the form-finding process, the cutting pattern generation is inherently connected to the membrane structure design, where the goal is to divide the spatial shape into a set of patterns, and to find their closest equivalent in the plane by the flattening. This is the consequence of the double curvature of membrane shapes that cannot be flattened without compromises and thus, the curved patterns have to be approximated by flat patterns. There are many methods developed for the flattening process, where some of them understand this process as a mathematical task while the other consider it as a physical process. The theoretical part of the *Generation of Cutting Patterns* chapter describes the various approaches from both groups. The second part will be focused on the presentation of several examples calculated by the developed tool.

4.1 Theory

The generation process of cutting patterns can be divided into two main parts. First, it is the separation of a spatial surface into a set of spatial patterns, and second, flattening these spatial patterns into the patterns in the plane. While the first task does not cause any distortions as there is no change of the shape, the second task causes unavoidable distortions as the flat pattern is always the approximation of the spatial one, which was double-curved. However, although the separation does not cause any distortions (pattern area, boundary lines length, etc.) because the shape does not change, choosing a specific cutting line has considerable influence on the quality of the resulting pattern. This quality can be understood in both the physical and the aesthetic meaning because the cutting lines define the seam lines layout whose appearance is an important architectural element of the whole structure (*Fig. 131*). The physical impact of the cutting lines on the patterns quality is in cutting differently curved spatial patterns and therefore, in the measure of the necessary distortion during the flattening process as a result.

Fig. 131 – Aesthetic aspect of cutting lines (Center Chodov, Praha, Czech Republic, http://archtex.cz/en/realizace.html)

4.1.1 Cutting Lines

Generally, any line can be used to split the surface into smaller parts as will be shown later. However, as described above, the cutting line shape has a considerable influence on the resulting pattern quality. There are two different line types used broadly: the geodesic and the

planar cuts. However, the geodesic cut type is usually the preferred one [19, 24, 25]. The reason for this preference is the relatively straight pattern after flattening, as shown in the practical part of this chapter. This leads to the minimisation of both the material wastage and the distortion.

The geodesic line can be described as a straight line in the tangential direction of a curved surface in any point. It is often considered as the shortest connection between two points on the curved surface. This is partially the truth because the shortest possible connection between two nodes across the curved surface is always the geodesic line. However, in order to describe the general situation rigorously, more geodesic lines can exist as shown below (*Fig. 132*). These lines represent the global and the local minimum of the distance between two points. However, this case is not frequent in the membrane structure.
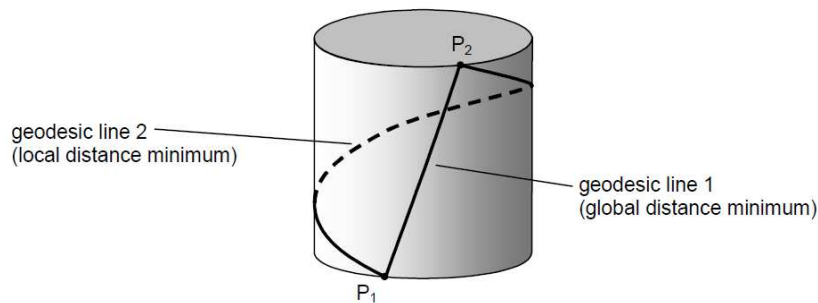
Fig. 132 – Possible existence of several geodesic lines [19]

Since the geodesic line is the straight line in the tangential direction of the curved surface, this line is relatively straight after flattening double-curved surfaces (non-zero Gaussian curvature) and absolutely straight when the Gaussian curvature is zero (e.g. cone and cylinder).

The way how to create geodesic line over the FE mesh is displayed below (*Fig. 133*), where two points are defined to be connected (left), the geodesic line on the spatial shape is found (middle), and the flattening process is performed (right).
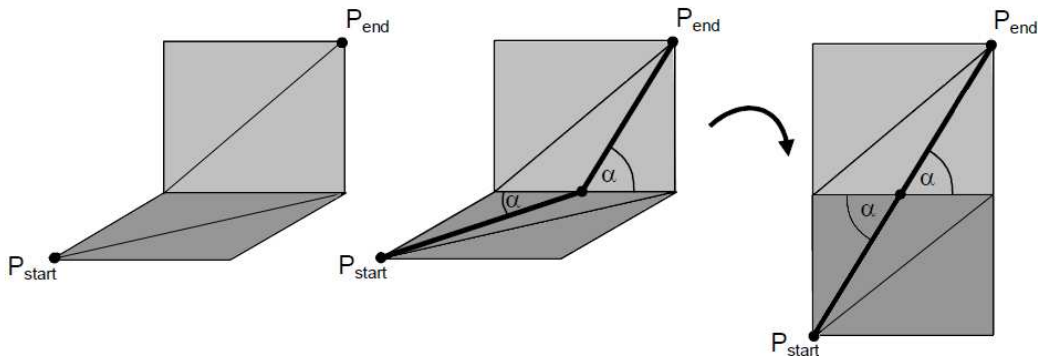
Fig. 133 – The geodesic line on the FE mesh before and after flattening ([19] with modifications)

4.1.2 Flattening Methods

As already mentioned, many methods were proposed for the flattening process, where the goal is to find the planar approximation of the spatial patterns. Some of them consider the process as a mathematical task while the other methods see it as a physical task. The different approaches will be described below, starting from the simplified methods and continuing to the general methods [19, 20, 26-34].

a) Simple Triangulation Method

The first flattening method to be presented is the *simple triangulation technique*. This method is based on modifying the FE mesh that was used for both the form-finding and the structural analysis. This modification is performed in such a way that the surface is obtained, which can be simply developed into plain by rotating the elements according to their edges (*Fig. 134*). It is obvious that the double curvature of the pattern is absolutely lost by such a modification. This geometric approach for the flattening process is characterised by simple implementation and fast calculation but also by low precision. While the FE model can be divided into a finer mesh for the form-finding and structural analysis purposes in order to reach more accurate interpretation of the spatial structure, this will not lead to the improvement of the patterns as the loss of the double curvature is inevitable disadvantage of this method.
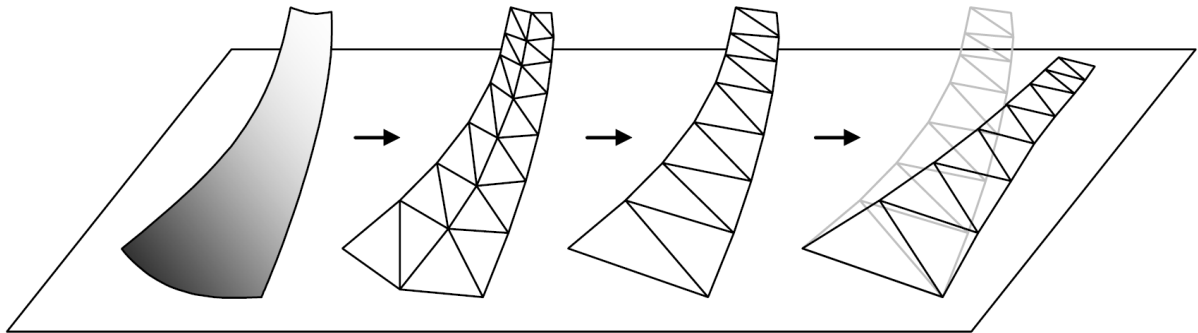
Fig. 134 – The basis of the simple triangulation method (from the left: the spatial shape, the FE mesh of the spatial model used for form-finding and structural analysis purposes, the modified mesh for flattening purposes, the flattened pattern) [19]

b) Mathematical Squashing by Least Square Approach

The second method presented in this thesis is also based on the mathematical approach; however, there is no modification of the FE mesh before the flattening process. This method is searching for the most precise geometric interpretation of the spatial mesh in the plane by minimizing the squares of the defined parameter [29].

$$F(x,y) = \frac{1}{2}v^T P v \longrightarrow min. \tag{21}$$

Where F is the objective function to be minimized, v is the vector residuals and P is the matrix of weights p.

The residuals between the 3D and 2D shape can be defined as a difference of the edge lengths, changes of angles or element areas as defined by the following equations, or they can be even combined with the different weights p.

$$v = l_{2D} - l_{3D} \tag{22}$$

$$v = \alpha_{2D} - \alpha_{3D} \tag{23}$$

$$v = A_{2D} - A_{3D} \tag{24}$$

c) Physical Squashing by Least Square Approach

The most advanced methods derived for the flattening process are based on the physical interpretation of this task. These methods does not only allow for the consideration of the shape change due to pressing the pattern into the plane, but also the material characteristics. The material can be defined as isotropic or orthotropic without any problem. One of the alternatives is to minimize the squares of the stress differences as presented by the equation.

$$F(x,y) = F(x_{2D}) = \frac{1}{2}\int_{\Omega_{2D}}(\sigma_{3D\to2D} + \sigma_{pre}) : (\sigma_{3D\to2D} + \sigma_{pre})d\Omega_{2D} \longrightarrow min. \tag{25}$$

Where F is the objective function to be minimized, x_{2D} is the *Euler coordinates*, $\sigma_{3D\to2D} + \sigma_{pre}$ is the *Cauchy stress* caused by flattening and prestress, Ω_{2D} is the actual configuration of the pattern in 2D.

d) *Physical Squashing with Energy Minimization*

The second physical access represents the most natural way of flattening that minimize the potential energy of the pattern caused by its pressing into the plane. This method follows the essential principle of the FE analysis as it is finding the equilibrium shape of the planar pattern in accordance with the Lagrange variational principle.

$$\Pi = \Pi^{int} = \Pi^{int}_{3D\to2D} + \Pi^{int}_{pre} \tag{26}$$

Since no external forces are present here, the equilibrium shape of the pattern is given by the minimization of the internal potential energy, and its derivation is described by following equation.

$$\frac{\partial\Pi}{\partial d} = \frac{\partial\Pi^{int}}{\partial d} = \frac{\partial(\Pi^{int}_{3D\to2D}+\Pi^{int}_{pre})}{\partial d} = \int_{\Omega_{3D}}(S_{3D\to2D} + S_{pre}) : \delta E_{3D\to2D}\, d\Omega_{3D} =$$
$$\int_{\Omega_{2D}}(\sigma_{3D\to2D} + \sigma_{pre}) : \delta e_{3D\to2D}\, d\Omega_{2D} = 0 \tag{27}$$

Here, the spatial patterns cut out of the membranes shape after the form-finding are considered as the initial (reference) configuration $\Omega_{3D} = \Omega_0$, and the unknown planar patterns are considered as the current (actual) configuration $\Omega_{2D} = \Omega$ (*Fig. 135*). $S_{3D\to2D} + S_{pre}$ and $\sigma_{3D\to2D} + \sigma_{pre}$ are the *2nd Piola-Kirchhoff stresses* and the *Cauchy stresses* caused by the flattening and the prestress of the membrane. $\delta E_{3D\to2D}$ and $\delta e_{3D\to2D}$ are derivatives of the *Green-Lagrange* and *Euler-Almansi strains* caused by the flattening as well.

The prestressed spatial shape is the actual configuration for the form-finding but the reference configuration for the flattening process. Therefore, the final prestress represented by the *Cauchy stresses* after the form-finding is identified with the *2nd Piola-Kirchhoff stresses* here.
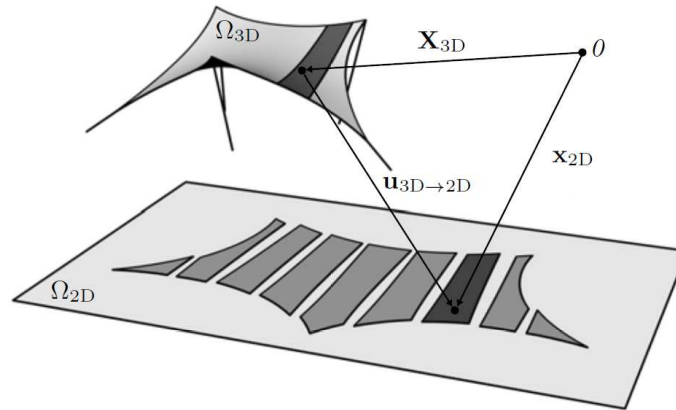
Fig. 135 – The flattening process ([20] with modifications)

It is also possible to combine the different methods in order to find the optimal solution for the implementation into the software. The mathematical squashing can be used to estimate the preliminary planar shape as this method is really fast, and the physical analysis can then be performed in order to improve the initial estimation and to reach the energetically optimized patterns with regard to the material used. This combination provides advantages of both methods, i.e. the increased speed compared to the pure physical access while the same precision is preserved.

4.1.3 Construction Requirements

In addition to the above-described optimization of the pattern from the physical point of view, there are the other requirements to be satisfied, specifically the construction requirements, which are necessary due to manufacturing. The most common requirement is to guarantee the same lengths of the adjacent pattern edges for welding (*Fig. 136*). Another requirement is the utilization of the specific compensation for the boundary line, also known as decompensation.
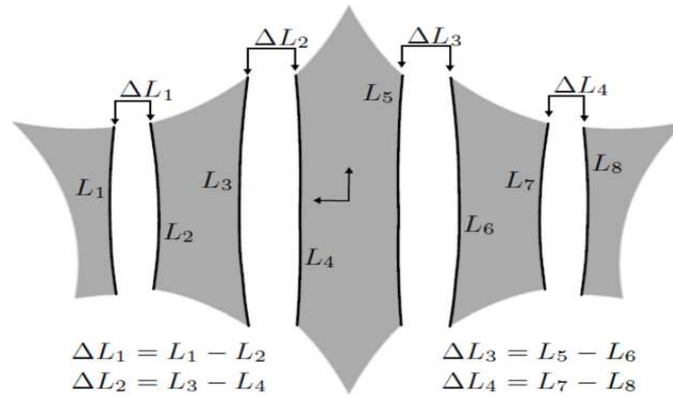
Fig. 136 – Ensuring the same lengths of the boundary lines of the adjacent patterns ([20] with modifications)

This restriction can be implemented into the flattening process without any problems. However, if we consider the energetic optimization of the pattern as the selected method, the reached equilibrium shape will have a higher potential energy with these restrictions than without them. However, this is an inevitable and natural consequence of inserting the required restrictions for any flattening method type.

4.1.4 Compensation

The compensation is the strain caused by prestress, and it usually leads to shortening the pattern, although it is also possible to elongate it, as you can see in the figure below (*Fig. 138*). The compensation values are investigated by the biaxial testing, taking into consideration the specific load diagram where the loading is repeated several times in both directions. The first loading cycle is strongly nonlinear in the case of the woven fabric. The achieved values are used for generating the patterns.
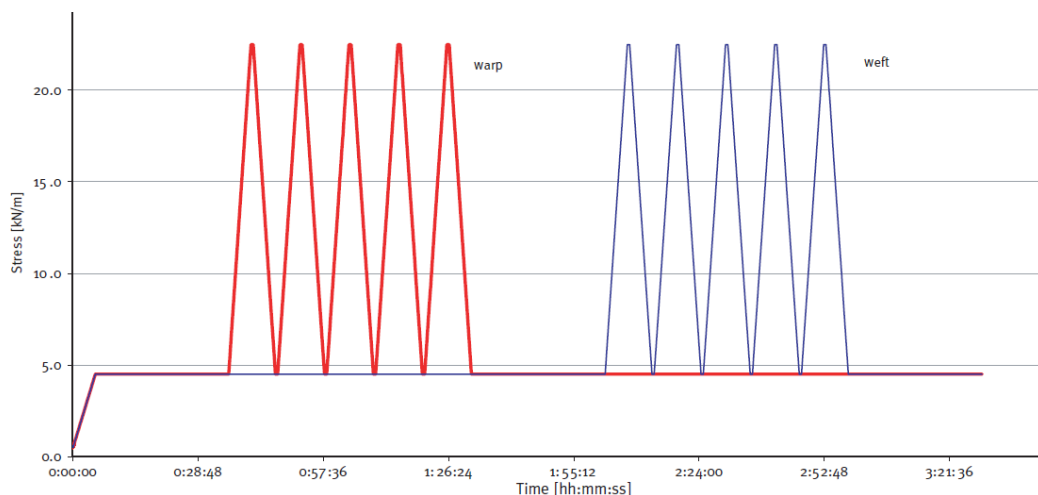
Fig. 137 – Biaxial test: load history [35]
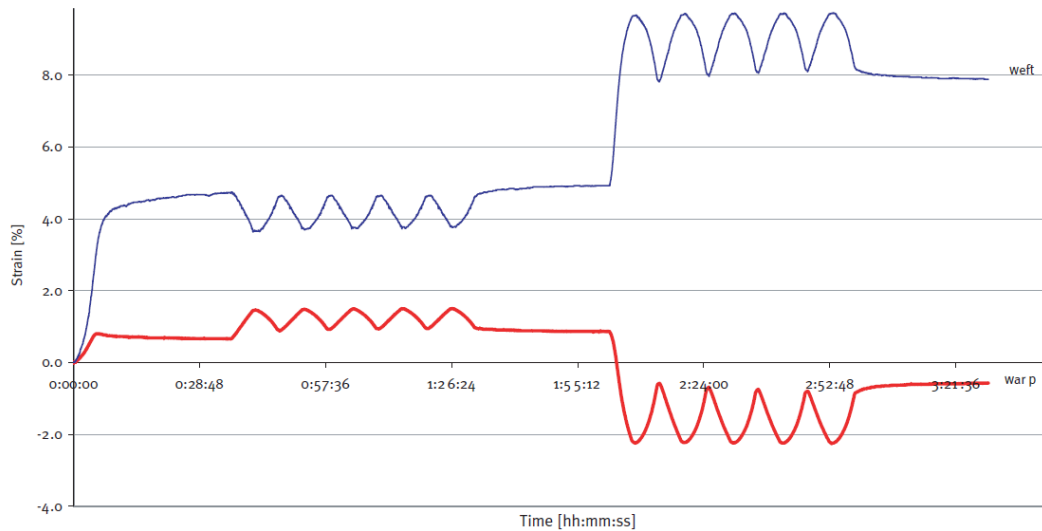
Fig. 138 – Biaxial test: measured strains [35]

It is usual that the compensation is applied after the flattening. However, in order to reach the best solution, both the flattening process and the compensation should be generally performed in one optimization process. This process can be performed using the advanced flattening methods.

The woven fabric is usually approximated by the linear orthotropic material model for the structural analysis according to the values obtained from the testing or production sheet. Such a material can be used in the generation of cutting patterns, where the compensation values obtained are considered at the same time the flattening is performed.

The compensation is used as strain values since the application of stresses would require the precise material model. As you can see in the picture below (*Fig. 139*), the orthotropic plastic material model is generally the most appropriate interpretation of the woven fabric.
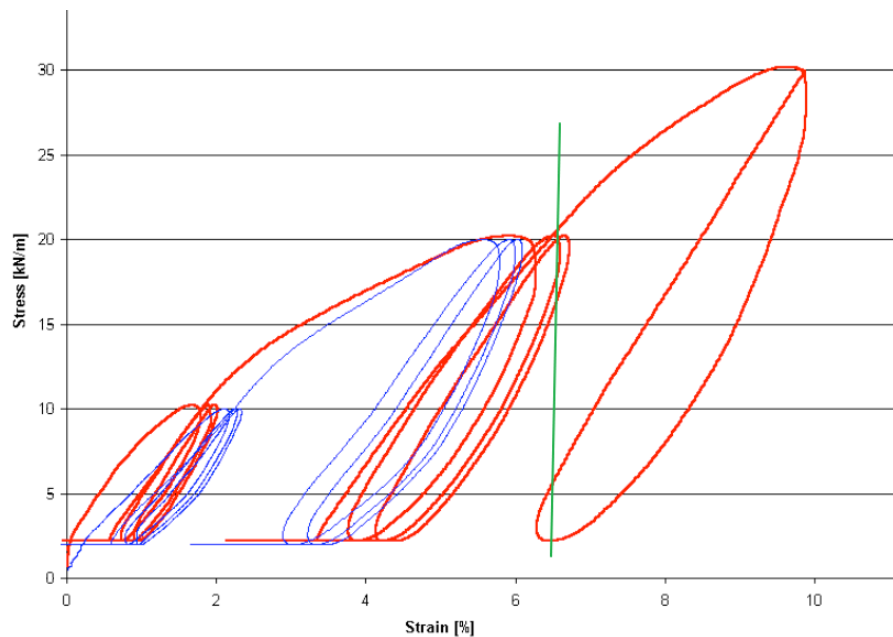
Fig. 139 – Biaxial test: stress-strains diagram [36]

If using such a material model, the automatic compensation is possible. However, it would be necessary to define the prestress value as well as the stress under the load to be able to find the magnitude of the strain under prestress after the plastification as this is the required value

to guarantee the designed prestress after the loading cycles. To demonstrate this statement, the green line was drawn in the enclosed figure (*Fig. 139*). We need to satisfy the prestress $2.4\,kN/m$ in the warp direction after the loading cycles. However, as you can see, the prestress will reach higher values during the erection process because the prestress of $20.5\,kN/m$ is equivalent to the same strain before the plastification caused by loading cycles, which will follow. This is already considered in the compensation values, which are obtained by the diagrams presented above (*Fig. 137, Fig. 138*).

To develop the automatic compensation, further investigation and research are needed. It is also necessary to have wide experience with experiments, which will verify the algorithms to be implemented.

4.2 Practice

In the practical part of this chapter, several examples are presented, using various cutting lines. First, the impact of the cutting lines to the planar patterns will be presented, and second, the evaluation of the pattern quality will be discussed. Finally, the complex structure will be divided into patterns. The pattern quality mentioned here is not considered in the theoretical meaning but in the practical one since even the most precise flattening method is always working with the given spatial pattern. If this one is too wide and curved, too high distortions are necessary, which make the patterns not usable from the practical point of view even though it is a good planar interpretation of the spatial pattern from the theoretical point of view.

On the basis of the advantages described above, the combination of two flattening methods, i.e. the *mathematical squashing* and the *distortion energy minimization*, were implemented into the RF-CUTTING-PATTERN add-on module of the RFEM software. Displaying results for pattern evaluation is currently under development and will be released soon.

4.2.1 Utilization of Different Cutting Lines

The utilization of different cutting lines was mentioned in the theoretical part and it will be presented now in a practical example. Three types of lines are used for the hypar structure: arbitrary lines, geodesic lines, and planar sections (*Fig. 140, Fig. 141*).
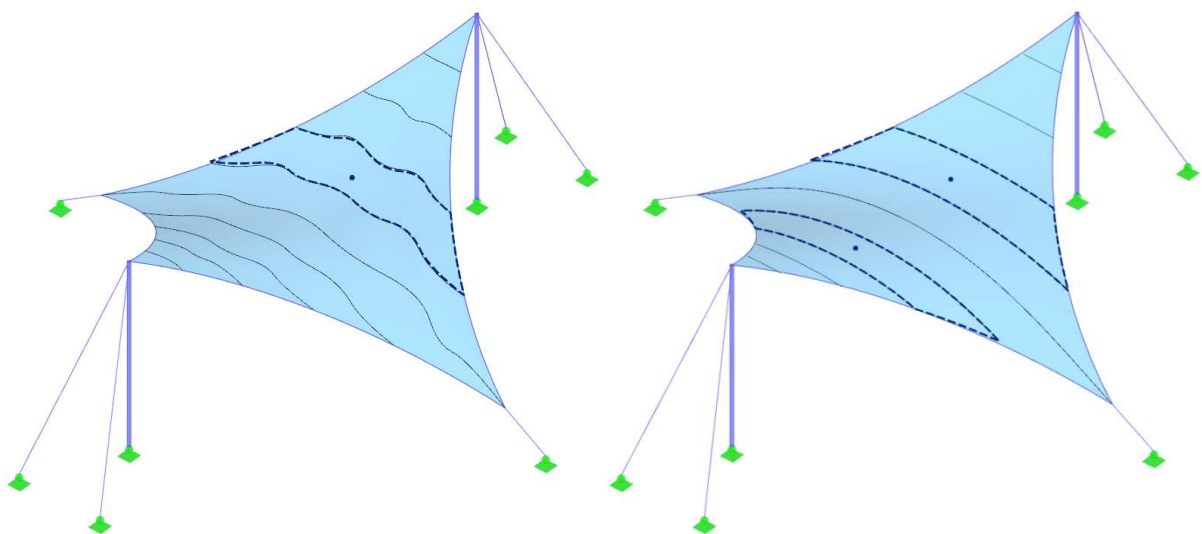
Fig. 140 – Using different cutting lines to split the membrane; arbitrary lines (left), geodesic lines (right top) and planar sections (right bellow)
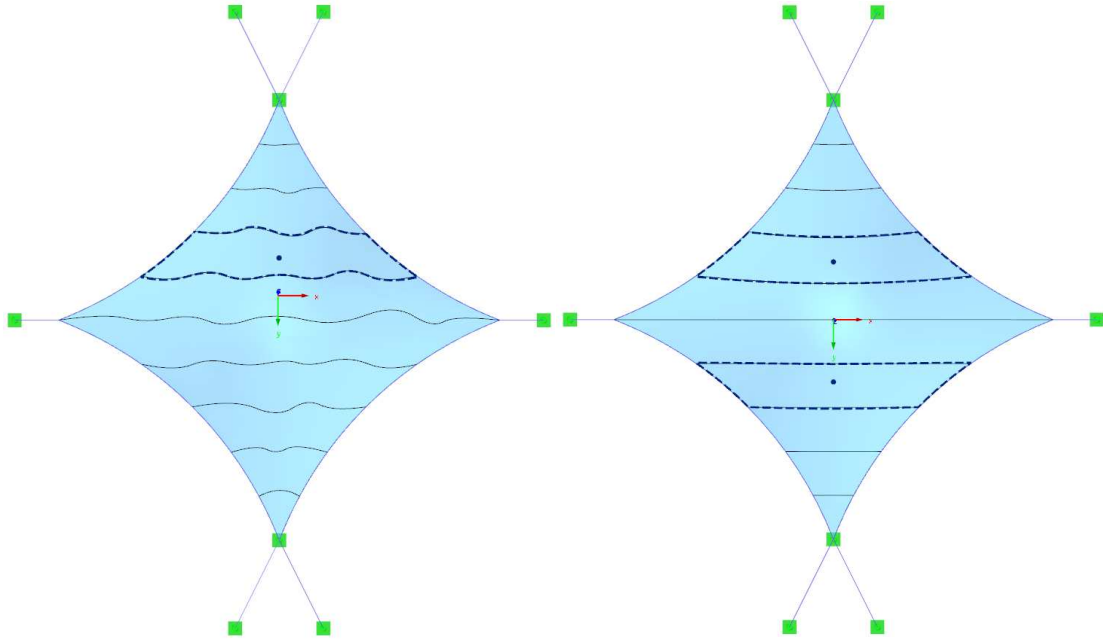
Fig. 141 – Using different cutting lines to split the membrane; arbitrary lines (left), geodesic lines (right top) and planar sections (right bellow)
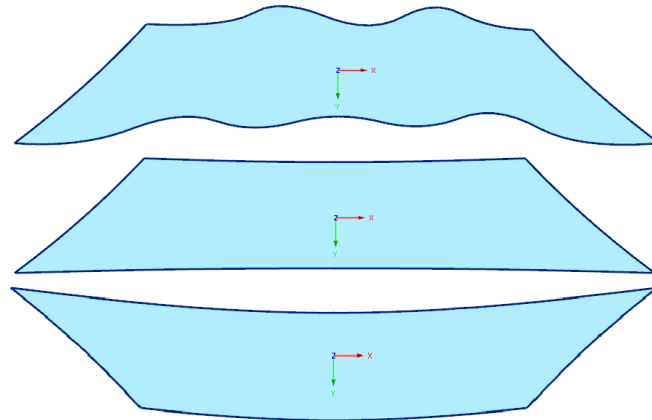
Fig. 142 – Resulting patterns using the arbitrary lines (top), geodesic lines (middle) and planar sections (bellow)

The well-known experience is that the geodesic lines produce straight patterns while minimizing the material wastage. On the other hand, planar sections produce patterns with more or less curved shape, usually called banana shapes. Such a shape leads to a higher material waste. The arbitrary lines produce really strangely shaped patterns as illustrated in the figure above (*Fig. 142*).

4.2.2 Evaluation of Pattern Quality

The patterns quality will be evaluated using the results of the nonlinear analysis, which is used to minimise the potential energy of flattened patterns. The presented patterns will be calculated on rhombus-shaped cushions consisting of two ETFE layers (*Fig. 143*) with the thickness $t = 300.0\ \mu m$, even though the thickness has no impact on the strain due to the flattening process. The longer diagonal is $a = 10.0\ m$, the shorter one is $b = 4.0\ m$. The linear isotropic material model is considered for this material, with the properties described below.

$$E = 900.0\ MPa, G = 310.0\ MPa, \nu = 0.452 \tag{28}$$

The constitutive matrix of such a material is:

$$C = \begin{bmatrix} C_{11} & C_{12} & C_{13} \\ & C_{22} & C_{23} \\ sym. & & C_{33} \end{bmatrix} = \begin{bmatrix} C_{xxxx} & C_{xxyy} & C_{xxxy} \\ & C_{yyyy} & C_{yyxy} \\ sym. & & C_{xyxy} \end{bmatrix} = \begin{bmatrix} 339.18 & 153.18 & 0.00 \\ & 339.18 & 0.00 \\ sym & & 93.00 \end{bmatrix} \frac{kN}{m} \quad (29)$$

The form-finding process was performed with the isotropic prestress $n_x = n_y = 0.40 \, kN/m$ of the ETFE foil layers and the internal overpressure $p_o = 250.0 \, Pa$ of the gas in chambers. The final shape (*Fig. 143*) will be flattened; in this case, the first cushion is not divided, the second one is divided into four patterns, and the third one is divided into eight patterns.

As already mentioned, the pattern quality to be presented is considered from the practical point of view, not from the theoretical one. From the theoretical point of view, there is no difference in the quality because all of the presented patterns are the shapes of minimal potential energy. However, the bigger patterns need higher distortion while pressing down. This distortion is described by the strains caused by this process (*Fig. 145 - Fig. 150*). However, these proportional strains will influence the stress state of the cushions in the construction process where they will have the opposite values as the erection process is inverse to the flattening. When too high values of the strain occur, the prestress can be overcome and wrinkles appear as a result, or the opposite situation can happen as too high stresses arise. From the practical point of view, the patterns have a higher quality when the strain caused by flattening is smaller. The smaller is the pattern, the smaller strain is reached. However, it is not possible to divide the structure into too many too small patterns so it is necessary to opt for a compromise in order to find a good solution that will satisfy the requirement of a well-prestressed structure.
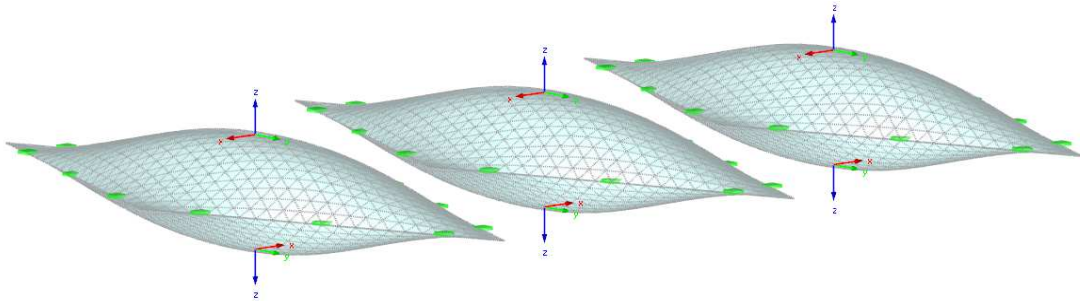
Fig. 143 – ETFE cushions with the x/y (warp/weft) orientation displaying, FE mesh
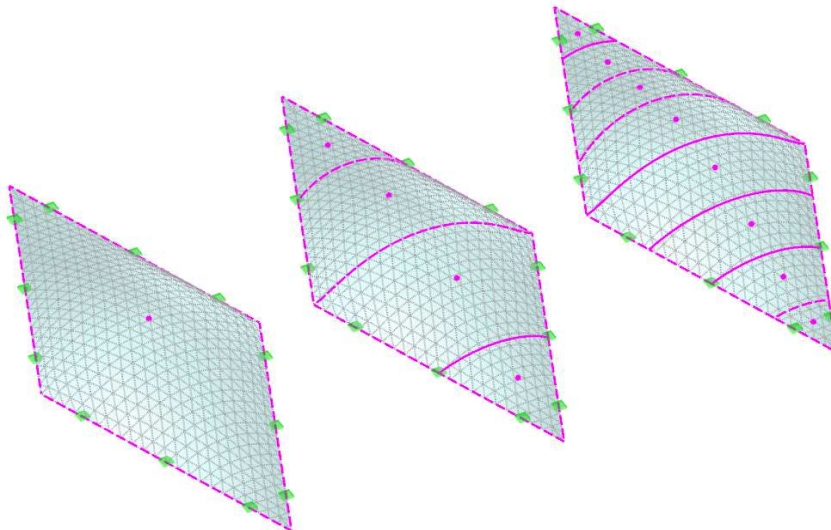
Fig. 144 – Spatial patterns (3D) with the information that the mathematical squashing was performed
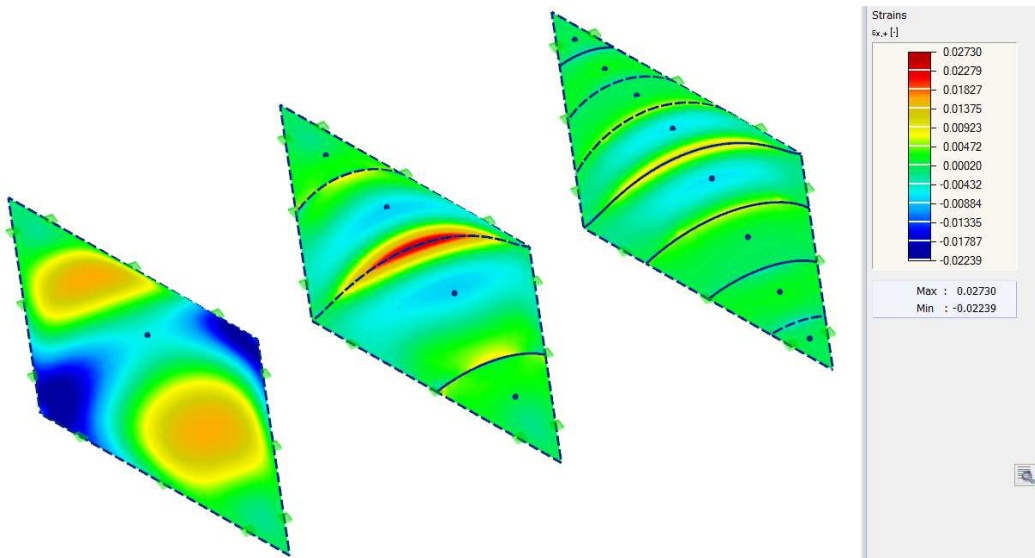
Fig. 145 – Strains ε_x in 2D patterns caused by flattening (displayed on spatial (3D) patterns for having compact model of all patterns)
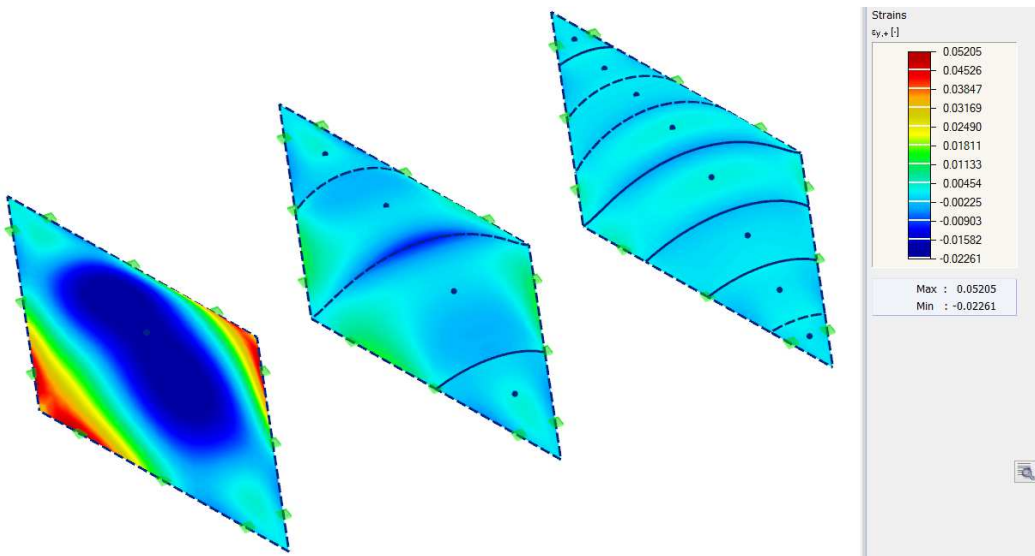
Fig. 146 – Strains ε_y in 2D patterns caused by flattening
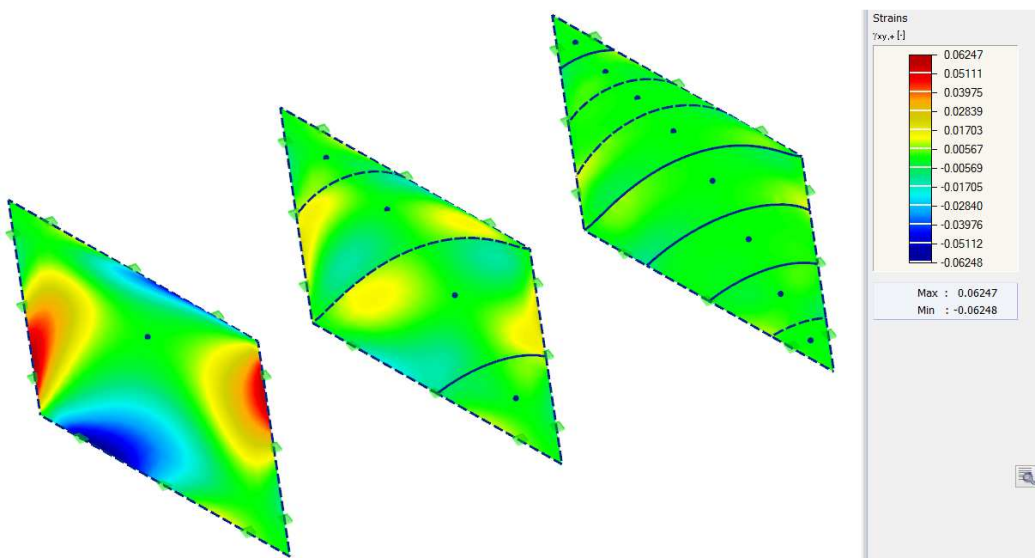
Fig. 147 – Strains ε_{xy} in 2D patterns caused by flattening
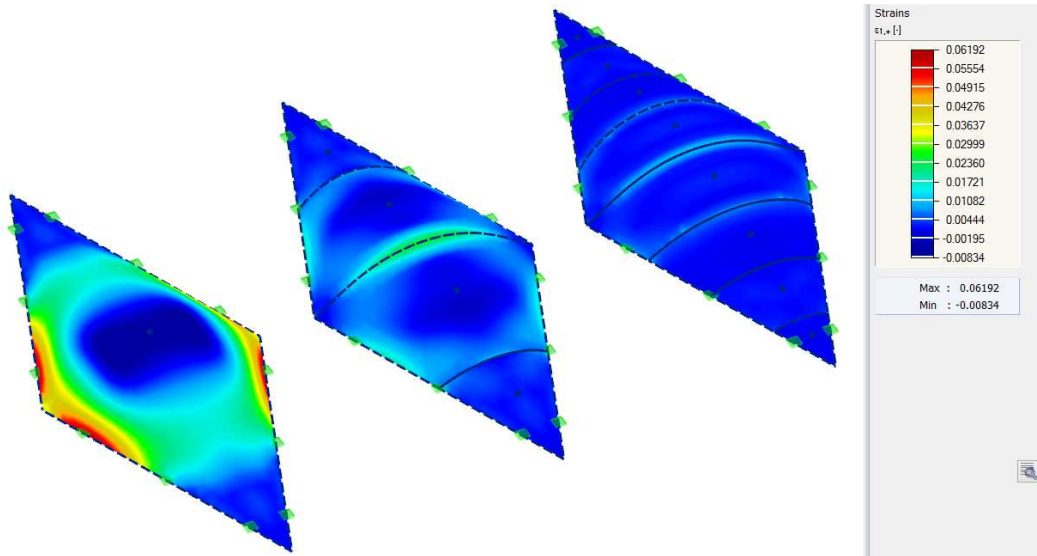
Fig. 148 – Strains ε_1 in 2D patterns caused by flattening
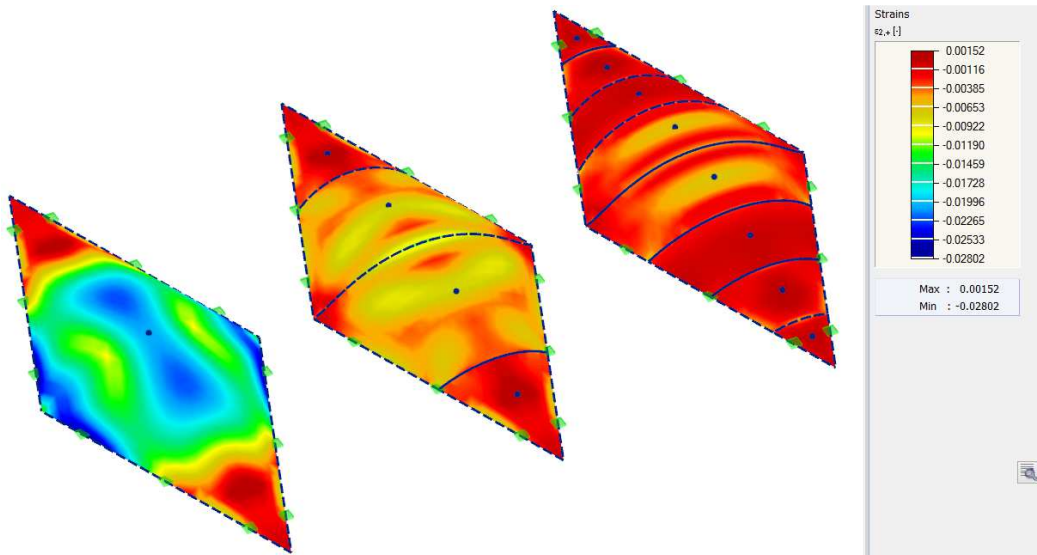
Fig. 149 – Strains ε_2 in 2D patterns caused by flattening
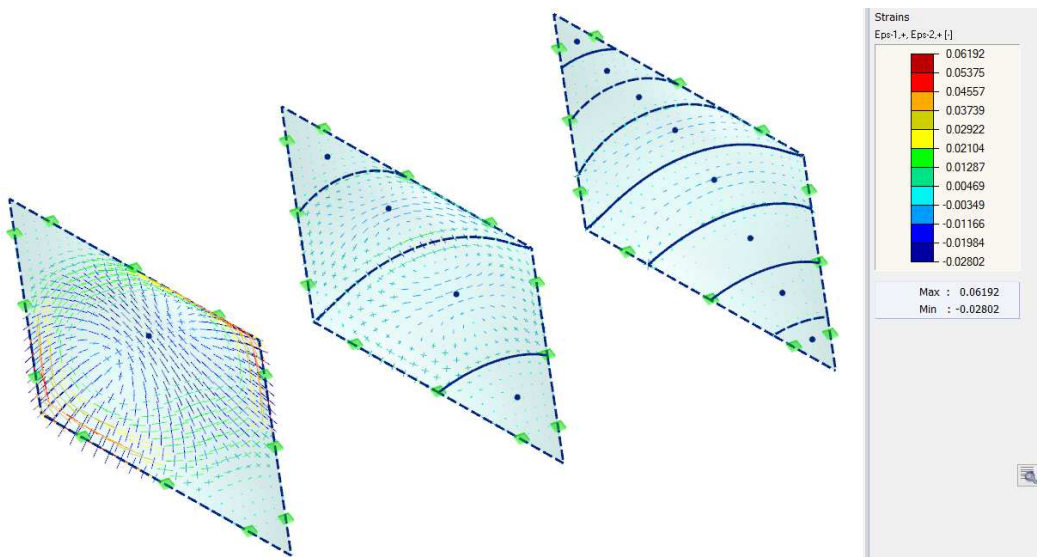
Fig. 150 – Vectors of strains $\varepsilon_1, \varepsilon_2$ in 2D patterns caused by flattening
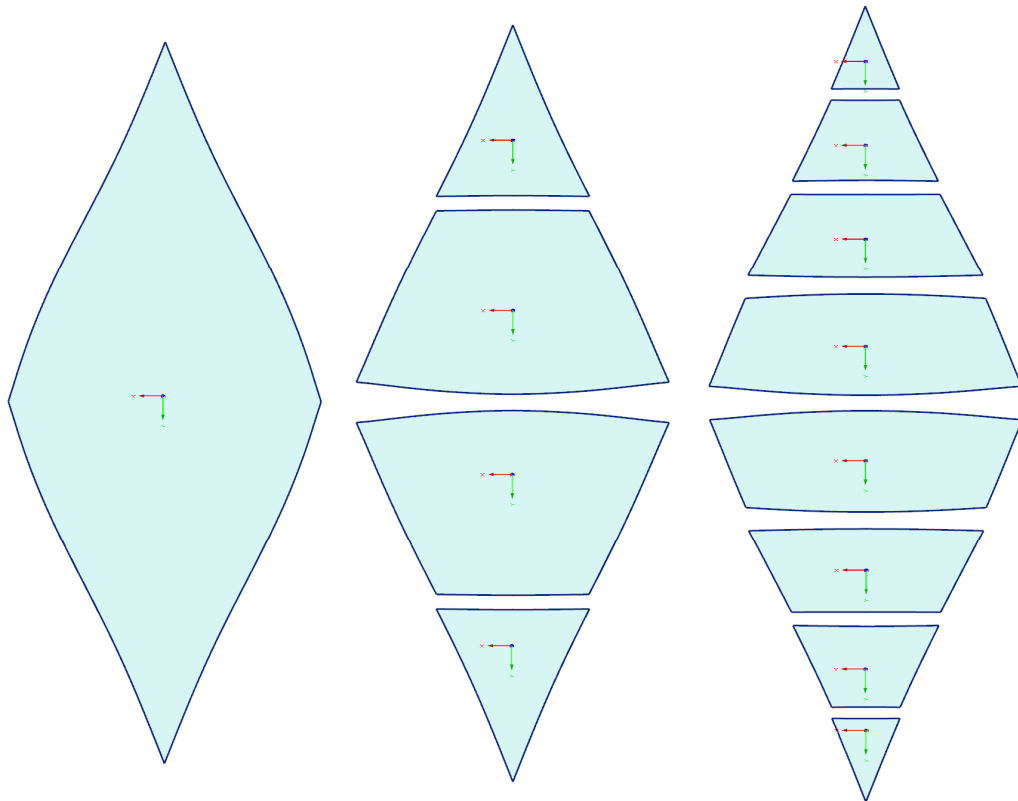
Fig. 151 – Flattened (2D) patterns with the information that the distortion energy minimization was performed

The purple edges of the patterns suggest that the preliminary shapes were calculated using the *mathematical squashing* (*Fig. 144*) while the blue edges suggest that the nonlinear analysis was performed to find the patterns by using the *distortion energy minimization* (*Fig. 145 - Fig. 151*). Planar patterns can be displayed in a dialogue box (*Fig. 151*) or exported to draw the structural details. The strain is displayed on the user-defined structure in the main software's environment. It is also possible to display the stress changes due to the flattening. As mentioned above, strain/stress will have inverse values in the erection process. When considering the big pattern, the compression can be observed in the middle and the tension at the edges during the flattening process while the overstress will appear in the middle and the low stresses at the edges in the erection process.

4.2.3 Structural Requirement

The last structure presented here is a composition of four cone-shaped membranes (or five, if counted the small one in the middle) and eight hypar shaped membranes. The diameters of the cone membranes are approximately $d \approx 20.0\,m$, the heights are $h = 8.0\,m$. The ground plan dimensions of the hypar membranes are approximately $a \approx b \approx 10.0\,m$ and the heights are $h = 3.0\,m$. The entire system is subjected to the form-finding process and afterwards, patterns are calculated on the resulting shape. The widths of the patterns at the bottom of the cones are approximately $w \approx 2.0\,m$, to have an overview of the structure dimensions.

Again, the first round of the cutting pattern generation process is the *mathematical squashing*, the second one is the *distortion energy minimization*. In the following, some details of the input data for this analysis will be described. The input data can be entered in the dialogue box in four categories: *Compensation*, *Compensation by Boundary Line*, *Allowances*, *Line Type* (*Fig. 152*).The compensation can be defined as a constant or linear

value in the warp/weft directions in the second tab of the dialogue box. The specific compensation for the boundary lines can be defined in third tab of the dialog box, if required. In the fourth tab, it is possible to define the allowances for the welding/boundary lines as well as the individual allowances for the selected line, if required. In the last tab, the line category is specified, and there are two possible types: *boundary line* and *welding line*. The default setting is that boundary lines are the lines that do not touch any other pattern or patterns (lines a/c in *Fig. 152*). On the other hand, welding lines are the lines that do touch the other pattern or patterns (since more than two patterns can meet in one line although this is not common) (lines b/d in *Fig. 152*). It is guaranteed that the welding lines of the neighbouring patterns have the same length after the calculation. If it is required to freely flatten the patterns without any interaction between them, it is possible to change the welding line to the boundary line and such a requirement will not be taken into account in the pattern optimization process. As can be seen in the figure (*Fig. 152*) bellow, it is possible to *Consider material from model* in the pattern calculation since there are quite big differences between the isotropic materials such as ETFE and the orthotropic materials such as woven fabrics, and these properties can be taken into account. If it is not intended to use a specific material in the pattern calculation, it is possible to use the *Isotropic material ($E_{warp}/E_{weft} = 1; \nu = 0$)* as this material guarantees the same behaviour in the warp/weft direction and no interaction between them through the Poisson's ratio.

The separate patterns are flattened in the *mathematical squashing* without considering the options described above. Such shapes are an initial estimation or patterns used for the consequent analysis applying the *distortion energy minimization* where all the patterns are calculated together to find the global energy minimum. All above-described possibilities are taken into account and the interaction between the patterns is guaranteed, if the welding lines are present.
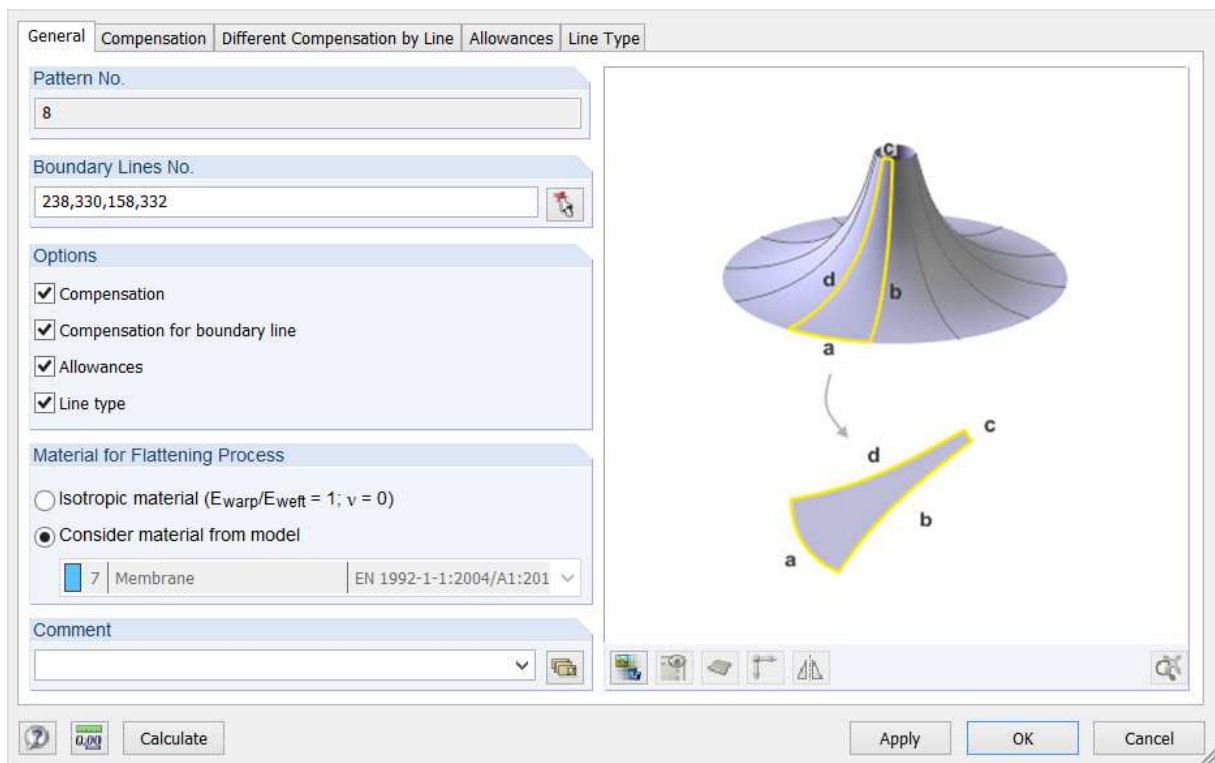
Fig. 152 – Dialogue box for generating cutting patterns (RF-CUTTING-PATTERN)

The material used for the presented membrane structure is the woven fabric. The mechanical properties are approximated by the orthotropic linear elastic material model, which is used in both the structural analysis and the cutting pattern generation.

$$E_x = 1000.0 \frac{kN}{m}, E_y = 800.0 \frac{kN}{m}, G_{xy} = 100.0 \frac{kN}{m}, \nu_{xy} = 0.10, \nu_{yx} = 0.08 \qquad (30)$$

The thickness of the membrane is $t = 1.0\ mm$ and the resulting constitutive matrix is:

$$C = \begin{bmatrix} C_{11} & C_{12} & C_{13} \\ & C_{22} & C_{23} \\ sym. & & C_{33} \end{bmatrix} = \begin{bmatrix} C_{xxxx} & C_{xxyy} & C_{xxxy} \\ & C_{yyyy} & C_{yyxy} \\ sym. & & C_{xyxy} \end{bmatrix} = \begin{bmatrix} 1008.06 & 80.65 & 0.00 \\ & 806.45 & 0.00 \\ sym. & & 100.00 \end{bmatrix} \frac{kN}{m}$$

$$(31)$$

The structure division (*Fig. 153, Fig. 154*) can be seen bellow (*Fig. 155, Fig. 156*). The purple colour suggests that the preliminary calculation was performed, the blue colour means that the FE-based calculation of the planar patterns was done, applying the *distortion energy minimization*.
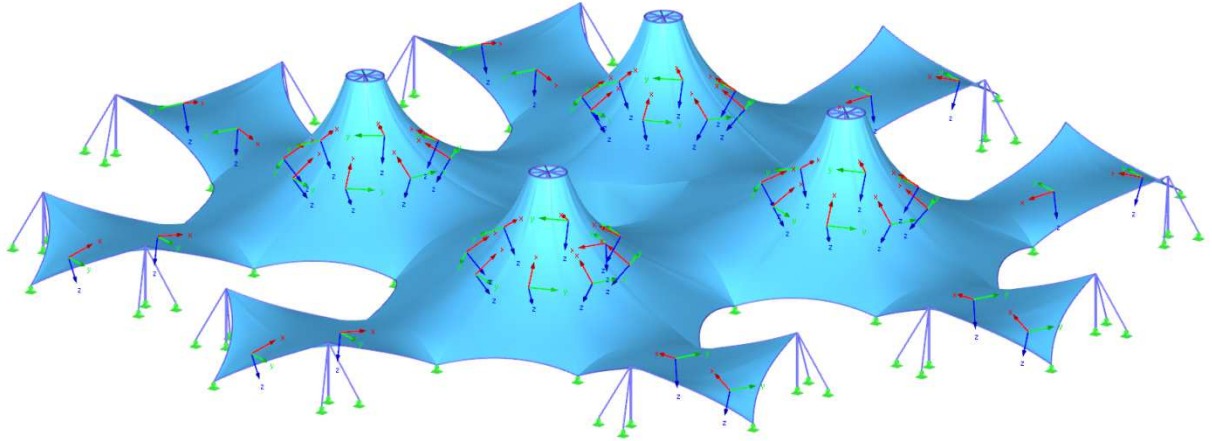
Fig. 153 – Membrane structure with the x/y (warp/weft) orientation displayed

Fig. 154 – FE mesh of the membrane structure

Fig. 155 – Spatial patterns (3D) with the information that the mathematical squashing was performed

Fig. 156 – Spatial patterns (3D) with the information that the distortion energy minimization was performed

As in the case of the structural analysis, the more precise results are reached with a finer FE mesh.

5 CONCLUSION

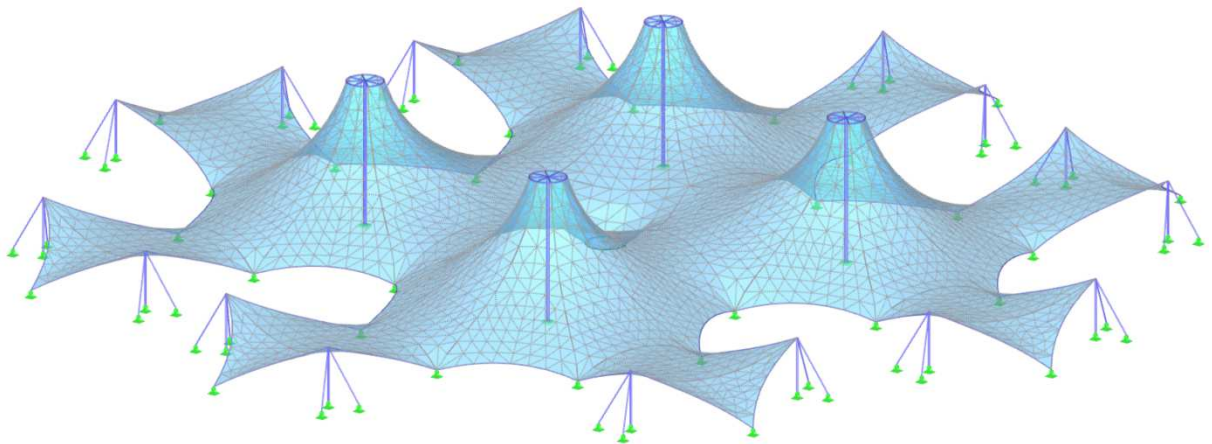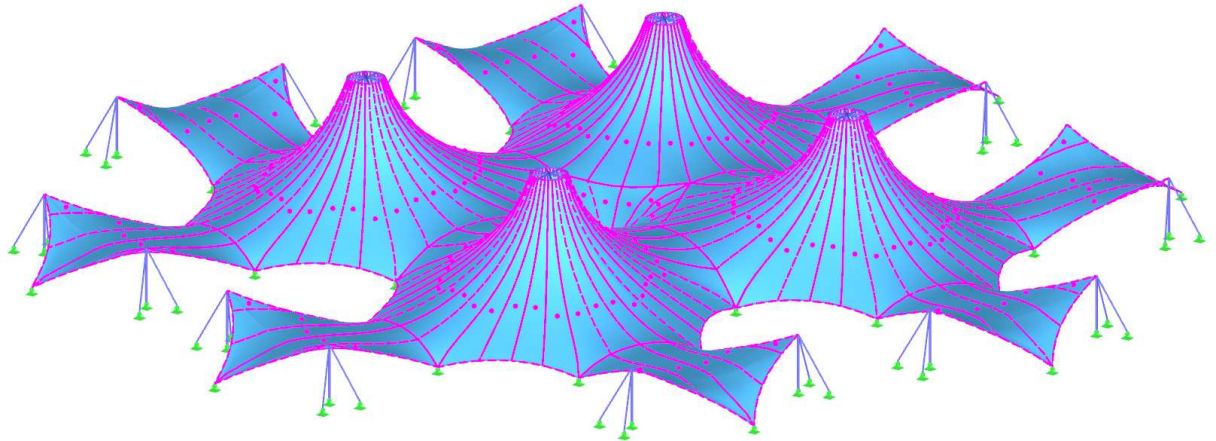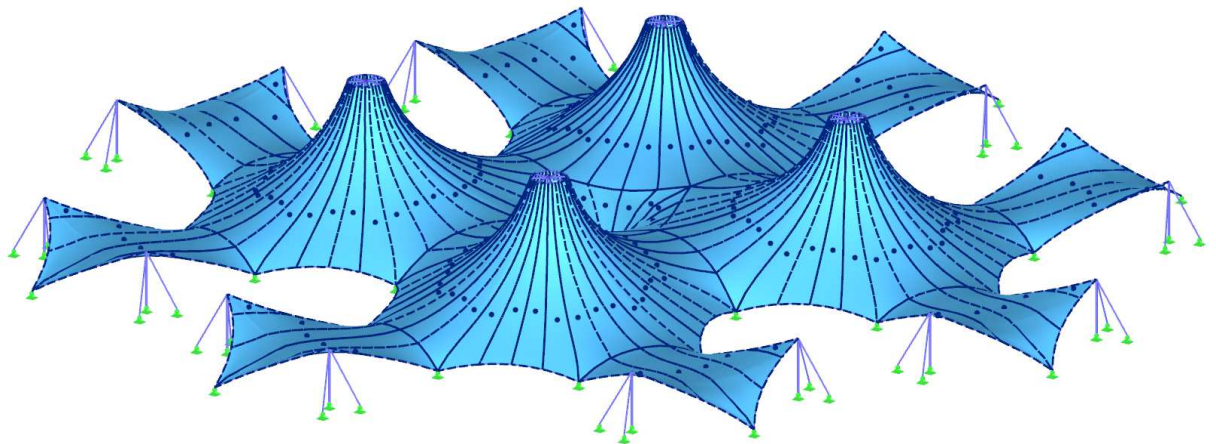The intention of this work was to summarize the principles of three basic steps when designing membrane structures, and to demonstrate the practical examples described in the chapters *Form-Finding*, *Structural Analysis*, and *Generation of Cutting Patterns*. The examples shown here present basic principles of the form-finding analysis as well as some important differences compared to the structural analysis, and also the nonlinear behaviour of these structures, including the specific task of flattening the membrane, which has to be divided into a set of patterns. The evaluation of the patterns using the nonlinear analysis results can be an important tool in the designing process. It is unquestionable that the membrane structures are fascinating topic for many specialists since their architectural expression, structural specifics and, of course, really complex physical behaviour provides a wide space for many new concepts and researches.

The examples presented here were created in the RFEM software [III], including the tools for the essential designing steps described above that were developed and implemented in the last years. Form-finding of the membrane and cable structures as well as the structures under compression, as presented in this work, can be performed using the RF-FORM-FINDING add-on module. The structural analysis can be done in the main program RFEM and the RF-CUTTING-PATTERN add-on module allows for flattening the spatial structure into the plain as a set of patterns. The challenging development resulted in the release of these tools; however, it is certain that the further development is an amazing and endless journey and many new tools are in the process of development or planning. For example, there are two new improvements that will be released soon: the first one is a tool for the calculation of pneumatic structures, and the second one is the display of strains/stresses caused by the flattening process, which can be used for the pattern evaluation. The examples created by using both tools were presented in this work.

6 REFERENCES

[1] Otto, F., & Rasch, B. (1995). *Finding Form.* Deutscher Werkbund Bayern: A.Menges.

[2] Bletzinger, K., & and Ramm, E. (1999). A General Finite Element Approach to the Form Finding of Tensile Structures by the Updated Reference Strategy. *International Journal of Space Structures,* 14(2), 131-146.

[3] Bletzinger, K., & Ramm, E. (2001). Structural Optimization and Form Finding of Light Weight structures. *Computers and Structures*, 79(22-25), 2053-2062.

[4] Bletzinger, K., Wüchner, R., Daoud, F., & Camprubi, N. (2005). Computational Methods for Form Finding and Optimization of Shell and Membranes. *Computer Methods in Applied Mechanics and Engineering,* 194(30-33), 3438-3452.

[5] Wüchner, R., & Bletzinger, K. (2005). Stress-adapted numerical form finding of pre-stressed surfaces by the updated reference strategy. *International Journal for Numerical Methods in Engineering,* 64(2), 143–166.

[6] Bletzinger, K., Firl, M., Linhard, J., & Wüchner, R. (2010). Optimal shapes of mechanically motivated surfaces. *Computer Methods in Applied Mechanics and Engineering*, 199(5-8), 324–333.

[7] Barnes, M. (1999). Form Finding and Analysis of Tension Structures by Dynamic Relaxation. *International Journal of Space Structures*, 14(2), 89-104.

[8] Wakefield, D. (1999). Engineering Analysis of Tension Structures: Theory and Practice. *Engineering Structures*, 21(8), 680-690.

[9] Schek, H. (1974). The Force Density Method for Form Finding and Computations of General Networks. *Computer Methods in Applied Mechanics and Engineering*, 3(1), 115-134.

[10] Linkwitz, K. (1999). Formfinding by the Direct Approach and Pertinent Strategies for the Conceptual Design of Prestressed and Hanging Structures. *International Journal of Space Structures*, 14(2), 73-88.

[11] Bletzinger, K., Linhard, J., & Wüchner, R. (2009). Extended and Integrated Numerical Form Finding and Patterning of Membrane Structures. *Journal of the international association for shell and spatial structures*, 50, 35-49.

[12] Linhard, J., & Bletzinger, K. (2010). "Tracing" the Equilibrium - Recent Advances in Numerical Form Finding. *International Journal of Space Structures,* 25(2), 107-116.

[13] Veenendaal, D., & Block, P. (2012). An overview and comparison of structural form finding methods for general networks. *International Journal of Space Structures*, 49(26), 3741–3753.

[14] Argyris, J.H., Angelopoulos, T. & Bichat, B. (1974). A General Method for the Shape Finding of Lightweight Tension Structures. *Computer Methods in Applied Mechanics and Engineering,* 3(1), 135-149.

[15] Maurin, B., & Motro, R. (1998). The surface stress density method as a form-finding tool for tensile membranes. *Engineering Structures*, 20(8), 712-719.

[16] Pauletti, R.M.O., & Pimenta, P.M. (2008). The natural force density method for the shape finding of taut structures. *Computer Methods in Applied Mechanics and Engineering,* 197(49-50), 4419-4428.

[18] Bonet, J., & Mahaney, J. (2001). Form finding of membrane structures by the updated reference method with minimum mesh distortion. *International Journal of Solids and Structures*, 38(32-33), 5469-5480.

[19] Bletzinger, K.U., Dieringer, F., & Philipp, B. (2013). *Numerical Theory (MM2)* (Manuscript, Master Membrane Structures). Anhalt University of Applied Sciences.

[20] Dieringer, F. (2014). *Numerical Methods for the Design and Analysis of Tensile*

Structures (Dissertation). Ingenieurfakultät Bau Geo Umwelt, Technische Universität München.

[21] Moritz, K. (2007). Bauweisen der ETFE-Foliensysteme. *Stahlbau, 76. Jahrgang, Heft 5.*

[22] Němec, I. at al. (2010). *Finite element analysis of structures: Principles and Praxis*, (1st ed.). Aachen: Shaker Verlag.

[23] Moritz, K. & Schiemann, L. (2013). *Structural Design Concepts (MM6)* (Manuscript, Master Membrane Structures). Anhalt University of Applied Sciences.

[24] Martínez, D., Velho, L., & Carvalho, P.C. (2005). Computing geodesics on triangular meshes. *Computers & Graphics*, 29(5), 667–675.

[25] Yang, B., & Lu, Y. (2011). Computing Approximate Geodesic on Triangular Mesh. *Journal of Information & Computational Science*, 8(5), 826–832.

[26] Dieringer, F., Wüchner, R., & Bletzinger, K.U. (2011). Advanced cutting pattern generation – Consideration of structural requirements in the optimization process. *V International Conference on Textile Composites and Inflatable Structures, STRUCTURAL MEMBRANES 2011*, 84-91.

[27] Maurin, B., & Motro, R. (1999). Cutting Pattern of Fabric Membranes with the Stress Composition Method. *International Journal of space Structures*, 14(2), 121-129.

[28] Moncrieff, E., & Topping, B.H.V. (1990). Computer Methods for the Generation of Membrane Cutting Patterns. *Computers and Structures*, 37(4), 441-450.

[29] Ströbel, D., Gründig, L., & Singer, P. (2013). Selected Examples for the Optimization of Cutting Patterns for Textile Membranes. *VI International Conference on Textile Composites and Inflatable Structures, STRUCTURAL MEMBRANES 2013,* 258-267.

[30] Kim, J.Y., & Lee, J.B. (2002). A new technique for optimum cutting pattern generation of membrane structures. *Engineering Structures*, 24(6), 745–756.

[31] Cai, Z.Y., Li, M.Z., & Zhang, H.M. (2007). A simplified algorithm for planar development of 3D surface and its application in the blank design of sheet metal forming. *Finite Elements in Analysis and Design*, 43(4), 301–310.

[32] Zhong, Y., & Xu, B. (2006). A physically based method for triangulated surface flattening. *Computer-Aided Design*, 38(10), 1062–1073.

[33] Li, J., Zhang, D., Lu, G., Peng, Y., Wen, X., & Sakaguti, Y. (2005). Flattening triangulated surfaces using a mass-spring model. *The International Journal of Advanced Manufacturing Technology*, 25(1-2) 108-117.

[34] Zhang, Q.L., & Luo, X.Q. (2003). Finite element method for developing arbitrary surfaces to flattened forms. *Finite Elements in Analysis and Design*, 39(10), 977-984.

[35] Forster, B., & Mollaert, M. (2004). *European Design Guide for Tensile Surface Structures*. Brussel: Vrije Univ. Brussel.

[36] Balz-Bögner, H., & Blum, R. *Mechanical and Physical Properties and Basic on Structural Engineering (CM03)* (Manuscript, Master Membrane Structures). Anhalt University of Applied Sciences.

7 WEB LINKS

[I] *Dlubal Software - Structural Engineering Software for Analysis and Design*. (2017). Retrieved 5 September 2017, from https://www.dlubal.com/en

[II] *FEM consulting, s.r.o – Development of software systems for building and machine construction solutions*. (2017). Retrieved 5 September 2017, from http://www.fem.cz/?lang=en

[III] Dlubal Software. (2017). *Analysis & Design Software for Tensile Membrane Structures*. Retrieved 5 September 2017, from https://www.dlubal.com/en/solutions/industries/analysis-and-design-software-for-tensile-membrane-structures